Title
Elucidating the Solution Chemistry in Graphene Liquid Cell Transmission Electron Microscopy

Author
Crook, Michelle

Publication Date
2023

Peer reviewed|Thesis/dissertation

Elucidating the Solution Chemistry in Graphene Liquid Cell Transmission Electron Microscopy

by

Michelle F Crook

A dissertation submitted in partial satisfaction of the

requirements for the degree of

Doctor of Philosophy

in

Chemistry

in the

Graduate Division

of the

University of California, Berkeley

Committee in charge:

Professor A. Paul Alivisatos, Chair
Professor Ting Xu
Professor Alex Zettl

Spring 2023

Abstract

Elucidating the Solution Chemistry in Graphene Liquid Cell Transmission Electron Microscopy

by

Michelle F Crook

Doctor of Philosophy in Chemistry

University of California, Berkeley

Professor A. Paul Alivisatos, Chair

Graphene liquid cell transmission electron microscopy (TEM) is a technique that can visualize nanoscale dynamics in liquid in real time. The liquid cell TEM technique has bypassed the high vacuum limitations for TEM operation by using electron transparent membranes to encapsulate small volumes of solution. These days, graphene is commonly used as the membrane, which has made atomic resolution imaging of materials in liquids commonplace. This emerging technique has already shown great promise in becoming a powerful characterization tool for the nanomaterials community and beyond, but as with any new technique, careful analysis and understanding of the system are critical for further development.

A major hurdle in the liquid cell TEM technique is understanding and controlling the effects of water radiolysis in the solution from the ionizing electron beam. A variety of reactive species are formed once imaging begins, and understanding how these species interact with the solution and sample is critical to developing this technique. This is a daunting task, as the solution is hermetically sealed within the graphene sheets, the volume within the liquid cell is typically less than an attoliter, and the radical chemistry only occurs when the electron beam is turned on, which greatly limits the methods that can be used to study the solution. Together, these factors make it an extremely challenging task to study the solution chemistry of graphene liquid cells.

This thesis will give an overview of the solution chemistry thought to occur in graphene liquid cells, describe some experimental techniques that can be used to probe this chemistry, and provide experimental results expanding our understanding of the chemistry occurring in these sealed pockets. In Chapter 1, the development of the liquid cell TEM technique, as well as the fundamentals of radiation chemistry, how it is thought to occur within the context of liquid cell TEM, and the current methods used to understand the radiation chemistry will be provided. In Chapter 2, we studied how halides, common additives in nanocrystal synthesis and well known radical scavengers, altered the dynamics of a model system, gold nanocrystal

etching in graphene liquid cells. Correlative pulse radiolysis measurements determined the active oxidant in the gold nanocrystal etching mechanism. These studies revealed the power of using experimental measurements to describe the system. In Chapter 3, electron energy loss spectroscopy was used to directly measure the solvated species inside a graphene liquid cell. These studies revealed significant concentration of the encapsulated solution, which was also shown to affect the kinetics of oxidation of the active oxidant. Overall, using these experimental methods to measure the solution species in graphene liquid cells have greatly enhanced our knowledge of the system, and how to better design the liquid cell around the desired experiments. In Chapter 4, an outlook of the state of graphene liquid cells and suggestions to adapt the design of the system and modeling of the solution to the experimental results presented herein are given.

To My Parents

Who have always taught me to believe in myself

Contents

List of Figures

List of Tables

Acknowledgments

Working towards obtaining a Ph.D. is no easy task, and is certainly not one that can be completed alone. There are countless people who have led me to this point where I am today, submitting my dissertation as the final requirement to complete my Ph.D..

First and foremost, my parents. They have been there since the beginning, gave me an enriching and fulfilling childhood, and have supported me through all my endeavors, academic or otherwise. They believed in me throughout the good times and the bad, and most importantly, taught me to believe and trust in myself.

The decision to become a chemist most certainly traces back to my high school chemistry teacher Dr. Loomis, colloquially known as Doc. My classmates complained that he made the tests too hard, but ultimately he was giving us the opportunity to challenge ourselves, to see what we could achieve if limits were not placed upon us. The first test I failed was in his class, but it was in this same class where I learned how capable I am. For that, I must thank him.

In my undergraduate studies, I had several excellent professors and mentors that taught me the foundational knowledge needed to become a chemist. Dr. Alistair Lees convinced me to start research in my sophomore year, Dr. Julien Panetier gave me a rigorous physical chemistry education, Dr. Chuan-Jian Zhong taught me the foundations of instrumental analysis with relevance to current research efforts, and the late Dr. Sean McGrady taught me the fundamentals in solid state chemistry.

Of course I would be amiss without mentioning my research advisors throughout the years. I did my first independent research in the lab of Prof. M. Stanley Whittingham under the guidance of Dr. Hui Zhou. Here I learned what research is and how to progress on a scientific project. I also spent two summers during my undergraduate studies performing research at other universities under the guidance of Prof. Chis Ackerson and Prof. Yves Chabal. Each of them helped me pick up and complete a research project in fields new to me. The teachings and experiences I had in each of these research environments was truly formative and I know that I would not have made it to where I am today without this.

I must also thank my thesis advisor, Prof. A. Paul Alivisatos. It was under his guidance where I feel I have truly become a scientist. He has provided me with the tools and resources needed to complete my projects. He supported me in undertaking whatever projects most interested me, and allowed me the time and space to work towards finding these projects on my own. Most importantly, his mentorship style has taught me to become an independent thinker and for that I am grateful.

Of course completing this degree would not have been possible without the support I received inside and outside of the lab. I must thank the many lab mates I've had throughout my time as a graduate student, namely Rafaela Brinn, Priscilla Pieters, Ethan Curling, Jakob Dahl, Justin Ondry, Hyun Dong Ha, Abdullah Abbas, Vida Jamali, Ivan Moreno-Hernandez, Jason Calvin, Chang Yan, and Joeson Wong. I must also thank Kayli Martinez, Nicole Navarro, Marisol Navarro, Kerry Jones, and Suzanna Yaeger-Weiss, my friends outside

of the lab (and inside of my pod during COVID) who provided much needed friendship and camaraderie after a long work day.

Last, but certainly not least, I must thank those who did not think I would make it to this point or even, at times, actively dissuaded me from continuing. It is no secret that getting a Ph.D. is a challenging task, but perhaps the most challenging aspect may be just choosing to continue. I am truly grateful for the challenges I faced because it caused me reflect on my goals and my values and ultimately made me more determined to finish what I had started.

For those I have missed, I thank you as well.

Chapter 1

Introduction

1.1 Overview

Liquid cell transmission electron microscopy (TEM) has emerged as a powerful technique to study nanomaterial dynamics in solution. Liquid cell TEM continues to generate active interest as it is the only technique that provides sub nanometer spatial resolution and sub millisecond temporal resolution in solution, making it well suited to study processes such as nanocrystal nucleation and growth, self assembly, galvanic exchanges, nanocrystal interactions, among others. While this technique has been instrumental in developing our understanding of a variety of nanoscale dynamics, there is still progress to be made in elucidating the effects of the solution chemistry in this technique. Notably, the electron beam used to produce images of the sample is extremely perturbative to the host solution, generating highly reactive species that can alter the chemistry, and observed dynamics, *in situ*. Foundational literature and seminal studies of electron beam effects in the liquid cell have provided a starting point to understand the solution chemistry, but direct measurement of solution processes in the liquid cell will be required to make this a more robust technique moving forward.

To put these recent developments into context, we will first explore the workings of TEMs, the first attempts to observe liquids in the TEM, and the development of the current liquid cells. We will next define the several different types of liquid cells available today, as well as the advantages and disadvantages of each type. Then, we will deeply explore radiolysis, how to understand, mitigate, and control it, and several of the methods commonly used for this. We will explain how, as of today, radiolysis is inextricably linked to the liquid cell technique and many of the observed processes. Accordingly, we will explore the methods that have been used to understand and probe radiolysis, including chemical reaction networks and different types of spectroscopies. Together, these concepts will set the foundation for work presented in Chapters 2 and 3.

1.2 Development of Liquid Cell Transmission Electron Microscopy

As scientists, our curiosity of the surrounding world has led us to develop tools that allow us to see what was previously invisible to the human eye. Since the invention of the first optical microscope *ca.* 1600,[1] scientists have worked tirelessly to improve image quality, resolution, and microscope performance. Nearly every field of science has benefited from discoveries made with an optical microscope. Yet with these improvements to instrument design, eventually came limitations. In 1874, Ernst Abbe became the first to postulate a theoretical limit to the resolution of a microscope as described in Equation 1.1 below, known as Abbe's diffraction limit.

$$R = \frac{\lambda}{2NA} \tag{1.1}$$

In this equation, λ is the wavelength of the illumination source, and NA is the numerical aperture, which for modern instruments is close to 1. Abbe's diffraction limit tells us that as we lower the wavelength of the illumination source, we can increase the resolution of the collected images. For optical microscopes, which use visible light as the illumination source, the smallest wavelength of the illumination source is approximately 400 nm, indicating that the smallest resolvable features are around 200 nm. However, in the pursuit of seeing finer and finer details, scientists theorized that this limit could be circumvented by developing new microscopes using illumination sources with exceedingly small wavelengths.

In 1928, Davisson and Germer published an experiment that confirmed the wave nature of electrons.[2] This confirmed an earlier hypothesis from Louis de Broglie that suggested the wave-particle duality of electrons. According to de Broglie, the momentum of any particle, including electrons, was related to its wavelength through Equation 1.2

$$\lambda = \frac{h}{mv} \tag{1.2}$$

where h is Planck's constant, m is the mass of the electron, and v is the velocity of the electron. Accordingly, by increasing the kinetic energy of an electron, the wavelength is decreased. If, then, an electron beam is used as an illumination source for a microscope, the resolution could be tunable and improved by using higher and higher energies. Indeed, in 1933, the first transmission electron microscope (TEM) with resolution higher than an optical microscope was developed,[3] and continual developments led to increasingly improved performance. Today, modern TEMs operate between 80 and 300 keV, with a few high energy microscopes operating at 1 MeV.[4] With advances in modern instrumentation, the main limitation to the resolution with these high accelerating voltage TEMs is not the wavelength of the illumination source, but coherency of the electron beam and aberrations of the electron lenses.[5–8] To date, the highest resolution that has been achieved with an electron microscope is about 0.5 Å,[9] while resolving single atoms or atomic columns has become commonplace.[5,10–14]

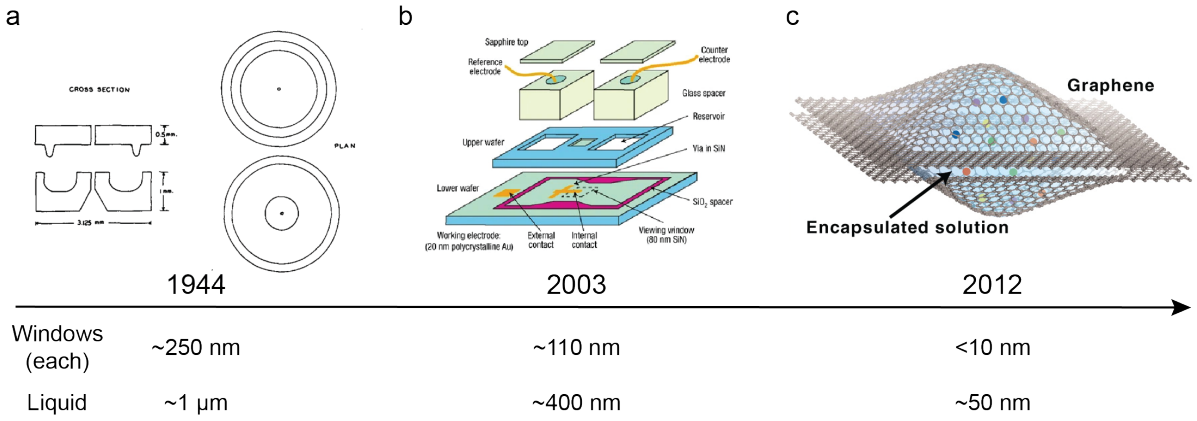

Figure 1.1: Development of liquid cell transmission electron microscopy from a) the first report of creating a closed cell to study high vapor pressure liquids (reproduced with permission from[15], Copyright 1944 AIP Publishing Group), b) the first modern liquid cell which achieved much higher resolution, as well as electrochemical control (reproduced with permission from[17], Copyright 2003 Nature Publishing Group), and c) the first graphene liquid cell, which could distinguish individual lattice planes (reproduced with permission from[18], Copyright 2012 The American Association for the Advancement of Science)

In order to achieve this extremely high resolution, it is necessary to keep the path of the electron beam in the microscope under high vacuum ($\sim 10^{-}5$ mtorr) so that the electrons do not scatter off of any molecules, which may destroy the coherency of the electron beam. This means that the samples that can be studied in TEMs are limited to dry, solid samples, such as metals, oxides, nanomaterials, etc.. Yet, there are many processes in which the interaction of a material with a solution are of prime interest, such as the changes in the interface of a battery electrode when in contact with the electrolyte, attachment of atoms during growth of colloidal nanocrystals, and the structure of hydrated biological materials, just to name a few.

Since 1944, only five years following the first commercial TEM, scientists have been developing methods to introduce low vapor pressure liquids, like water, into the TEM.[15] The first report of introducing liquid water into a TEM was successful at preventing leaks and protecting the liquid from evaporation, but suffered from low resolution. The cell was composed of thick collodion windows, and the thinnest liquid layers that could be achieved with the available technology at that time was approximately 1 μm (Figure 1.1a). The total thickness of these liquid cells were approximately 1.5 μm,[16] which can absorb and scatter sufficient electrons to severely limit resolution.

Several decades later, the idea of a closed cell to contain liquid samples was revisited. With improvements in silicon manufacturing, new cells could be developed with thinner windows and liquid layers. In these new closed cells, a thin silicon nitride window supported by a larger silicon chip was used to enclose the liquid sample (Figure 1.1b).[17] With these

new thinner cells, small copper nanocrystals could be observed, and electrode patterning on the windows could induce electrodeposition, which could be observed in real time in the microscope.[17] This time, the closed cell design could observe and study electrochemical phenomena of the solvated samples in the TEM. Advances in design and preparation techniques decreased the liquid and window thickness even further, making high resolution imaging in liquids possible (Figure 1.1c). This technique, now known as liquid cell transmission electron microscopy, or the liquid cell, grew in popularity and is becoming a well-known technique to study materials in liquid.

1.3 Types of Liquid Cells

Today, there are several types of liquid cells that are commonly used, which each have their own strengths and limitations. These liquid cell configurations could most easily be broken down into three main classes: 1) SiN_x microfabricated liquid cells, and 2) TEM grid-based sandwich liquid cells, and 3) Next-generation liquid cells.

SiN_x Microfabricated Liquid Cells

Apart from the seminal 1944 work, the SiN_x microfabricated liquid cells were the first type commonly used and developed. These liquid cells consist of three main components; two chips, each with a thin, electron transparent SiN_x window and a thicker Si support, and O-rings to create a hermetic seal. The windows of these liquid cells are prepared using microfabrication techniques, which allows the thickness to be very thin. The windows of these liquid cells are prepared by taking a Si wafer with SiN_x on top, and etching away the silicon in a small region to leave a thin, electron transparent SiN_x membrane which is used as the window. The rest of the Si around the SiN_x provides stability and encloses the bulk liquid. These liquid cells were originally prepared individually, but today are readily available commercially. As they are commercially available, they are straightforward to prepare after proper training, results can be quite reproducible, and physical parameters of the cells, such as window thickness, liquid thickness, and liquid volume are well known and well controlled.

While these liquid cells are highly controllable, they suffer from thick water layers, mostly due to bulging at the middle of the window due to the pressure differential of the liquid layer. The increased thickness of the liquid layer decreases the achievable resolution, and sometimes even visibility. While there are ways around this, such as creating smaller windows to minimize bulging, or imaging at the corners where the liquid layer is the thinnest, these methods limit the available area to study the desired system, which may mean that more samples and more time are needed to generate adequate data.

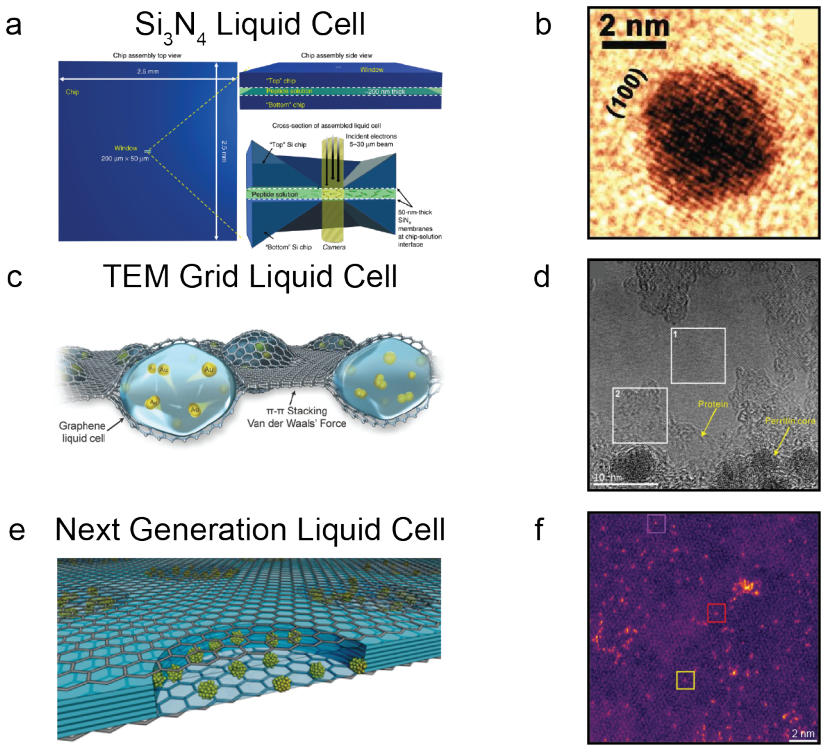

Figure 1.2: a) SiN_x liquid cell schematic (reproduced with permission from[19], Copyright 2019 Touve *et al.*) and b) a high resolution image from a SiN_x liquid cell (reproduced with permission from[20], Copyright 2014 The American Association for the Advancement of Science). c) Graphene liquid cell schematic (reproduced with permission from[21], Copyright 2017 John Wiley and Sons) and d) a high resolution image from graphene liquid cell (reproduced with permission from[22], Copyright 2014 WILEY-VCH Verlag GmbH Co. KGaA, Weinheim). e) Next generation microfabricated liquid cell schematic (reproduced with permission from[23], Copyright 2018 American Chemical Society) and f) a high resolution image from a next generation microfabricated liquid cell (reproduced with permission from[24], Copyright 2022 Clark *et al.* under exclusive license to Springer Nature Limited).

TEM Grid-Based Liquid Cells

The other common liquid cell type is one based on two TEM grids sandwiched together. The most prevalent of these types is what is called the graphene liquid cell, where two TEM grids are first coated with single to few layer graphene, then a small droplet of solution is encapsulated between these two grids.[18,25] With this type of liquid cell, the strong van der Waals forces between the two graphene sheets, rather than an o-ring, make a hermetic seal that will protect the droplet from the high vacuum of the TEM. While the graphene liquid cell is the most common type of this sandwich based liquid cell, more recently new types of liquid cells using different grids that do not require a graphene coating have emerged. These have been called the amorphous carbon, or carbon film liquid cells, and use plasma treated carbon TEM grids to encapsulate the desired solution.[26]

These graphene liquid cells have many advantages over the SiN_x liquid cells, namely that the resolution is significantly better. In all the TEM grid-based liquid cells, the thickness of the windows (either graphene or carbon film) are between 1-20 nm, whereas for the SiN_x liquid cells, the windows are typically 50-200 nm thick. Additionally, the thickness of the liquid layer is typically on the order of 10s of nm,[25,27–29] while the thickness of the liquid layer in SiN_x liquid cells is several hundred nm, and can be over a micron thick in the center of the window.[30–33] However, one major limitation of these TEM grid-based liquid cells is that they lack reproducibility. The liquid pockets of these liquid cells form stochastically, meaning that the size, shape, thickness, and volume of these pockets varies with each sample that is made.[27,28,34–36] In practice, this means that one needs to study a system where these parameters wouldn't be expected to affect the system, or ample time must be spent searching for liquid pockets of similar geometry. Further, these liquid cells are formed through an evaporative drying process where a droplet of the solution is placed on one of the grids, then the other grid is placed on top. As the excess solution evaporates, the two grids are brought into close contact to form the seal. This formation process indicates that the nature of the encapsulated solution may be different from the original solution as evaporation may be significant. This is discussed a great detail in Chapter 3.

Next Generation Liquid Cells

In the past few years, scientists have begun developing next generation liquid cells that combine the advantages of SiN_x and graphene liquid cells. These liquid cells are microfabricated to contain wells with well defined volumes, but the window layer is single to few layer graphene, or another thin material such as monolayer MoS_2.[23,24,37] These liquid cells have the reproducibility of the size, shape, and volume of the liquid cells as the wells can be constructed at will, but by using the thin window layers, can still reliably obtain high resolution images and videos, down to single adatom resolution.[24]. The main limitation of these liquid cells is that they are not commercially available, and they require significant effort and cost to prepare individually. It will be interesting to see if these types of liquid cells become commercialized in the future, as that would open up the field to more reproducible,

high resolution work, and would likely draw even more attention and researchers to use this technique.

1.4 Water Radiolysis

When a liquid cell is placed inside a TEM and the electron beam is turned on, the liquid solution is no longer chemically identical to the same stock solution left on the benchtop. The electron beam is a form of ionizing radiation and when it is introduced to the solution, it will ionize the water present. This presents major considerations for the liquid cell technique, and understanding the radiation chemistry present is a must to understand how this will affect the system of interest. The precise nature of the radiation chemistry depends greatly on the solvent used. There are reviews that describe the radiation chemistry of some common organic solvents,[38] but the majority of research, including the work that will be described in Chapters 2 and 3 use water as the solvent, which will be the focus here.

Formation of the Primary Products

When a high energy electron beam interacts with water, energy is transferred to the water, creating excited state water molecules. Several ps later, the water molecules decompose in the path of the individual electrons, to create inhomogenously distributed reactive intermediates. When sufficient energy is deposited into the water, as is common in liquid cell TEM, several of these reactive intermediates are formed within 10s of ångstroms of each other in what is known as a *spur*.[39–43] These intermediates react to form products within these spurs such as the hydrogen radical $^{\bullet}H$, the hydroxyl radical $^{\bullet}OH$, and H_2 which are known as the *initial yield*. After about 10^{-11} to 10^{-10} seconds, these species of the initial yield then diffuse and react further to form the primary products,[44–47] as described in Equation 1.3

$$H_2O \rightsquigarrow e^-_{aq}, {}^{\bullet}OH, H_2O_2, {}^{\bullet}H, H_3O^+, {}^{-}OH, HO_2{}^{\bullet}, H_2 \tag{1.3}$$

After about 1 μs, the primary products are homogeneously distributed within the water. The system can then be described as containing a certain concentration of these primary products,[39] which are described by their *g-values*. The G-value is a term that denotes how many molecules have been consumed or destroyed per 100 eV of energy absorbed.

Chemical Reaction Network

When neat water is irradiated, eight primary products are formed. These species can then diffuse throughout the system and take part in a cascade of slower chemical reactions, forming an additional seven species. Already, several dozen chemical reactions are needed to describe the interactions between these 15 species and water. Further, any solutes present increase the number of chemical reactions needed to describe the environment, and it quickly becomes apparent that this is an unreasonable task to perform by hand. Particularly for

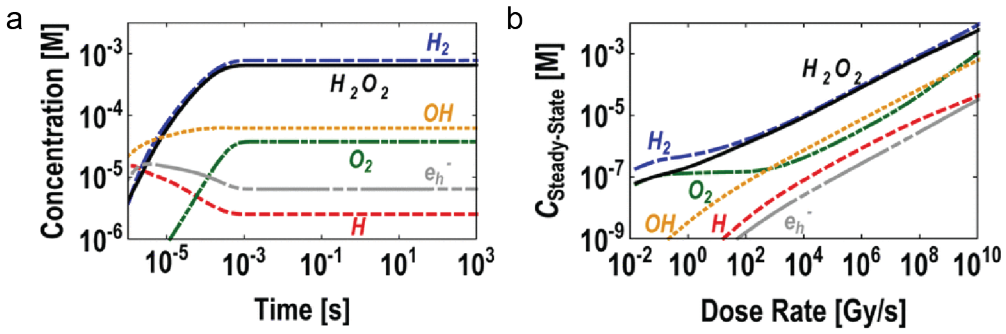

Figure 1.3: a) Concentration of primary products with time and b) steady state concentration of primary products with dose rate. Reproduced with permission from[48], Copyright 2014 American Chemical Society

liquid cell TEM, the relevant processes under observation occur on the time scale of seconds to minutes to 10s of minutes, whereas most radical reactions occur several orders of magnitude faster. To understand how these dozens of interrelated reactions interact with one another to develop the reaction environment, a kinetic model is commonly used. This type of kinetic model was first developed by Elliot, and McCracken[44] in 1990, but has more recently been adapted to and expanded in MatLAB[48].

After adaptation of this model to MatLAB in 2014,[48] this chemical reaction network has become a predominant method for for understanding the radiation chemistry in the liquid cell. This model can predict the radiation chemistry present in the liquid cell by solving the following partial differential equation.

$$\frac{\delta C_i}{\delta t} = D_i \nabla^2 C_i - \sum_j k_{ij} C_i C_j + \sum_{j,k \neq i} k_{jk} C_j C_k + R_i \tag{1.4}$$

In Equation 1.4, the first term represents the diffusion of species i in water, the second and third term, respectively, relate to the production and destruction of species i through chemical reactions with rate constants k_{xx}, and the last term is the electron beam induced generation of chemical species. The electron beam induced generation is determined according to Equation 1.5.

$$R_i = f_i \rho \psi G_i \tag{1.5}$$

Where f_i is the molar fraction of water, ρ is the liquid density, ψ is the electron dose rate, and G_i is the G-value for chemical species.

By solving this partial differential equation for every species i in the system, factors such as the concentration over time can be calculated (see Figure 1.3a). Further, the concentration of various species as a factor of dose rate can be calculated as well (see Figure 1.3b), a parameter that is readily controlled with the TEM.

Here, it is important to point out precise definitions of certain terminology used to describe the number of electrons interacting with the sample. In the field of radiolysis, the term *dose rate* is commonly used and is defined as the amount of energy *absorbed* by the sample in a given period of time. The units for this are commonly Grays/second, where 1 Gray (Gy) is 1 Joule of energy absorbed per kilogram. Importantly, in electron microscopy, it is very difficult to calculate how much energy is being directly absorbed by the sample, but it is much easier to determine how much energy is being imparted on the sample. This is a metric which can be defined as *electron flux* which is the number of electrons hitting the sample per unit area per unit time, and typically has units $e^{-}Å^{-2}s^{-1}$. The seminal radiation chemistry literature has been used to inform the liquid cell TEM community, and this is done by equating the Gy/s dose rates to the $e^{-}Å^{-2}s^{-1}$ electron fluxes. These two metrics are precisely equal *if* every electron imparted on the sample in the TEM is absorbed by the sample, but in the vast majority of cases, this is not true. However, without a straightforward method to calibrate how many of the electrons are being absorbed by the sample for each sample, drawing these analogies where possible is a good first order approximation. Ultimately, many liquid cell TEM studies that are dependent on the electron flux look at trends in the transformation to determine differences between higher energy and lower energy processes.

1.5 Radiolysis and Redox Chemistry

Understanding the relative concentrations of these water radiolysis products in the liquid cell is important, but ultimately the goal is to understand how these radiolysis products may or may not affect the samples we are trying to observe. A straightforward method to understand how these radical species may interact with any samples added to the system is to look at their reduction potentials. The reduction potential is a measure of the tendency of a species to gain an electron and become reduced, and is measured in Volts (V). If a material has a high tendency to become reduced, it's reduction potential will be a large negative number. If a material has a high tendency to become oxidized, it will have a high positive number. All of these numbers are relative to some reference electrode, commonly the standard hydrogen electrode (SHE).

The reduction potentials are half reactions, so to understand whether a chemical reaction will take place between a radical species and a sample, we can combine a half reaction for a radical species and a half reaction for a sample. To keep the calculations straightforward, we will just be looking at simple metals interacting with the radicals. A list of the water radiolysis products and their reduction potentials are listed in Table 1.1 and a list of simple metals and their reduction potentials are listed in Table 1.2.

To determine whether a chemical reaction will be spontaneous (*i.e.* will occur), a reduction and oxidation half reaction are added together, ensuring the electrons are canceled out. When a reaction is reversed, so is the sign of the reduction potential. Then, the two reduction potentials are added together. If this number is positive, then the reaction is

Half Reaction	Reduction Potential (V)	Reference
$e^- \rightleftharpoons e^-_{aq}$	-2.88	[49]
$H^+ + e^- \rightleftharpoons H^\bullet_{aq}$	-2.31	[49]
$HO^\bullet_2 + e^- + H^+ \rightleftharpoons H_2O_2$	+1.46	[49]
$HO^\bullet + e^- + H^+ \rightleftharpoons H_2O$	+2.73	[49]
$HO^\bullet + e^- \rightleftharpoons HO^-$	+1.90	[49]

Table 1.1: Reduction Potentials of Select Water Radiolysis Products

Half Reaction	Reduction Potential (V)	Reference
$Li^+ + e^- \rightleftharpoons Li$	-3.04	Atkins, and Shriver[50]
$Ti^{3+} + 3e^- \rightleftharpoons Ti$	-1.37	Aylward, and Findlay[51]
$Zn^{2+} + 2e^- \rightleftharpoons Zn$	-0.76	Bard[52]
$Fe^{2+} + 2e^- \rightleftharpoons Fe$	-0.44	Atkins[53]
$Cu^{2+} + 2e^- \rightleftharpoons Cu$	+0.16	Bard[52]
$[PtCl_4]^{2-} + 2e^- \rightleftharpoons Pt + 4Cl^-$	+0.77	Bard, and Falkner[54]
$Pt^{2+} + 2e^- \rightleftharpoons Pt$	+1.19	Bard, and Falkner[54]
$[AuCl_4]^- + 3e^- \rightleftharpoons Au + 4Cl^-$	+0.93	Bard[52]
$Au^{3+} + 3e^- \rightleftharpoons Au$	+1.52	Bard[52]

Table 1.2: Reduction Potentials of Select Simple Metals

spontaneous and thermodynamically will occur, if it is negative it will not.

As a simple example, let's look at the reaction between the hydroxyl radical and metallic copper. Using the tables, we see that the two half reactions we are considering are as follows:

$$HO^{\bullet} + e^{-} \rightleftharpoons OH^{-}; +1.90V \tag{1.6}$$

$$Cu^{2+} + 2e^{-} \rightleftharpoons Cu; +0.16V \tag{1.7}$$

The full chemical reaction we are considering is then

$$2HO^{\bullet} + Cu \rightleftharpoons Cu^{2+} + 2OH^{-} \tag{1.8}$$

and the electrochemical potential for this reaction is

$$E = +1.90V + (-0.16V) = +1.74V \tag{1.9}$$

As the electrochemical potential for this full reaction is highly positive, this reaction will occur spontaneously.

After a quick inspection of Tables 1.1 and 1.2, it is obvious that many of the water radiolysis products have very large potentials, either positive or negative, while the majority of the simple metals have more moderate potentials. Even the noble metals which are known for their inertness and stability can be oxidized by the hydroxyl radicals, particularly if there is a complexation agent such as chloride present.

Evidently, the radical environment present in liquid cell TEM is extremely harsh. Radiolysis from the electron beam produces a wide variety of radicals and reactive species which have large potentials capable of transforming even noble metals. From the kinetic chemical reaction network, we know that as we increase the dose rate, that the steady state concentration of these species will increase. If we assume that the electron flux is equal to the dose rate, and an electron flux of 100 $e^{-}Å^{-2}s^{-1}$ is used for a particular experiment (this is much lower than what would commonly be used for high resolution imaging), this corresponds to a dose rate of 1.4×10^{8} Gy/s. For reference, acute radiation poisoning with a LD100 occurs when >10 Gy are absorbed over the course of a few minutes,[55] and the worst hit areas of the Chernobyl Nuclear meltdown were estimated to endure radiation levels of approximately 650 Gy/s.[56] So then, with extremely high levels of radiation, and the continuous generation of reactive radical species, how does one obtain any relevant information about the system?

1.6 Controlling Radiolysis

Due to the extreme radiation chemistry that the liquid cell faces, there has been significant work in developing methods to mitigate the effects of radiolysis. Largely, the community has worked to develop methods to decrease the electron flux imparted on the sample, or to scavenge the radiolytically produced species. However, it is also possible to use the effects

of radiolysis to induce specific changes in the system of interest, and leverage that to learn more about the fundamental chemistry presiding over that system.

Mitigating Radiolysis

Reducing the effects of radiolysis on the sample has been of prime interest in the community from the beginning. One method of doing so is to add species to the solution which alter the chemistry of the solution. An example of this is to use radical scavengers to reduce the concentration of radicals in the solution. While this technique has been used for a long time with other types of radiolysis to control the solution chemistry,[43,57–59] examples of using radical scavengers in the liquid cell is somewhat limited. One reason for this could be that the radical scavengers used typically create a byproduct that is also disruptive to the system. For instance, alcohols are oftentimes used to scavenge hydroxyl radicals as they are known to react through a hydrogen abstraction mechanism to form water and a new organic radical species.[43] These species depend on the identity of the original alcohol, but typically have reducing potentials, which can generate a net reducing environment by scavenging the highly oxidizing hydroxyl radicals to create excess reducing species. While this can be a useful method to specifically study a reduction process, the effects of radiolysis are still present.

This effect is exemplified in a study of a galvanic exchange reaction in the liquid cell.[33] It was noted that Ag nanocrystals in a $PdCl_2$ solution participated in a galvanic exchange reaction in the liquid cell, very similarly to what occurs bench top, but the rate of reaction was significantly faster (Figure 1.4a). To understand the effect of the electron beam on the galvanic exchange, isopropanol was added to scavenge the radiolytically produced hydroxyl radicals, and it was noted that the galvanic exchange no longer occurred. Instead, as a net-reducing environment was generated, the Pd deposited on the Ag nanocrystals to create a Ag/Pd core/shell nanocrystal (Figure 1.4b). In this study, the use of the radical scavengers appeared to successfully scavenge the oxidizing hydroxyl radicals, but ultimately prevented the observation of the desired transformation. However, as work employing these radical scavengers in the liquid cell is somewhat limited, it would be an interesting future direction to see if a mix of scavengers could be used to limit the effects of radiolysis in the liquid cell.

Additionally, the windows of the liquid cells themselves are known to have an effect on the radiolytic activity of the solution. There are a few critical differences between SiN_x membranes and graphene or carbon membranes used in liquid cells. To begin, the SiN_x membranes are relatively thick and composed of a higher atomic number material than graphene or carbon membranes. This indicates that the SiN_x windows will act as a source of secondary electrons (electrons ejected from the membrane due to inelastic scattering) which can increase the effects of radiolysis in SiN_x liquid cells.[61–63] Further, graphene has shown to have radical scavenging abilities which decreases the radiolytic load of the solution.[60,64–66] DNA superlattices, which are sensitive to radiation damage, were shown to maintain their structure in graphene liquid cells, or SiN_x liquid cells with graphene coated windows, compared to bare SiN_x windows.[60] *Ex situ* Raman showed that the graphene degraded after the

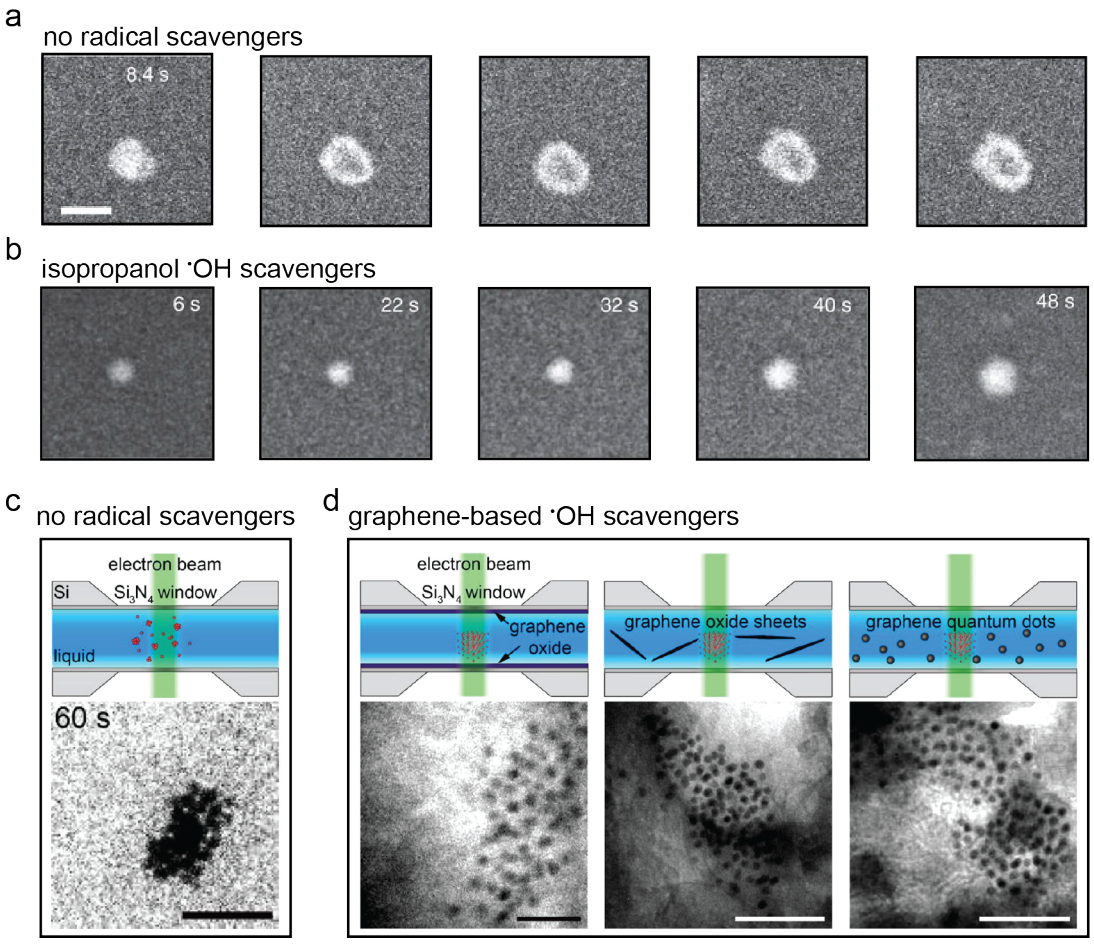

Figure 1.4: a) Evolution of a Ag nanocrystal in a $PdCl_2$ solution. The nanocrystal undergoes a galvanic exchange reaction which causes a hollow structure to form. b) Evolution of a Ag nanocrystal in a $PdCl_2$ solution and isopropanol. The isopropanol scavenges the radiolytically produced hydroxyl radicals which minimizes the oxidation of the Ag, and encourages Pd reduction on the surface to grow the nanocrystal larger (a) and b) reproduced with permission from[33], Copyright 2014 Nature Publishing Group, a division of Macmillan Publishers Limited. All Rights Reserved.). c) Au-DNA superlattice aggregating in a SiN_x liquid cell under electron beam irradiation. d) Au-DNA superlattice maintaining it's structure under electron beam irradiation in a SiN_x liquid cell with various graphene-based scavengers (c) and d) reproduced with permission from[60], Copyright 2017 American Chemical Society).

liquid cell experiment, indicating that the graphene chemically reacts with the radiolysis products, which can help protect the samples from radiation damage.[60]

The above discussion indicates that there are steps that users can take to mitigate the effects of radiolysis, by using certain additives or graphene liquid cells to scavenge radiolysis products. However, these techniques are limited in their scavenging capacity. Alcohols and and other radical scavengers react through an irreversible process, so an excess of alcohol is needed to prolong the scavenging effects. Additionally, the reaction of graphene with hydroxyl radicals is known to form holes in the graphene layer,[65], which can cause the liquid to evaporate out of the system. Using multi-layer graphene could help prevent leakage, but ultimately there is not currently a scavenging methods that will completely negate the effects of radiolysis in the liquid cell.

Utilizing Radiolysis

While completely mitigating the effects of radiolysis would allow users to study their systems in their native liquid environments, experimentally that is not yet possible. However, radiolysis could also be used as a tool to purposefully induce changes, to understand fundamentals about a system. Perhaps the simplest and most prominent example of this in the nanomaterials community is using the reducing effects of electron beam induced radiolysis to grow nanocrystals in solution. There have been several examples of electron beam induced growth of nanocrystals since the recent resurgence of liquid cell electron microscopy.[17,18,20,67–73] For these beam-induced growth processes, a highly reducing species, such as the solvated electron, reacts with a preloaded metal salt to reduce the metal atom, as described in Equation 1.10 below.

$$M^+ + e^-_{aq} \rightarrow M^0 \tag{1.10}$$

This process continues until the metal atoms aggregate and begin to grow and form nanocyrstals. When synthesizing metal nanocrystals on the benchtop, the reductant used is not solvated electrons, but the liquid cell studies have still informed bench top syntheses. For instance, an early study looked at beam initiated growth of Pt nanocrystals in the liquid cell. This study found evidence of non-classical growth mechanisms where two small nanocrystals merged together, stopped growth for a certain waiting time, then continued to grow to form a monodisperse yield of nanocrystals.[74] This study provided direct experimental evidence of non-classical growth behavior of nanocrystals.

Additionally, techniques have been developed to study the reverse process, nanocrystal etching in liquid cell TEM. The advantage of studying the etching processes in the liquid cell is that the experiment begins with a well defined, pre-characterized nanocrystal. This makes it much more straightforward to characterize changes in the nanocrystal, as the shape, orientation, zone axis, and other parameters are already known. Additionally, studying nanocrystal etching in the liquid cell is one way to look at some fundamental characteristics of the nanocrystals, such as the relative reactivity of different surface facets, and

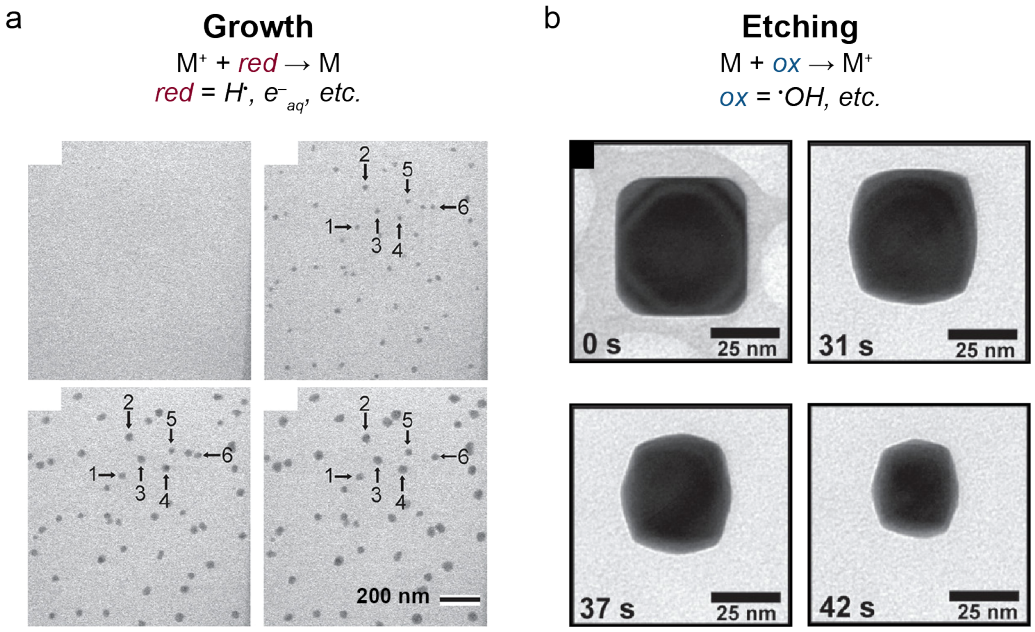

Figure 1.5: a) Example of growth of nanocrystals in the liquid cell (reproduced with permission from[75], Copyright 2012 American Chemical Society) and b) etching of nanocrystals in the liquid cell (reproduced with permission from[76], Copyright 2018 American Chemical Society)

potential degradation pathways. To study etching processes in the liquid cell, the oxidizing radiolysis products, mainly hydroxyl radicals, are used to induce changes in the system. This is performed sometimes through tuning the electron flux,[48], but more commonly through the use of an Fe^{3+} additive.[76–81] It was thought that Fe^{3+} could induce this oxidizing environment by scavenging the radiolytically produced solvated electrons, and converting them to additional hydroxyl radicals through Fenton's mechanism,[77] although experimental evidence of this was lacking. Work to understand the role of iron in the oxidative etching of metal nanocrystals in the liquid cell is presented in Chapter 2.

1.7 Directly Measuring Chemical Species

Reproduced in part with permission from: Crook, M. F; Moreno-Hernandez, Jamali, V.; Alivisatos, A. P. "Recent Advances in the Study of Colloidal Nanocrystals Enabled by *In Situ* Liquid Phase Transmission Electron Microscopy" *MRS Bulletin* **2022**, 47, 3, 305-313

The majority of the understanding of the chemical environment in liquid cell electron microscopy comes from findings of the water radiolysis community. Users rely heavily on the model described in 1.4 to understand their system. This model has been instrumental to the field and has been widely adopted, added to, and specialized to understand specific

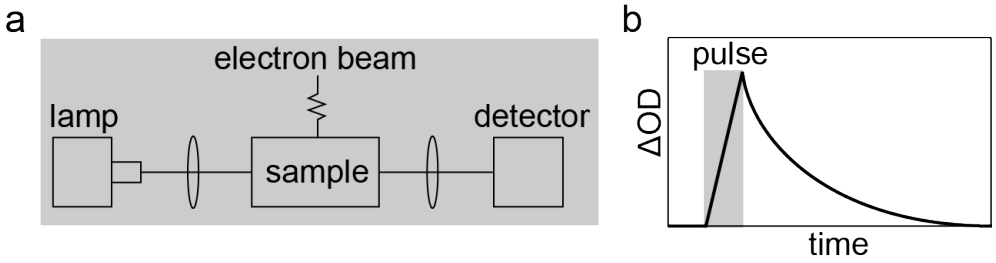

Figure 1.6: a) Schematic of pulse radiolysis set up and b) Schematic of example pulse radiolysis spectrum (reproduced with permission from[87], Copyright 2022 Moreno-Hernandez *et al.*, under exclusive License to the Materials Research Society).

systems.[72,82–86] While this is very informative, the outputs of this model have not been experimentally validated inside the liquid cell. Measuring the concentration, or even probing the presence of the molecular and ionic radiolysis products in the liquid cell is extremely challenging. Instead, much of the work in understanding the chemical environment has used some sort of beam-sensitive probe, such as nanocrystal growth or etching, to induce whether the environment is predominately reducing or oxidizing, then hypotheses about the relevant reactions are built from there. Moving forward, gaining deeper understanding of the liquid cell environment will necessitate correlative techniques that can provide insights into the relevant chemistry. Herein, two techniques which show promise are described.

Pulse Radiolysis

The chemical reaction network discussed heavily in this Chapter is based off of results from pulse radiolysis experiments, many performed several decades ago. Pulse radiolysis is a technique where a source of ionizing radiation, often times an electron beam, is coupled to a time resolved spectroscopic measurement[88] (Figure 1.6a). In pulse radiolysis, the difference in absorption before and after the radiation pulse is measured, to determine the changes to the system after the pulse (Figure 1.6b). This is how all of the reactions and rate constants that are used in the kinetic radiolysis models today were determined. The advantage of pulse radiolysis, when compared to the information that liquid cell TEM can offer, is that it can measure any species that has visible absorption, including certain molecules and ions, which are invisible in the TEM. In this way, pulse radiolysis can provide insight on the species interacting with the sample and driving the observed chemistry. It seems that pulse radiolysis would be a useful technique to begin to understand the complex chemistry of the liquid cell, but as of the start of this thesis project, these two techniques have never been used in conjunction.

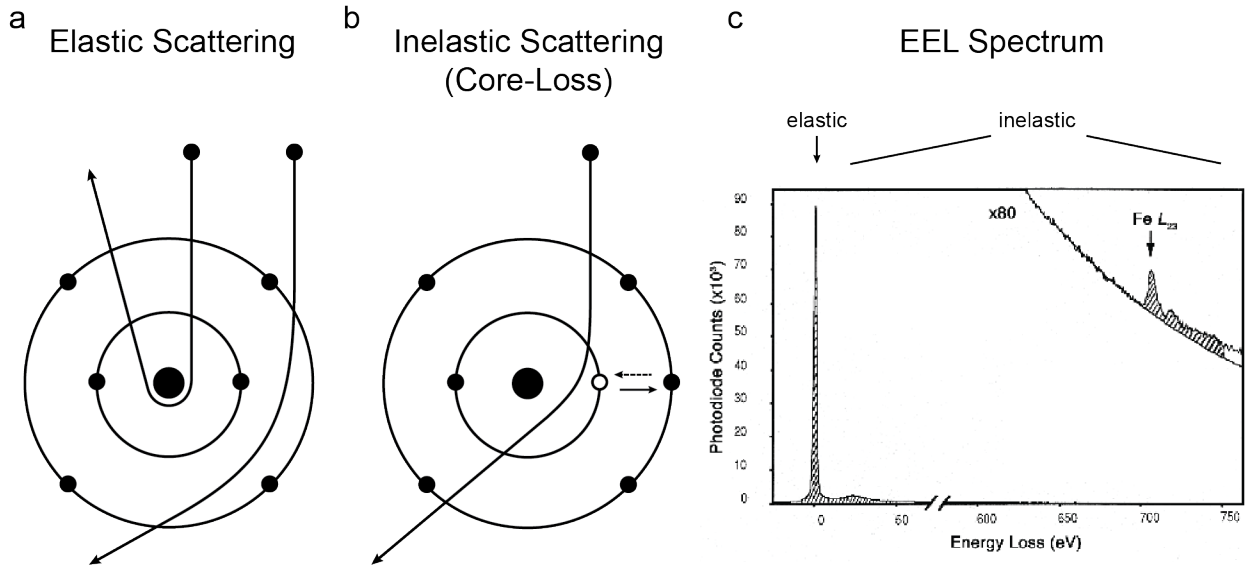

Figure 1.7: a) Schematic of elastic scattering process. b) Schematic of inelastic scattering process (a) and b) adapted with permission from[89], Copyright 2011 Springer Science Business Media, LLC). c) Example of EEL spectrum (adapted with permission from[90], Copyright 2005 John Wiley and Sons).

Electron Energy Loss Spectroscopy

Another option is to use the built-in spectroscopies offered by the electron microscope, including X-ray Energy Dispersive Spectroscopy (EDS) and Electron Energy Loss Spectroscopy (EELS) to further understand the system. While EDS and EELS are both methods with elemental selectivity, EELS is also sensitive to chemical changes, providing it with added benefits when studying the solution chemistry.

EELS operates through measuring the energy of the electrons after passing through the sample. When a high energy electron interacts with matter, it can undergo two main processes. Firstly, it can be *elastically scattered* where it is weakly scattered or diffracted by the sample and does not lose any energy (Figure 1.7a). Alternatively, the electrons can be *inelastically scattered* where, for one example, the incoming beam can excite a core electron to a higher energy state (Figure 1.7b). The electron from the electron beam will lose a characteristic amount of energy that corresponds to the energy of this transition. These *energy losses* are characteristic to the elements, and can shift in energy and/or change in fine structure depending on the oxidation state, or immediate chemical environment.[90] In practice, these energy losses are collected and are commonly characterized by a high intensity zero-loss peak (ZLP) which corresponds to the elastically scattered electrons, and higher energy features which correspond to inelastically scattered electrons (Figure 1.7c). This sensitivity would make EELS a prime method to study the solution chemistry inside the liquid cell, *in situ*.

While EELS is a powerful technique to study chemistry inside the liquid cell, the most common uses of EELS are to verify the presence of water through the O K-edge[23,34,91] and to measure the liquid thickness.[23,30,92] However, EELS has been proven to be a powerful technique to track radiolysis effects on nanomaterials. Jungjohann et al. tracked the O K-edge from water during continuous irradiation from an electron-beam probe.[93] Modulation of the pre-edge peak at 528 eV indicated variability in the oxygen bonding environment and distortion of the hydrogen bonding network in water due to radiolysis damage. Additionally, another study by Wang *et al.* tracked the Fe L-edge of a ferritin particle in a graphene liquid cell to determine the oxidation state of iron in the hydrated state.[22] By trapping the protein in a biocompatible liquid cell, the reduction of Fe^{3+} to Fe^{2+} in the iron oxide core could be distinguished, indicating that the biological function of the protein is not affected under irradiation.

These correlative methods have been powerful tools to deepen our understanding of the system, but there is still a big opportunity to use these techniques to deepen our understanding of the solution environment in liquid cell TEM.

1.8 Putting it all Together:

Here, we now understand the motivations for using liquid cell transmission electron microscopy, it's advantages, and how radiolysis affects these measurements. From here, there are opportunities to grow the field by better understanding and quantifying the chemical environment within graphene liquid cells in particular. In Chapter 2, we begin by exploring a model system in graphene liquid cells, gold nanocrystal etching using an Fe^{3+} additive. In this chapter, we expand upon previous work to understand how common halide additives may affect the results of gold nanocrystal etching experiments. Additionally, we use pulse radiolysis to probe the role of the Fe^{3+} additive, and propose a mechanism for how it induces etching in the liquid cell. In Chapter 3, we focus on a slightly different system, a Ce^{3+} additive used to induce etching of gold nanocrystals in the liquid cell. Here, we use EELS to directly probe the role of the Ce^{3+} additive with time resolved measurements. Additionally, as EELS is an *in situ* technique, it is used to directly probe the concentration of the Ce^{3+} additive within the graphene liquid cell, providing experimental measurements of the solution chemistry in the liquid cell.

Chapter 2

Elucidating the Role of Chemical Additives Using Liquid Cell TEM and Pulse Radiolysis

Reproduced in part with permission from: Crook, M. F; Laube, C.; Moreno-Hernandez, I. A.; Kahnt, A.; Zahn, S.; Ondry, J.; Liu, A.; Alivisatos, A. P. "Elucidating the Role of Halides and Iron During Radiolysis-Driven Oxidative Etching of Gold Nanocrystals Using Liquid Cell Transmission Electron Microscopy and Pulse Radiolysis" *Journal of the American Chemical Society* **2021**, 143, 30, 11703-11713

Graphene liquid cell transmission electron microscopy (TEM) has enabled the observation of a variety of nanoscale transformations. Yet understanding the chemistry of the liquid cell solution and its impact on the observed transformations remains an important step toward translating insights from liquid cell TEM to benchtop chemistry. Gold nanocrystal etching can be used as a model system to probe the reactivity of the solution. $FeCl_3$ has been widely used to promote gold oxidation in bulk and liquid cell TEM studies, but the roles of the halide and iron species have not been fully elucidated. In this work, we observed the etching trajectories of gold nanocrystals in different iron halide solutions. We observed an increase in gold nanocrystal etch rate going from Cl^-- to Br^-- to I^-- containing solutions. This is consistent with a mechanism in which the dominant role of halides is as complexation agents for oxidized gold species. Additionally, the mechanism through which $FeCl_3$ induces etching in liquid cell TEM remains unclear. Ground-state bleaching of the Fe^{3+} absorption band observed through pulse radiolysis indicates that iron may react with $Cl_2^{\bullet-}$ radicals to form an oxidized transient species under irradiation. Complete active space self-consistent field (CASSCF) calculations indicate that the $FeCl_3$ complex is oxidized to an Fe species with an $^{\bullet}OH$ radical ligand. Together our data indicate that an oxidized Fe species may be the active oxidant, while halides modulate the etch rate by tuning the reduction potential of gold nanocrystals.

2.1 Introduction

The morphology of gold nanocrystals (AuNCs) can be controlled with high precision with careful control of the synthetic environment. Minute changes in precursor concentration,[94–97] or ppm-level impurities,[98,99] can drastically change or completely inhibit nanocrystal formation. This sensitivity to the environment has been exploited to create a variety of different nanocrystal morphologies.[96,100–102] This literature forms a foundation that enables a reverse approach. In systems where the chemical environment is not well understood or is challenging to probe, the evolution of presynthesized gold nanocrystals can be used as a tool to deduce the reactive species in the chemical environment.

One environmental system that has remained challenging to probe is the solution in liquid cell transmission electron microscopy (LCTEM). LCTEM is a technique where a solution is hermetically sealed between two electron transparent SiN_x membranes,[74] two graphene-coated TEM grids,[18] or amorphous carbon windows,[26] enabling *in situ* imaging of nanocrystal transformations in solution. LCTEM has led to discoveries of new methods of crystal growth,[18,74] kinetic intermediates of gold nanocrystals,[76,77,79] and the precise atomic structure of individual solvated nanocrystals,[82,103] yet probing the solution chemistry in these systems has remained a challenge. Radiolysis induced by an electron beam is thought to dominate the chemistry in LCTEM and is challenging to replicate *ex situ*, and chemical intuition from traditional chemistry often does not hold during radiolysis. However, with careful experimental design, gold nanocrystals can be used as a chemical probe to elucidate the major reactive species present in LCTEM.

When a high-energy electron beam irradiates an aqueous solution, it produces a variety of radiolytic products, including $^{\bullet}OH$, H_2O_2, and $^{\bullet}H$, among others.[39–41] Schneider *et al.* developed a kinetic model to understand how the electron electron flux affects the concentrations of different radiolytic species.[48] They showed that, by switching from a low electron flux to a high electron flux regime, the liquid cell can be modulated from an oxidizing to a reducing environment, respectively, by altering the balance of highly oxidizing species ($^{\bullet}OH$) and highly reducing species (e^-_{aq}). Experimentally, it was shown that, in the high electron flux regime, the etch rate of gold nanocrystals is directly dependent on the electron electron flux,[77] indicating a close relationship between gold nanocrystal etching and radiolytic products.

In typical graphene LCTEM etching experiments preformed previously in our group, the encapsulating solution contains HCl to control the stability of AuNCs[104] and prevent hydrolysis of added metal salts.[76,77,79] It is well known that the vast majority of hydroxyl radicals ($> 90\%$) are scavenged in the presence of halides to produce halide-based radicals.[105–113] When halides scavenge hydroxyl radicals, the major radical product is $X_2^{\bullet-}$, where X = Cl, Br, or I.[108] Furthermore, bromide and iodide are far more efficient radical scavengers than chloride, as the intermediate formed from the initial reaction between halides and hydroxyl radicals primarily reverts back to the initial state in the case of chloride. For bromide and iodide, this intermediate is stabilized and continues reacting to form $Br_2^{\bullet-}$ and $I_2^{\bullet-}$ radicals. Consequently, the concentration of bromide- or iodide-containing radicals in solution will

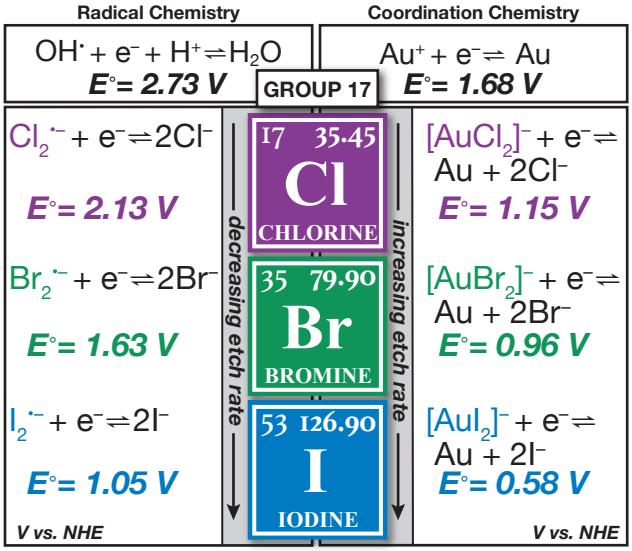

Figure 2.1: Radical chemistry versus coordination chemistry hypotheses for the effect of halides on AuNC etching in LCTEM

be greater than that of chloride-containing radicals, even with a 600-fold greater concentration of chloride ion present.[108] This means that even minute quantities of bromide or iodide present in the encapsulating solution of LCTEM can drastically alter the radiolytic environment.

One hypothesis is that the highly oxidizing hydroxyl radicals are responsible for etching gold nanocrystals in graphene LCTEM.[76,77,79,81] If this were the case, the etch rate would be modulated with chemical additives to alter the power of the oxidant. When halides scavenge hydroxyl radicals, the standard reduction potential is drastically reduced from $^{\bullet}OH$ to $I_2^{\bullet-}$ ($E(^{\bullet}OH/{-}OH) = 2.73$ V vs $E(I_2^{\bullet-}/2I^-) = 1.05$ V), indicating a marked decrease in the strength of the oxidant (Figure 2.1, left). Accordingly, one would expect the average etch rate of the gold nanocrystals to decrease in the presence of heavier halides.

A second hypothesis for the role of halides in LCTEM etching studies is their possible function as complexation agents for oxidized gold ions, thus serving to stabilize the products of the oxidation. The addition of heavier halides to the system can lower the reduction potential of gold by ca. 600 mV (Figure 2.1, right). This would present itself as an increase in etch rate in the presence of heavier halides, which is the opposite of the trend expected for the halides if their radical species are acting as the oxidizing agents for the gold nanocrystal. By observing the trend in etch rate of AuNCs as heavier halides are added, the dominating mechanism can be elucidated. Further, it is critical to understand the role of halides in LCTEM experiments, as halides are present as HCl in the encapsulating solution or through an ionic surface ligand (i.e., cetyltrimethylammonium bromide (CTAB)). Additionally, as halides from halide-containing ligands such as CTAB would introduce minute quantities of

halides, it is important to understand the role of substoichiometric concentrations of halides in graphene LCTEM etching experiments of AuNCs. Although the effects of halides in LCTEM of AuNCs have been acknowledged,[38,82,104,114] the highly nonlinear effects in halide mixtures warrant careful study to elucidate the relative role of complexation and radical chemistry to the observed etching trajectories.

While careful observation of nanocrystal etching trajectories in different chemical environments provides a route to understand the etching chemistry, it is unable to identify the key reactive chemical intermediates (*i.e., radiolysis products*) that are responsible for etching. Pulse radiolysis is a technique in which a high-energy pulsed electron beam irradiates a solution of interest that is probed by time-resolved optical spectroscopy. Through this technique, a solution can be irradiated with the same radiation source and at a peak electron flux that is approximately the same as the steady-state electron flux of LCTEM (4.25 $\times 10^9$ Gy/s peak in pulse radiolysis vs 1.14 $\times 10^9$ Gy/s steady state in graphene LCTEM). While the continuous irradiation in LCTEM provides much higher average power than in pulsed systems, the products formed in pulse radiolysis are likely still formed in LCTEM at short time scales. Accordingly, pulse radiolysis may provide a route to direct chemical identification of key reactive intermediates in graphene liquid cell encapsulation solutions.

$FeCl_3$ is frequently introduced as the etchant for LCTEM etching experiments.[76,77,79–81] Previous reports hypothesized that Fe^{3+} is reduced by solvated electrons to Fe^{2+}, which then catalytically produces sufficient hydroxyl radicals through a Fenton's type mechanism to etch gold.[77] While this mechanism is certainly one of the many simultaneously occurring reactions in a greater reaction network, the feasibility of this mechanism in LCTEM has not been investigated. An alternate possibility that, to date, has not been considered is that the preloaded Fe^{3+} complex is oxidized to a highly reactive species with sufficient potential to etch gold directly. Under the highly oxidizing conditions in LCTEM, it seems plausible that added metal complexes could be oxidized through a ligand or the metal center itself.

In this work, we aim to unravel the role of halides and iron during oxidative etching of gold nanocrystals in graphene LCTEM. We achieve this by combining *in situ* microscopic studies using graphene LCTEM with *in situ* spectroscopic studies using pulse radiolysis, combined with radical reaction network models and quantum chemical calculations of possible key intermediate species. In this manner, we can elucidate the roles of certain additives to nanocrystal transformations in graphene LCTEM, while pulse radiolysis can provide insight into the identity of the species causing these transformations. We designed a series of graphene LCTEM experiments to track the etch rate of gold nanocrystals in the presence of chloride, bromide, and iodide to elucidate their effect on etch rate. The increase in etch rate as we add heavier halides indicates that the predominating role of halides in graphene LCTEM is to act as complexation agents rather than as the active oxidant. The lack of etching in all halide environments in the absence of $FeCl_3$ indicates that iron is significant in the mechanism of gold nanocrystal etching. Accordingly, pulse radiolysis measurements were performed on graphene liquid cell solutions with and without $FeCl_3$ to gain a better sense of iron's role in the AuNC etching mechanism. The observed ground-state bleaching of the Fe^{3+} absorption band suggests that the Fe^{3+} complex may be oxidized by radiolyti-

cally produced radicals. Complete active space self-consistent field (CASSCF) calculations suggest that an oxidized iron complex with a OH ligand is likely the reactive form of iron in solution. Finally, we suggest a mechanism consistent with this data, where the radiolytically produced oxidized iron complex oxidizes the gold nanocrystal, while the halides control the rate of removal of the gold atoms.

2.2 Results & Discussion

Role of halides

For the LCTEM studies, gold nanocrystals were specifically synthesized to contain minimal additives that affect the observed etch rate. The gold nanocrystals were synthesized in the absence of silver, and chloride-containing CTAC ligands were used rather than bromide-containing CTAB, so that the concentration of bromide added to the encapsulating solution could be controlled. A concentrated solution of these pre-made spherical AuNCs were added to a solution of $FeCl_3$ and HCl to create the encapsulating solution. Forty mM $FeCl_3$ was added as the etchant precursor, while HCl was used to prevent hydrolysis of $FeCl_3$ and also tune the final Cl^- concentration to 190 mM. Enough HBr or HI was added to the respective solutions to bring the final concentration of Br^- or I^- to 0.38 mM. The amount of HX (where X = Br, I) added was low enough that the effect on pH was negligible. The exact role of $FeCl_3$ in graphene LCTEM is, to date, unknown, but a hypothesis is presented later in this report. $FeCl_3$ can etch gold in ambient conditions,[74] yet the rate of this was slow and the amount added in these experiments was low enough that minimal etching took place before the *in situ* experiments began. When TEM was used, the beam was spread so that the electron flux imparted on the sample was very low (<25 $e^-Å^{-2}s^{-1}$). When a candidate particle was found, the beam was condensed using a custom-written script to a specified electron flux.[115] At this high electron flux, the combination of radiolysis species and $FeCl_3$ created a highly oxidizing environment in the liquid cell, where AuNC etching could be observed in real time.

Figure 2.2a shows a representative etching trajectory of a gold nanocrystal in a chloride environment without iron, while Figure 2.2b shows the calculated projected area versus time curve of the etching trajectory. This lack of etching was observed in all three halide environments without the presence of iron (see Movies B.1.4-B.1.6). Parts c, e, and g of Figure 2.2 show representative etching trajectories of gold nanocrystals in chloride, chloride and trace bromide, or chloride and trace iodide environments, respectively, all with $FeCl_3$ present. The calculated projected area versus time curves of the etching trajectories of the gold nanocrystals in chloride, bromide, and iodide environments are shown in parts d, f, and h of Figure 2.2, respectively. This metric was chosen as it is consistent across all experimental conditions, including the nanocrystals in trace bromide and iodide environments that change shape throughout their etching trajectory. Gold nanocrystal etching with $FeCl_3$ has been shown to be linear after an initial induction period when plotted as surface area vs. time.[77] In

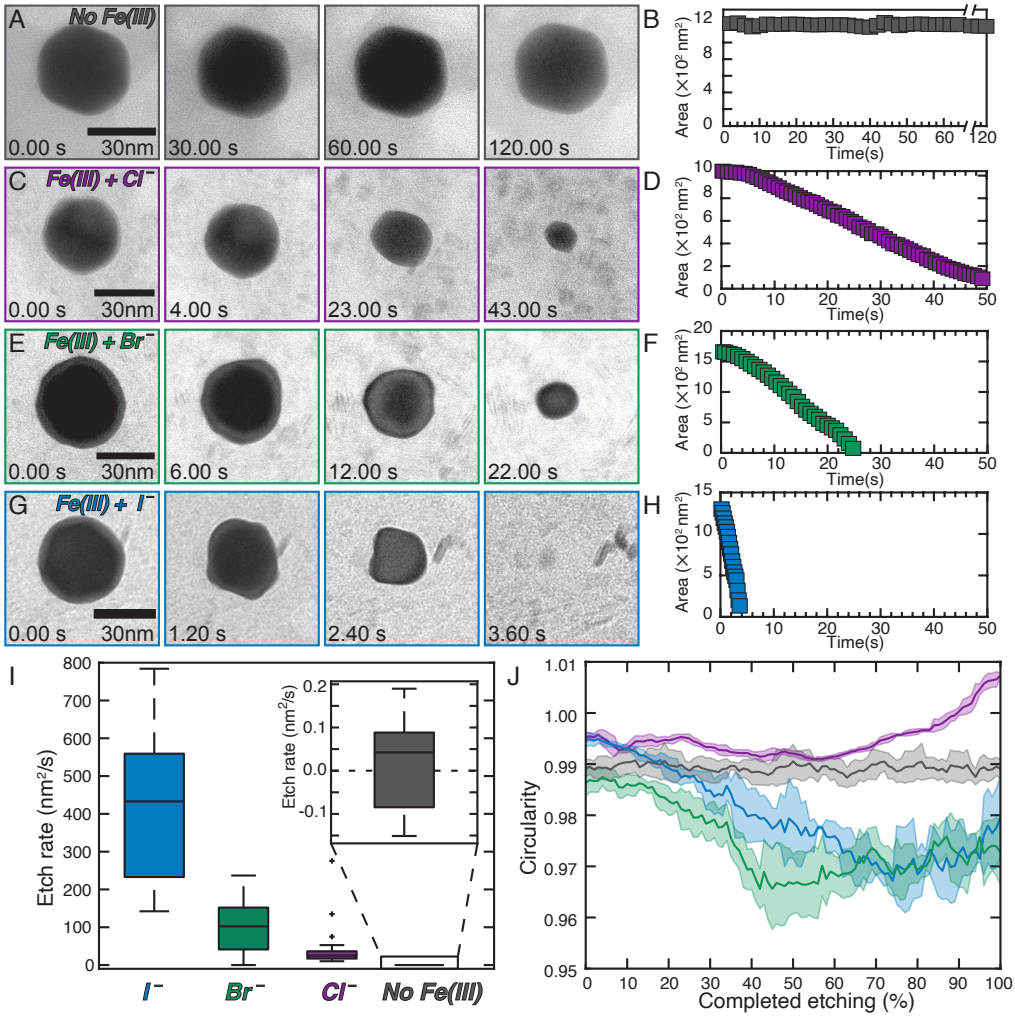

Figure 2.2: Effect of halides on oxidative etching of AuNCs. Etching trajectory and corresponding projected area versus time curves for AuNCs in an aqueous encapsulating solution of 190 mM Cl^- (A, B), 40 mM Fe^{3+} and 190 mM Cl^- (C, D), 40 mM Fe^{3+}, 190 mM Cl^-, and 0.38 mM Br^- (E, F), and 40 mM Fe^{3+}, 190 mM Cl^-, and 0.38 mM I^- (G, H). (I) Box and whisker plot of the average AuNC etch rate in each condition, totaling ca. 80 individual etching trajectories. Etch rates were determined by the slope of the linear portion of the area versus time curves as shown in panels B, D, F, and H. The average is given by the line in the box, the interquartile range is given by the edges of the box, and the range of the rates is given by the whiskers. Outliers are marked with a cross. (J) Circularity of the AuNC as it undergoes oxidative etching. A perfect circle has a circularity of C = 1, while any deviations lead to C < 1. The AuNC in solution with 190 mM Cl^- and 40 mM Fe^{3+} (purple) maintains a constant circularity of $\sim C = 1$, while the AuNCs in solution with 190 mM Cl^-, 0.38 mM Br^-, and 40 mM Fe^{3+} (green) and with 190 mM Cl^-, 0.38 mM I^-, and 40 mM Fe^{3+} (blue) deviate from C = 1 and are constantly changing throughout etching.

this study, they rationalize the linear surface area vs. time curve by suggesting a mechanism which is dependent on both the gold surface and the oxidant. For a sphere, surface area and projected area only differ by a factor of 4, indicating that for the nanocrystals in chloride environment the etch rate is linear with surface area, as seen in previous studies. While only the nanocrystals in chloride remain spherical throughout the etching trajectory, meaning only their projected areas are proportional to surface area, we expect the mechanisms to be similar under all halide environments, as discussed later in this Chapter.

Clearly, the etching time scale depends heavily on the species present in the graphene liquid cell. Without any iron added, the nanocrystals do not etch measurably under the time scales studied. With Fe^{3+} added to the liquid cells, complete etching occurs in the case of all three halides (see Movies B.1.4-B.1.6). The rate of gold nanocrystal etching is modulated by the addition of different halides. The gold nanocrystals etch the fastest in the presence of iodide and the slowest in the presence of chloride. Figure 2.2i summarizes the etching rate of ~ 80 nanocrystals, as box and whisker plots, for each of the environments explored. From this plot, it is apparent that the etch rate increases going down group 17. This trend is consistent with halides acting as complexation agents for the gold ions rather than as active oxidants.

These results indicate that the halide-dependent radical chemistry present in graphene LCTEM does not dominate the observed chemical transformations. Water-based and halide-based radicals are certainly formed once the liquid cell is exposed to the electron beam, but these radicals do not seem to drive the observed reaction trend. There are likely fewer radicals present in graphene liquid cells than is estimated through kinetic modeling, as graphene is known to scavenge radicals and create a milder environment.[60] This could decrease the concentration of halide radicals in the system, releasing halides to complex with gold ions. This effect makes graphene LCTEM well suited to study halide-dependent oxidative etching of metal nanocrystals for improved shape control in nanocrystal synthesis. Halides are well known to act as shape-directing agents in metal nanocrystal synthesis, and, in many cases, these syntheses explicitly employ cycles of oxidative etching and regrowth to improve monodispersity and refine morphology.[108,116–119] The liquid cell studies employed here offer major new dimensions to such studies because they allow for the tracking of individual particles, the comparison of etch rates, and the distribution of rates of etching, as well as the close observation of shape changes in ways that are challenging, if not unachievable, in bulk synthesis. Ultimately, this allows traditional chemical concepts to be studied at a single-particle level with graphene LCTEM.

It is also evident that the interquartile range (*i.e.*, the spread) of the etch rates in Figure 2.2i becomes larger in the case of large rates. As the size and size distribution of the nanocrystals are comparable under all conditions (see Figure A.1.1), we do not expect this to have a major effect on the distribution of etch rates. One possible explanation for this effect is that, as the etch rate increases, the exact rate becomes much more sensitive to the liquid cell geometry. For instance, if one liquid pocket is much thinner than another, this could cause a decrease in etch rate due to a lower concentration of oxidizing species near the surface of the AuNC. It is well known that graphene liquid cell pockets have inhomogeneous

thickness, especially near the edge of the liquid domain.[27,28,36] While this same pocket-size variability is likely present in all conditions studied here, a slower etch rate could allow more time for diffusion, potentially making it less sensitive to these differences.

Notably, the intermediate shapes of the nanocrystals as they undergo oxidative etching appear to become more anisotropic as heavier halides are added. Qualitatively, the AuNCs in solution with Cl^- maintain their spherical shape throughout etching, while the AuNCs in solution with Br^- and I^- become much more anisotropic. To quantify this, the circularity of the particle was calculated in each frame of the video. Circularity is defined in this work according to Equation 2.1,

$$C = \frac{4\pi A}{P^2} \tag{2.1}$$

where A is the projected area of the nanocrystal and P is the perimeter of the NC. If the shape measured is a perfect circle, then the circularity is $C = 1$, while any deviations from a perfect circle give $C < 1$. It is important to note that circularity is very sensitive to the perimeter of the shape being measured. This means that if there are errors during segmentation (binarization, how the outline of the AuNC is automatically determined), the calculated circularity can be misleading. Figure A.1.2 shows a representative outlining for the etching trajectory snapshots of the studied environments. The segmentation code used for this analysis produces a smooth perimeter very near the actual edge of the nanocrystal. Additionally, only the largest boundary in each frame is selected to calculate the circularity. This removes any interference from high contrast precipitates that may form throughout the etching trajectory, as can be seen in the final frames of Figure A.1.2.

Figure 2.2j demonstrates that the nanocrystals in solution with Cl^- maintain a constant circularity throughout the etching trajectory. In the case of added Br^- and I^-, the circularity begins near 1 but quickly decreases. Possible explanations for the decreased circularity when moving to heavier halides are two-fold. On one hand, bromide and iodide are well known to have a strong affinity for certain gold facets,[120] while chloride does not. This affinity directs etching to certain facets,[100] decreasing the circularity of the gold nanocrystals. On the other hand, as the complexation energy increases when heavier halides are added, the overpotential for oxidative etching of gold also increases. The system with iodide present has a > 600 mV increase in overpotential compared to the system with just chloride. This increase likely moves the oxidative etching well into the diffusion-limited regime, causing the oxidation to become anisotropic due to localized differences in the oxidative environment.

It is surprising that small concentrations of bromide and iodide can induce a significant increase in etch rate throughout the entire trajectory. If the AuNCs are oxidized to the Au^{1+} oxidation state, then two halides are needed to complex every gold atom. A gold nanocrystal 20 nm in diameter contains $\sim 2 \times 10^6$ gold atoms, meaning that 4×10^6 halides need to be present in each liquid cell pocket to complex all the gold atoms. As the thicknesses of the graphene liquid cells are typically < 200 nm,[18,35] the lateral dimension of the liquid cell needed to contain stoichiometric concentrations of bromide and iodide is on the order of 20 μm, far larger than the size of typical liquid cell pockets.[34,35] An excess of chloride is present

in all of the experiments, but if the complexation were to switch from a heavier halide to chloride in the middle of an etching trajectory, we would expect to see a distinct decrease in the etch rate due to the increasing reduction potential. This would manifest itself in the projected area versus time curves as a decrease in the etch rate as the etching trajectory progresses or as a second linear portion of the graph with a smaller slope, which is not present in these etching trajectories.

To rationalize this, we must consider ways in which the trace halides may be recycled. This may indicate the presence of chemical loops inside the liquid cell pockets. In this manner, a single chemical species is repeatedly oxidized and reduced many times by radicals or other species present in the system. For instance, two halides from solution complex an oxidized gold atom to form a $[AuX_2]^-$ complex. This complex could then be reduced by a solvated electron or hydrogen atom to form a Au^0 atom and two free X^- ions. These same halides are now available to complex another gold atom. This process constantly refreshes the supply of precursors to the system. In this case, even though there is a substoichiometric concentration of bromide or iodide added to the system, the concentration of the heavy halide ion available to the system approaches a steady state, which would give rise to the constant etch rates observed in this study.

Role of iron

In initial AuNC etching studies, iron in the form of $FeCl_3$ was empirically determined to be a suitable beam-initiated etchant precursor. However, the mechanism of etching remains unclear. Iron was previously proposed to be a catalyst to produce $^{\bullet}OH$ radicals through Fenton's mechanism,[77] as shown in Equation 2.2.

$$Fe^{2+} + H_2O_2 \longrightarrow Fe^{3+} + {}^{\bullet}OH + {}^{-}OH \tag{2.2}$$

In the graphene liquid cell, Fenton's reaction would occur as follows. Preloaded Fe^{3+} from $FeCl_3$ would be reduced by the electron beam to Fe^{2+}. Fe^{2+} would then react with radiolytically produced H_2O_2 to catalytically produce $^{\bullet}OH$. Through this mechanism, the presence of iron would need to cause a significant increase in the concentration of $^{\bullet}OH$ to account for the significantly accelerated etch rate of AuNCs. Additionally, any hydroxyl radicals produced through this mechanism are likely to be scavenged by the halides, as discussed previously. Therefore, any additional hydroxyl radicals produced through Fenton's reaction would ultimately manifest as a greater concentration of the $X_2^{\bullet-}$ species, where X = Cl, Br, and I. When Fenton's reaction is added to our kinetic model, we see no significant change in the concentration of hydroxyl radicals in the presence of halides and even a slight decrease in $^{\bullet}OH$ concentration compared to when no iron is present (see Figure A.1.3). We have shown earlier that the gold nanocrystal etch rate increases with the presence of halides, moving down group 17. If the $X_2^{\bullet-}$ radicals were the active etchants in this system, the gold nanocrystal etch rate should decrease, even if the halides are acting as both complexation agents and oxidants (see Figure A.1.4). While Fenton's reaction is likely occurring to some

extent in the liquid cell solution, it seems unlikely that this reaction accounts for the observed reactivity. It is well known that, under the high electron fluxes used in this study, both highly reducing and oxidizing species are formed.[48] Under these conditions, it is possible that the preloaded Fe^{3+} is oxidized by radicals to some extent, and it is this oxidized iron complex that directly oxidizes the AuNC.

Pulse radiolysis was used to gain spectroscopic insight into the role of iron in graphene LCTEM experiments. Pulse radiolysis is a pump-probe technique that allows spectroscopic observation of the formation of short-lived radicals under electron radiation with nanosecond time resolution. Additionally, by using selective radical scavengers, it is possible to investigate the oxidative and reductive reaction pathways separately. In these experiments the solution of interest is placed into a flow cell system ensuring the desired gas saturation of the solution as well as allowing for a renewal of the sample solution in the sample cell for every electron pulse. The sample is irradiated with an electron pulse with a peak electron flux of $\sim 4.25 \times 10^9$ Gy/s (85 Gy/pulse and a 15 ns pulse width), comparable to the steady-state electron fluxes used in graphene LCTEM. Using a fast-transient recorder, the absorption and decay of transient radical species can be observed within a 1 ms time domain. Herein, Δ OD is defined as the difference in optical density before (OD(GS), ground state absorption) and after (OD(T), transient) the electron pulse, as shown in Equation 2.3.

$$\Delta OD = OD(T) - OD(GS) \tag{2.3}$$

Figure 2.3 a and c depict the pulse radiolysis transient absorption spectra of an aqueous 0.2 M HCl solution and an aqueous 0.2 M HCl solution containing 1 mM $FeCl_3$, respectively, both saturated with N_2O. Such conditions lead to the production of three highly reactive species, namely, $^{\bullet}H$, $^{\bullet}OH$, and e^-_{aq}, in addition to the molecular products H_2 and H_2O_2. Under our experimental conditions, N_2O is used to efficiently scavenge and convert e^-_{aq} into $^{\bullet}OH$. The $^{\bullet}OH$ radicals react with Cl^- and ultimately form $Cl_2^{\bullet-}$ (see Table 2.1 for the detailed reaction cascade), which is discernible by the well-established transient absorption spectrum with a maximum at 340 nm.[121] This peak is observed in pulse radiolysis transient absorption spectra both with and without $FeCl_3$ (Figure 2.3a and c). A first indication toward a potential reaction of $Cl_2^{\bullet-}$ with Fe^{3+} comes from the comparison of the transient spectra in the 100 μs range. When $FeCl_3$ is present, the decay of the $Cl_2^{\bullet-}$ transient absorption goes below zero in the UV part of the optical spectrum around 290-360 nm, where Fe^{3+} complexes show strong ground-state absorption (see Figure A.1.5). This ground-state bleaching indicates that less Fe^{3+} is present at this time than before the electron pulse, suggesting a potential reaction between Fe^{3+} and $Cl_2^{\bullet-}$.

In addition to the reaction of Fe^{3+} with $Cl_2^{\bullet-}$, the reaction of Fe^{3+} with $SO_4^{\bullet-}$– another strongly oxidizing intermediate with an oxidation potential of +2.4 V vs. NHE[122]– was probed. The $SO_4^{\bullet-}$ radical is formed in a nitrogen saturated aqueous solution containing $K_2S_2O_8$ and 5 vol% t-BuOH. The radiolysis of such solutions initially forms the products of the water radiolysis ($^{\bullet}OH$, $^{\bullet}H$ and e^-_{aq}). The t-BuOH efficiently scavenges the $^{\bullet}OH$ and $^{\bullet}H$ radicals. The solvated electron reacts with $S_2O_8^{2-}$ to form SO_4^{2-} and $SO_4^{\bullet-}$. The latter is

discernable by its characteristic transient absorption spectrum with a maximum around 450 nm (see Figure A.1.6a).[123] When Fe^{3+} is added to this the solution, initially the transient absorption spectrum of $SO_4^{\bullet-}$is observed, but with increasing delay time a negative transient absorption develops in the spectral region below 350 nm (see Figure A.1.6c), where Fe^{3+} shows absorptions, similar to the reaction of Fe^{3+} with $Cl_2^{\bullet-}$. This is indicative of a reaction of Fe^{3+} with $SO_4^{\bullet-}$ (compare Figures A.1.6b and A.1.6d). This indicates that Fe^{3+} may in general react with very strong oxidizing intermediates.

Table 2.1: Proposed Reaction Cascade in Pulse Radiolysis Experiments

Label	$H_2O \rightsquigarrow e_{aq}^- + {}^\bullet H + {}^\bullet OH$	Reference
a	$N_2O + e_{aq}^- + H_2O \longrightarrow N_2 + {}^\bullet OH + OH^-$	Buxton[124]
b	${}^\bullet OH + H^+ + Cl^- \longrightarrow Cl^\bullet + H_2O$	Buxton[124]
c	$Cl^\bullet + Cl^- \longrightarrow Cl_2^{\bullet-}$	Jayson et al.[112]
d	$2\,Cl_2^{\bullet-} \longrightarrow 2\,Cl^- + Cl_2$	Jayson et al.[112]
e	$2\,Cl_2^{\bullet-} [Fe^{3+}L]^{x+} \longrightarrow 2\,Cl^- + [Fe^{ox}L]^{(x+1)+}$	
f	$2\,Cl_2^{\bullet-} [Fe^{3+}L]^{x+} \longrightarrow 2\,Cl^- + [Fe^{3+}L^{ox}]^{(x+1)+}$	

Further, the $Cl_2^{\bullet-}$ decay, as depicted by the 340 nm time absorption profile in parts b and d of Figure 2.3, can be evaluated to determine the kinetics of the reaction. Without any other potential reaction partners, $Cl_2^{\bullet-}$ recombines in disproportionation reaction (Table 2.1d). As expected for such a bimolecular recombination reaction when plotting $1/\Delta OD$ versus time for the 340 nm time profile (Figure 2.3b, inset) in the systems without $FeCl_3$, the resulting graph can be fitted linearly, and from the slope a bimolecular recombination rate constant of $2k = 2.7 \times 10^9 M^{-1}s^{-1}$ was derived as the recombination rate constant for $Cl_2^{\bullet-}$ under our reaction conditions. Plotting $1/\Delta OD$ versus time for the time profile of $Cl_2^{\bullet-}$ decay in the presence of $FeCl_3$ (Figure 2.3d, inset) shows a significant deviation from a linear relation, indicating a more complex reaction other than only the recombination of $Cl_2^{\bullet-}$. If there was no reaction between $Cl_2^{\bullet-}$ and Fe^{3+}, we would expect to see the same linear $1/\Delta OD$ versus time plot as in the inset of Figure 2.3b, as the only reaction pathway for the $Cl_2^{\bullet-}$ radicals would be their recombination. In the case of added $FeCl_3$, the $1/\Delta OD$ versus time plot is not linear, suggesting an additional reaction pathway for $Cl_2^{\bullet-}$. As the only additional species in solution is Fe^{3+} ions, this suggests a reaction between $Cl_2^{\bullet-}$ and Fe^{3+}. This further supports our hypothesis that the $Cl_2^{\bullet-}$ radical is reacting with Fe^{3+}. Unfortunately, even if evidence for a reaction of $Cl_2^{\bullet-}$ with Fe^{3+} were obtained, the reaction of $Cl_2^{\bullet-}$ with Fe^{3+} is a minor channel, and we have not been successful in obtaining a reliable rate constant for this reaction.

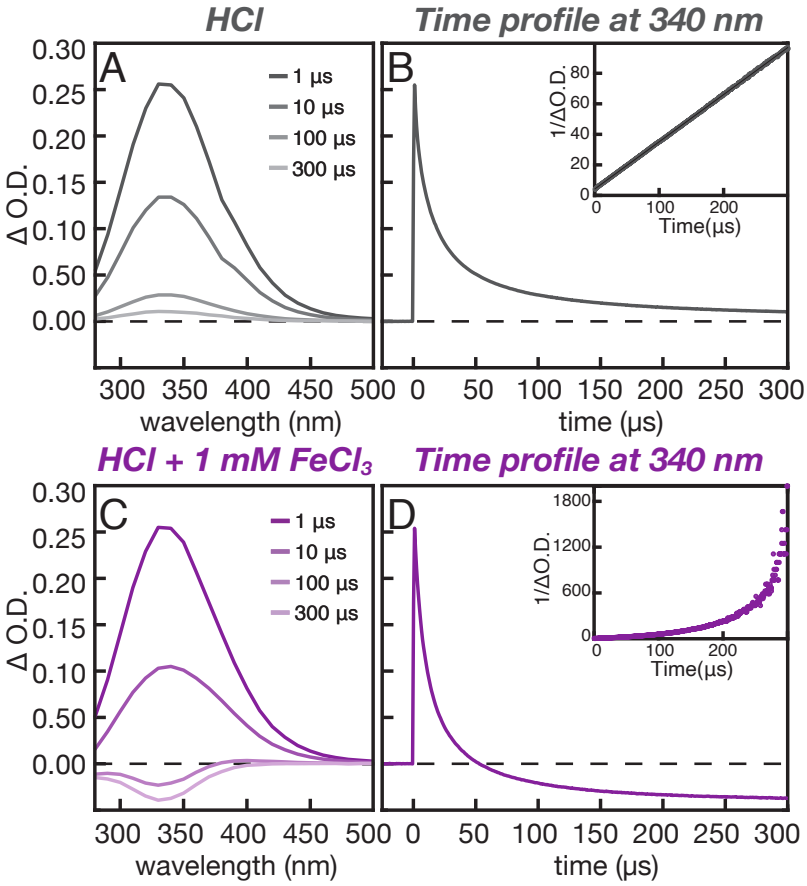

Figure 2.3: Pulse radiolysis measurement (85 Gy/pulse, 15 ns fwhm) of a 0.2 M HCl solution (A, B) and a 0.2 M HCl and 1 mM $FeCl_3$ solution (C, D) in N_2O saturated water. (A) Transient absorption spectra of a 0.2 M HCl solution at four different times: 1, 10, 100, and 300 μ s. (B) Related time profile of the transient absorption decay at 340 nm. (Inset) Time profile at 340 nm plotted as 1/OD versus time. The black line depicts a linear fit. (C) Transient absorption spectra of a 0.2 M HCl and 1 mM $FeCl_3$ solution at four different times: 1, 10, 100, and 300 μ s. (D) Related time profile of the transient absorption decay at 340 nm. (Inset) Time profile at 340 nm plotted as 1/OD versus time. Note that the OD values in the inset have been shifted by +0.0378 to prevent disruption of the shape of the curve due to the pole of the 1/x function for $x = 0$. This shift causes the 1/OD values to be larger at long times compared to the inset in (B).

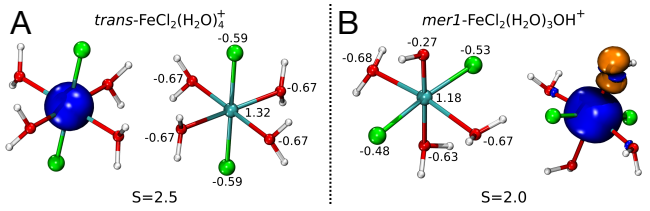

Figure 2.4: Mulliken partial charges and spin density isosurfaces from CASSCF calculations of a) trans$-FeCl_2(H_2O)^{4+}$ and b) mer$_1-FeCl_2(H_2O)_3OH^+$. See the Supporting Information for information on the active space. The blue isosurface highlights regions with increased alpha spin density, while orange highlights regions of increased beta spin density.

To consider how a reaction between Fe^{3+} and $Cl_2^{\bullet-}$ might be possible, we consider two pathways for the oxidation. $Cl_2^{\bullet-}$ can react with Fe^{3+} to oxidize the iron center ($[Fe^{ox}L]^{x+}$) or the ligands ($[Fe^{3+}L(ox)]^{x+}$). To explore the oxidation of the ligands, we first consider the ligand shell present on the iron ion. At the chloride concentration used in these studies, likely 1-2 Cl-ligands are present in the Fe^{3+}-aqua complex.[125] All possible isomers with 1-2 Cl-ligands were investigated through DFT calculations to determine the most stable structure. For each isomer, we have included seven possible electronic structures in our study. Four of the seven electronic structures started with default values for multiplicities of 1, 3, 5, 7 resulting mainly in electronic structures with increased α spin density on all atoms. The electronic structure of multiplicities 3, 5 and 7 served subsequently as initial input for antiferromagnetic structures with multiplicity of 1, 3 and 5, respectively. In these cases, the spin density on the iron atom was flipped in the initial guess of the wave function. Figure A.1.9, A.1.10, A.1.11 and A.1.12 show all obtained stable electronic structures for each isomer where the energy of the most stable electronic structure of each isomer was set to 0 kJ/mol. A comparison of the stability of the isomers to each other is provided in Figure A.1.13.

Finally, we compared the complexes to each other, see Figure A.1.14. The pK_a-value of the Fe-complexes were determined by following equation:

$$pK_a(Fe) = pK_a(Fe_{ref}) + \frac{G(Fe^-) + G(FeH_{ref}) - G(FeH) - G(Fe^-_{ref})}{2.303 \times RT} \tag{2.4}$$

where $pK_a(Fe_{ref})$ is the experimental pK_a-value of $Fe^3{\equiv}(H_2O)_6^{3+}$. $G(FeH)$ and $G(Fe^-)$ are the calculated Gibbs free energy of the protonated and deprotonated Fe-complex, respectively. $G(FeH_{ref})$ and $G(Fe^-_{ref})$ refers to the Gibbs free energy of $Fe^3{\equiv}(H_2O)_6^{3+}$, protonated and deprotonated. We have chosen $Fe^3{\equiv}(H_2O)_6^{3+}$ as reference due to the similarity to our investigated system which is essential to calculate accurate pK_a-values by isodesmic reactions.[126] Furthermore, we have employed the SMD solvation model[127] for the calculation of pK_a-values and Gibbs free energies between different complexes shown in Figure A.1.14 and A.1.15. The SMD solvation model excels C-PCM in accuracy and provides pK_a-values in so-

lution surpassing approaches based on thermodynamic cycles.[128] These calculations showed that mer$_1$−$FeCl_2(H_2O)_3OH^+$ should be the most stable oxidized complex under the experimental conditions. A similar protocol was applied to the Fe-complex before the oxidation where solely high spin states were considered. Figure A.1.15 shows the comparison of the most stable structures highlighting that [trans−$FeCl_2(H_2O)_4]^+$ is most stable in solution. Finally, CASSCF calculations of the most stable complexes were carried out where the orbitals of the active space are shown in Figure A.1.16.

Under these experimental conditions, the [trans−$FeCl_2(H_2O)_4]^+$ structure (Figure 2.4a) was found to be the most stable in solution. Upon oxidation, the trans−$[FeCl_2(H_2O)_4]^+$ complex lost a H atom to become mer$_1$−$[FeCl_2(H_2O)_3OH^+]$. CASSCF (14,10) calculations were used subsequently to determine the electronic structure of the oxidized complex. Figure 2.4b shows the isosurface of the spin density indicating that the OH ligand plays an important role in the electronic structure of the complex. This is supported by a local spin analysis revealing a complex that resembles a high-spin Fe^{4+} complex ($< SZ >= 2.14$) antiferromagneticly coupled to the OH ligand ($< SZ >= -0.14$). Additionally, comparison of the Mulliken partial charge of mer$_1$−$[FeCl_2(H_2O)_3OH^+]$ to trans−$[FeCl_2(H_2O)_4]^+$ indicates that it is mainly the O atom of the OH ligand that is oxidized, while the electron density around the iron center is slightly increased. This suggests that the role of iron in the LCTEM experiments may be to stabilize the reactive radical species by complexing to the iron center. Considering the pulse radiolysis data, it seems plausible that the $Cl_2^{\bullet-}$ radical oxidizes the Fe^{3+} complex in solution to decay into its products. The oxidized iron complex then stabilizes itself by donating a hydrogen atom to form mer$_1$−$[FeCl_2(H_2O)_3OH^+]$, supported by the high acidity of the unprotonated complex. Then the oxidized hydroxyl ligand bound to the iron center is the reactive species that oxidizes the gold nanocrystals.

The pulse radiolysis experiments suggest that the active iron species in our solution have extended lifetimes compared to radiolytically produced radical species. If the active iron species is long-lived, it may be possible to build up a concentration during electron-beam irradiation that, upon removal of the electron beam, would continue to etch the gold nanocrystal. Figure 2.5a shows an etching trajectory of a gold nanocrystal in the same chloride solution as in Figure 2.2a. A plot of the initial projected area versus etch rate for these nanocrystals is shown in Figure A.1.7. Halfway through the etching trajectory, the dose was decreased from 800 to 25 $e^-Å^{-2}s^{-1}$. The nanocrystal continued etching after removal of the high-intensity beam, but at a slower etch rate (see Movie B.1.7). This is in contrast to constant irradiation at 25 $e^-Å^{-2}s^{-1}$ without the initial high dose period, which leads to negligible etching (Figure 2.5b). We confirmed that the nanocrystals were in liquid rather than in a dry pocket (see Figure A.1.8) in these control experiments. Figure 2.5c shows a representative projected area versus time curve for the nanocrystals originally irradiated at a high electron flux. Etching of the nanocrystals continues after the dose is decreased, albeit at a much slower rate. This indicates that a concentration of a long-lived oxidant is built up during the high-dose-rate regime. Then, once the electron flux is decreased, the excess oxidant in solution can diffuse to the surface of the nanocrystal and continue oxidatively etching the gold. Figure 2.5d shows this data for several different

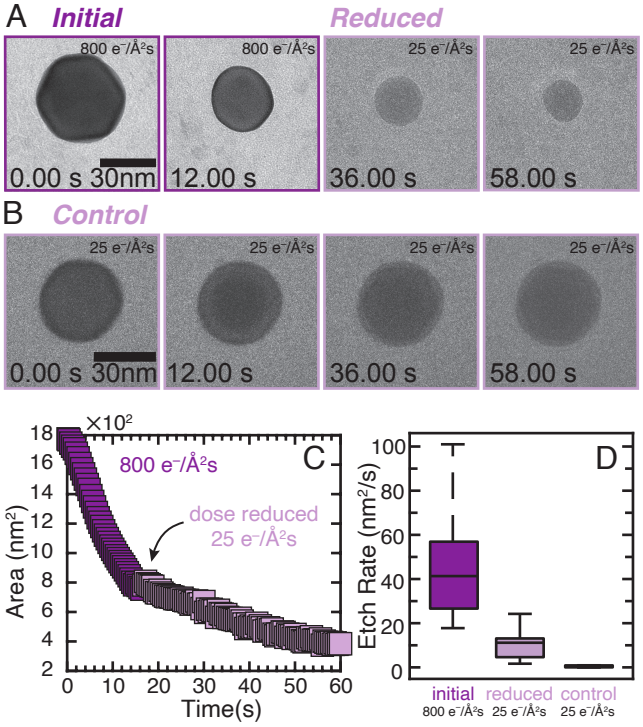

Figure 2.5: a) Etching trajectory of a AuNC in 40 mM Fe^{3+} and 190 mM Cl^-. The etching trajectories begin at 800 $e^-Å^{-2}s^{-1}$ but are reduced to 25 $e^-Å^{-2}s^{-1}$ in the middle of etching. After the electron flux decrease, the nanocrystal continues etching. b) Control experiment showing that when the AuNC is initially irradiated at 25 $e^-Å^{-2}s^{-1}$ the nanocrystal does not etch. c) Area versus time curve of the etching trajectory shown in a). The nanocrystal etches at a constant rate initially, consistent with the previous experiments. When the electron flux is decreased, the etch rate immediately slows, but etching continues. d) Box and whisker plots summarizing 19 different etching trajectories recorded under these conditions. The average etch rate of the AuNC after reducing the electron flux is significantly lower than the initial etch rate, but it is nonzero.

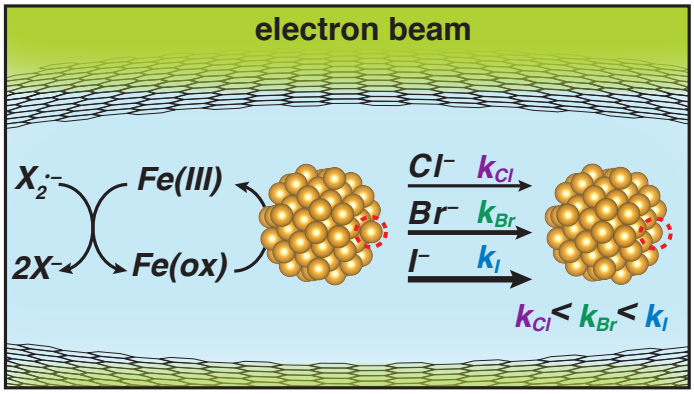

Figure 2.6: Proposed mechanism of AuNC etching in graphene LCTEM.

etching trajectories, presenting the reproducibility of this trend.

The lifetime of the $Cl_2^{\bullet-}$ radical in this system is on the order of a few hundred microseconds (Figure 2.3b), while water-based radicals have much shorter lifetimes. On the basis of this, any radicals formed while the liquid cell was irradiated with a high electron flux should decay $<$ 1 ms after the dose is decreased. The prolonged etching after the electron flux is decreased indicates it is unlikely that a water- or halide-based radical is responsible for gold nanocrystal etching. This experiment supports the pulse radiolysis data indicating the formation of a long-lived transient species that is directly involved in the gold nanocrystal etching.

Taking into account the role of the halides and the role of the iron species in graphene LCTEM, we propose a mechanism consistent with the data, as shown in Figure 2.6. First, radiolysis induced by the electron beam creates a significant concentration of oxidizing radicals. These radicals react with the preloaded Fe^{3+} to form an oxidized iron transient species. The oxidized iron transient species then oxidizes the gold nanocrystal. However, the rate at which the gold nanocrystal is oxidized is controlled by the type of halide present. The standard reduction potential for gold decreases in the presence of heavier halides, effectively increasing the overpotential and increasing the rate of oxidation.

2.3 Conclusion

Understanding the chemical processes occurring in LCTEM is crucial to determine the mechanism of nanocrystal etching. We have shown that introducing trace amounts of halides can significantly modulate the etch rate of gold nanocrystals under electron-beam irradiation. While the halides are also known to create oxidizing radical species, in this system their dominating role is as a complexation agent for the oxidized gold ions. This indicates that metal nanocrystal etching studies performed in graphene LCTEM can be relevant for study-

ing the effect of shape control by halides, particularly syntheses that use oxidative etching. In the present case, the liquid cell studies in tandem with pulse radiolysis and computational quantum chemistry have offered several new insights. The role of halides as complexation agents in particular should help in the more systematic design of future bulk syntheses. However, it is possible that the halide radicals may play a much bigger role when studying less-stable systems, such as semiconducting or metal oxide nanocrystals, or when imaging in a SiN_x liquid cell because any radical-scavenging effect from the graphene is absent. It is important to consider the effect of halides, even in minute quantities, as low concentrations in solution can cause significant effects under electron-beam irradiation.

A distinct lack of etching of gold nanocrystals in the absence of preloaded $FeCl_3$ indicates that iron plays a significant role in the etching mechanism. A combination of LCTEM experiments, pulse radiolysis experiments, and theoretical calculations suggests that the added Fe^{3+} species are oxidized by radicals into a highly reactive, yet long-lived, oxidized complex. This complex is responsible for the etching of gold nanocrystals in LCTEM, contrary to previous reports proposing $^{\bullet}OH$ radicals as the active oxidant. Further, it is possible that this behavior is not limited to iron salts and indicates that care must be taken to consider the reactivity of metal ions that may be present in the solution or in the material of interest during liquid cell observation. This study points to the importance of understanding the additives in the encapsulating solution. Ultimately, this is a step toward defining the chemical environment within graphene LCTEM to aid in better control and interpretation of LCTEM experiments.

2.4 Materials and Methods

Nanocrystal Synthesis

Gold nanocrystals were synthesized following a modified procedure published previously.[96]

Preparation of Seeds

Briefly, 10 mL of 100 mM cetyltrimethylammonium chloride (CTAC) and 0.25 mL of 10 mM hydrochloroauric acid ($HAuCl_4$) were added to a clean, 20 mL vial. The vial was put into a water bath set to 30 °C and was stirred rapidly. $NaBH_4$ (0.45 mL, 20 mM) was added, allowed to stir for 1 min, and then left undisturbed at 30 °C for 1.5 h to decompose any excess $NaBH_4$.

Preparation of Nanocrystals

Two identical solutions of 9.5 mL of 100 mM CTAC, 0.25 mL of 10 mM $HAuCl_4$, and 90 μL of 40 mM ascorbic acid (AA) were each added to clean 20 mL vials in order. To the first vial, 25 μL of the seed solution was added during rapid stirring until the solution turned

pale pink (∼5 s). Then, 300 μL of this solution was added into the other vial, briefly mixed, and left to sit on the bench for 15 min to allow the growth to complete. The solution was then washed and resuspended in water three times by centrifugation at 8000 rpm for 10 min. After the final washing, the nanocrystals were concentrated to an optical density (OD) of 1 and then stored in a vial in the dark.

Graphene Liquid Cell Preparation

Graphene liquid cells (graphene liquid cells) were prepared as described previously[115] with modifications as follows. Prepared graphene-coated grids were used to encapsulate a solution of 40 mM $FeCl_3$ in 40 mM HCl and the presynthesized gold naoncrystals. For samples with Br^- or I^-, concentrated HBr or HI was serially diluted with Milli-Q water to a 0.8 mM concentration. This solution was added to the $FeCl_3$ and gold nanocrystal solution for a final concentration of 0.38 mM. Approximately 0.5 μL of the encapsulating solution was placed on the graphene side of a graphene coated grid held in self-closing tweezers. A half-grid, prepared by cutting a grid with a razor, was then immediately placed graphene side down on top of the droplet and left to dry for 10 minutes.

In situ TEM Imaging

All experiments were performed on a FEI Tecnai S-Twin T-20 TEM operating at 200 kV with a LaB_6 filament. *In situ* videos were collected with a Gatan Rio 16 IS camera using the Digital Micrograph *in situ* data collection function. Videos were binned by two for 2048 × 2048 resolution. The nominal magnification was 97k× for a pixel resolution of 1.4 Å/pixel. The frame rate for most videos was 5 fps, yielding a temporal resolution of 0.2 s. The frame rate of videos containing iodide and no iron was 2 fps, yielding a temporal resolution of 0.5 s. To convert CCD counts to electrons, a conversion value of 124 was used and all videos were taken at 800 $e^-Å^{-2}s^{-1}$, except for the graphene liquid cells without iron, which were taken at 2000 $e^-Å^{-2}s^{-1}$. It is important to note that there may be a slight inaccuracy in this conversion value, but as all videos were taken at the same electron flux, the conclusions of this Article are independent of its exact value. Additionally, this conversion value is different from that in previous publications from our group[77] because we have updated our camera system. So far, we have been unable to determine a conversion value from our previous camera to this one, so exact electron fluxs published in this and future works may be slightly different from those in previous publications.

Pulse Radiolysis

The pulse radiolysis experiments were carried out using 15 ns electron pulses from the 10 MeV linear accelerator Elektronika-U003 (Toriy, Moscow). The dose delivered per pulse was measured by electron dosimetry and SCN dosimetry.[129] Doses of ∼85 Gy/pulse were selected. The optical detection system consisted of a pulsed 1000 W xenon lamp (Osram,

XBO1000), Suprasil cell (light path 1 cm), high-intensity grating monochromator (Acton research, SP500), R928 photomultiplier (Hamamatsu Photonics), and a fast transient recorder (Tektronix, TDS5034B). Linac operation and data acquisition were done in the computer-controlled mode.

Theoretical Calculations

All calculations were carried out with the ORCA program package.[130] A revised B3LYP functional was employed for structure optimization, which is optimized to estimate the energy splitting between different spin states.[131,132] The resolution of identity (RI) approximation was used to speed up Coulomb and exchange integrals.[133] All calculations employed the def2-TZVP basis set.[134] Dispersion forces were considered by an atom pairwise dispersion correction with the Becke-Johnson damping scheme,[135,136] while solvation effects of water were incorporated by the conductor-like polarizable continuum model (C-PCM).[137] The structure was confirmed as a minimum on the potential energy surface by a seminumerical frequency calculation. Subsequently, CASSCF calcu- lations were carried out. The final active space consists of 15 electrons in 10 orbitals for the initial complex and 14 electrons in 10 orbitals for the oxidized complex. The natural orbitals of the active space as well as a detailed discussion about how the most stable isomer was identified can be found in the Supporting Information. Local spins were determined by the approach proposed by Herrmann, Reiher, and Hess.[138] All calculations were uploaded to the NOMAD repository with an embargo time of 3 months to support the FAIR data principles.

Chapter 3

EELS studies reveal substantial solute concentration effects in graphene liquid cells

Reproduced in part with permission from: Crook, M. F.; Moreno-Hernandez, I. A.; Ondry, J. C.; Ciston, J.; Bustillo, K. C.; Vargas, A.; Alivisatos, A. P. "EELS Studies of Cerium Electrolyte Reveal Substantial Concentration Effects in Graphene Liquid Cells" *Journal of the American Chemistry Society* **2023**, 145, 12, 6648-6657

Graphene liquid cell transmission electron microscopy is a powerful technique to visualize nanoscale dynamics and transformations at atomic resolution. However, the solution in liquid cells is known to be affected by radiolysis, and the stochastic formation of graphene liquid cells raises questions about the solution chemistry in individual pockets. In this study, electron energy loss spectroscopy (EELS) was used to evaluate a model encapsulated solution, aqueous $CeCl_3$. First, the ratio between the O K-edge and Ce M-edge was used to approximate the concentration of cerium salt in the graphene liquid cell. It was determined that the ratio between oxygen and cerium was orders of magnitude lower than what is expected for a dilute solution, indicating that the encapsulated solution is highly concentrated. To probe how this affects the chemistry within graphene liquid cells, the oxidation of Ce^{3+} was measured using time-resolved parallel EELS. It was determined that Ce^{3+} oxidizes faster under high electron fluxes, but reaches the same steady state Ce^{4+} concentration regardless of flux. The time-resolved concentration profiles enabled direct comparison to radiolysis models, which indicate rate constants and g-values of certain molecular species are substantially different in the highly-concentrated environment. Finally, electron flux-dependent gold nanocrystal etching trajectories showed that gold nanocrystals etch faster at higher electron fluxes, correlating well with the Ce^{3+} oxidation kinetics. Understanding the effects of the highly-concentrated solution in graphene liquid cells will provide new insight on previous studies, and may open up opportunities to systematically study systems in highly-concentrated solutions at high resolution.

3.1 Introduction

Liquid cell transmission electron microscopy (LCTEM) is a technique that allows users to study systems at nanoscale resolution in solution. This technique has uncovered many discoveries such as new mechanisms of growth and etching of nanocrystals,[18,74,76,79,139] nanocrystalline structure in solution,[82,103] and nanocrystal superlattice formation.[26,140–142] This technique will continue to generate active interest because, thus far, it is the only method that enables the direct structural observation of single particle trajectories of nanocrystal chemical transformations. From the beginning, there have been concerns that the observation conditions would not correspond to that of the native colloidal solution. The earliest studies showed that the effective viscosity of the trapped liquids were orders of magnitude higher than typical liquids,[74] in part because the most readily observed nanocrystals are trapped near the surface.[143] Early simulations suggested that there are significant perturbations of the liquid by the electron beam,[48] and that these perturbations significantly alter the reactivity. More recent work has shown that these effects can be modulated using redox couples.[83] This study here suggests that there is an additional major difference with common nanocrystal growth solution conditions, namely the possibility that the fluids in graphene liquid cells are highly concentrated electrolytes.

There has been significant progress over the last decade to understand the solution chemistry in LCTEM. At this point it is well known that many of the observed chemical transformations are controlled by electron beam initiated reactions. The electron beam of the TEM induces radiolysis of water molecules (or other solvents) to form highly reactive species, such as $^{\bullet}OH$, $H^{\bullet}$, H_2O_2, among others,[39–41] which can either interact directly with the sample,[86,144,145] or with added solutes to induce changes in the sample,[77,79,83,84,146] with increasing evidence that these reactive species can be deliberately controlled to explore different kinetic regimes. Yet, as the structures of the solvated species that may drive chemical transformations in the liquid cell are indiscernible with electron microscopy, work to understand the solution chemistry and it's interactions with a sample of interest has relied on models,[48] correlative experiments,[19,84,86] or through probing indirect chemical transformations.[77,78,83]

More recently, advanced TEM techniques such as electron energy loss spectroscopy (EELS) have been used to determine changes in the sample upon irradiation. EELS is a technique in which electrons from the electron beam scatter inelastically within the sample, losing characteristic amounts of energy that correspond to inner shell or valence transitions.[90] Through analysis of the fine structure of the energy loss spectrum of core transitions, information such as oxidation state and chemical environment can be inferred. EELS has been used in conjunction with LCTEM previously to measure the thickness of the liquid,[23,30] or to check for water by confirming the presence of the O K-edge.[23,34,147] If the liquid layer is sufficiently thin, fine structure analysis of core-loss transitions can be performed through the liquid.[148] This has been done previously to explore how irradiation in LCTEM changes the oxidation states of materials,[22,149] and even to measure the water structure in liquid cells.[28,93,150]

In this study, we use core-loss EELS to elucidate the solution chemistry present in

graphene liquid cells. Graphene liquid cells are a particularly interesting liquid cell type, as they are easy to prepare, do not require a specialized holder, and the thin, low-Z graphene windows offer the highest resolution of the liquid cell configurations. With graphene liquid cells, a solution of interest is placed between two graphene coated TEM grids, and the van der Waals forces between the graphene sheets hermetically seal a small volume of the solution and protect it from the vacuum environment of the TEM.[76] While graphene liquid cells have been utilized to study systems at high resolution, the nature of these liquid cells raise questions about the solution chemistry and how it may differ from bulk solutions. It has been suggested that 2D materials such as graphene exert a van der Waals pressure on liquid or gas molecules trapped between layers,[151–153] and this phenomenon has been suggested to occur in graphene liquid cells as well.[36] Additionally, the individual pockets within a graphene liquid cell form stochastically, sometimes around objects like nanocrystals,[27] indicating that the environment could differ from region to region. Finally, since these pockets form through evaporative drying of the solution, the concentration of species within the liquid cell may be different from the original encapsulating solution.

Here, we use EELS to probe the chemistry of a model redox couple, Ce^{3+}/Ce^{4+}, in graphene liquid cells. The Ce^{3+}/Ce^{4+} redox couple was chosen as Ce has a large EELS cross section, there are marked differences between the Ce^{3+} and Ce^{4+} EEL spectra, and previous work has shown that this redox couple has the potential to etch gold nanocrystals in graphene liquid cells.[83] Steady-state EELS results indicated that the solution within graphene liquid cells was substantially more concentrated than the preparation solution across various starting concentrations. As a highly concentrated solution likely alters the kinetics of the system, we next studied the oxidation kinetics of Ce^{3+} with time-resolved EELS. The rate of oxidation of Ce^{3+} increased with increasing electron flux, but all systems reached a similar steady-state Ce^{4+} concentration regardless of electron flux. It was determined that the kinetics of oxidation could not be explained with prior radiolysis models derived from pulse radiolysis results of dilute solutions. The radiolysis models were revised to account for the observed Ce^{3+} oxidation kinetics, largely through methods developed for highly concentrated solutions. These factors indicate that the graphene liquid cell technique results in a substantial increase in the concentration of solutes, and for the studies conducted herein the solution may be better described as a hydrated salt matrix rather than a dilute liquid solution. Lastly, we studied the electron flux dependent etching of gold nanocrystals, a model system, and correlated the results to the kinetic EELS data.

3.2 Results & Discussion

It has recently become clear that metal nanocrystal etching studies in LCTEM have been controlled by redox processes of metal ions in solution. It is suggested that preloaded metal ions are oxidized under electron beam irradiation by radiolytically produced hydroxyl radicals.[83,84] This oxidized species then has the electrochemical potential to oxidize the metal nanocrystals in solution, a process which can be captured in real time in the TEM. This

redox cycling process can be inferred based on *in situ* TEM observations, yet direct evidence is lacking.

By using parallel-beam EELS, direct chemical insight into these transformations can be obtained, while irradiating the sample with the same conditions used in metal nanocrystal etching studies. In this work, we used EELS to gain experimental insight into the chemistry of the solution in graphene liquid cells (Figure 3.1a). Previous work has shown that the Ce^{3+}/Ce^{4+} redox couple is a suitable beam-initiated etchant for gold nanocrystals.[83] This system allows *in situ* observation of gold nanocrystal etching as preloaded $CeCl_3$ is oxidized to a Ce^{4+} species, forming a Ce^{3+}/Ce^{4+} redox couple with an electrochemical potential sufficiently positive to spontaneously etch gold nanocrystals (Figure 3.1b). Additionally, Ce^{3+} and Ce^{4+} have sharp $M_{4,5}$ edge white lines, which makes Ce readily identifiable with EELS. Further, Ce^{3+} and Ce^{4+} have distinct differences in fine structure, which can be seen in the spectra of the solid state standards for Ce^{3+} and Ce^{4+}, CeF_3 and CeO_2, respectively (Figure 3.1c). This enables chemical identification of the Ce oxidation state using EELS, making the Ce redox couple a suitable model system for determining electron beam-initiated transformations in graphene liquid cells. The M-edge of Ce^{3+} has two major peaks at 881.6 and 898.9 eV, as well as smaller features at 880.8, 895.9 and 897.5 eV. The M-edge of Ce^{4+} has two major peaks at slightly higher energies at 883.0 and 900.8 eV, as well as two satellite peaks at 888.3 and 906.0 eV that originate from the LMCT between the Ce metal center and the ligands.[154,155] For these reasons, we use EELS to study the Ce^{3+}/Ce^{4+} redox couple etching gold nanocrystals as a model system to probe the solution chemistry in graphene liquid cells.

The liquid pockets of a graphene liquid cell are typically formed through an evaporative drying process to seal the top and bottom graphene sheets together,[25,76] and it is possible that this may increase the concentration of species in solution. Of note, another well-developed liquid cell geometry is the SiN_x liquid cell, where a hermetic seal is formed between the o-rings and the SiN_x chips. Although this indicates that evaporation is not necessary to form a seal, as in graphene liquid cells, this does not preclude evaporation of the solvent. While it would be an interesting system to study, the facilities we used do not allow SiN_x liquid cells in the microscope, so we were unable to perform these measurements.

To measure the concentration of the encapsulated solution in graphene liquid cells, gold nanocrystals were added to the $CeCl_3$ solution and irradiated to induce etching before collecting an EEL spectrum. This is to confirm that the area under measurement was consistent with typical behavior observed in previous liquid cell studies.[83] Additionally, the irradiated area in these measurements was intentionally limited to a relatively small area (see 3.4) to attempt to fully capture liquid regions in these spectra. EELS was used to approximate the concentration of graphene liquid cells by taking the ratio of the oxygen K-edge and cerium M-edge signals and their respective cross sections for each measurement. In this system, oxygen is only present in water, and any oxygen coming from the grid should be negligible (see Figure A.3.1). We first measured the oxygen to cerium ratio for graphene liquid cells prepared with 40 mM $CeCl_3$, which is the same order of magnitude of oxidant used previously in etching studies.[76–79,83,84] Figure 3.2a shows a representative spectrum collected from these

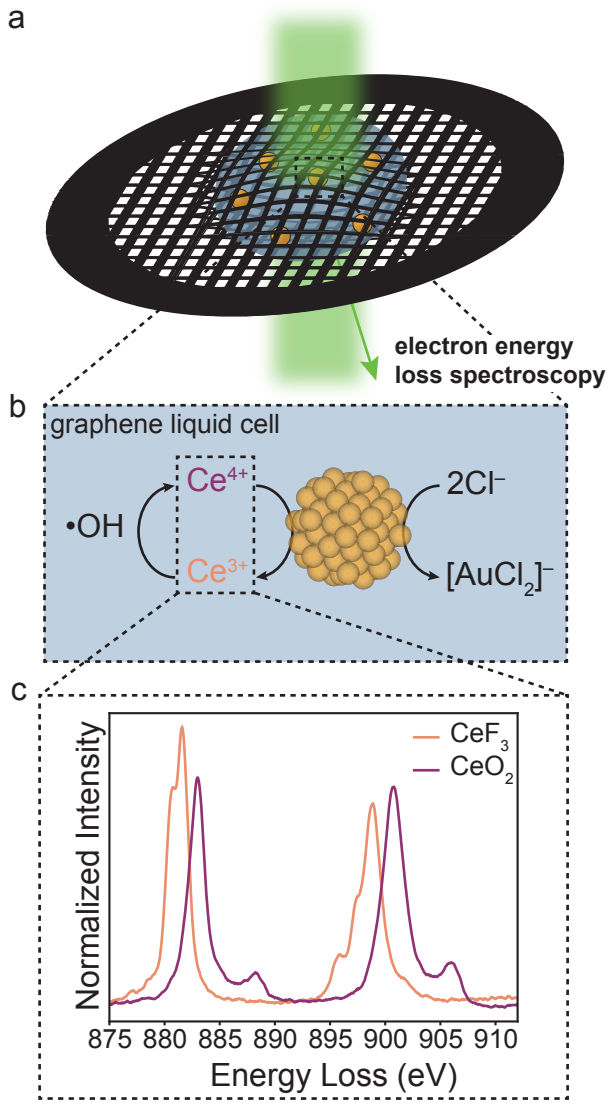

Figure 3.1: a) Schematic of a graphene liquid cell irradiated with an electron beam. b) Schematic of the proposed redox reactions occurring at the gold nanocrystal surface during electron beam initiated etching. c) Electron energy loss spectra of the Ce M-edge for CeF_3 (Ce^{3+}) and CeO_2 (Ce^{4+}). Note the distinct differences in the fine structure with the change in oxidation state.

graphene liquid cells (bottom), while Figure 3.2b shows the box plot of the measurements (right). The average oxygen to cerium ratio measured for the 40 mM solution is 3.46±2.72. In a 40 mM $CeCl_3$ solution, the ratio of oxygen to cerium atoms is approximately 1300 to 1. Additionally, the solubility limit of $CeCl_3$ in water is approximately 4 M, which corresponds to an oxygen to cerium ratio of 14 to 1. The ratios measured are significantly lower than what is expected, and also lower than the maximum solubility of a $CeCl_3$ solution. While it is possible that parts of the irradiated region were dry which could lower the measured ratio, the measured ratio is still three orders of magnitude lower than what is expected for a dilute solution. The lateral dimensions of the graphene liquid cell pockets are typically larger than the irradiated region used in these experiments, on the order of several hundred nanometers or more, (see Figure A.3.2 and[34,35]) indicating that it is likely that a significant portion of the irradiated region is hydrated. Further, time resolved thickness measurements and time resolved oxygen to cerium ratio measurements indicate that the solution is not evaporating upon exposure to the electron beam (see Figure A.3.3 and Figure A.3.4). Ultimately, while it is possible that the measurements underestimate the amount of water present, it is clear that the encapsulated solution is substantially more concentrated than the original solution.

Although the solution of the graphene liquid cells measured herein indicate that the encapsulated solution is highly concentrated, it may be possible to decrease the concentration of the encapsulated solution by preparing the graphene liquid cells with increasingly dilute initial solutions. We next prepared graphene liquid cells made with 4 mM and 0.4 mM $CeCl_3$. Gold nanocrystals were added to the initial solution, but we were unable to induce etching of the gold nanocrystals in most cases of graphene liquid cells prepared with 4 mM $CeCl_3$ and in all cases of the graphene liquid cells prepared with 0.4 mM $CeCl_3$. Representative spectra collected from these graphene liquid cells are shown in Figure 3.2a and box plots of the calculated oxygen to cerium ratios are shown in Figure 3.2b. The average oxygen to cerium ratio measured for the graphene liquid cells prepared with 4 mM and 0.4 mM $CeCl_3$ are 4.1 ±1.9, and 20.9 ±10.7, respectively. This data indicates that it is possible to create a more dilute solution in graphene liquid cells by preparing a more dilute initial solution, although the encapsulated solutions are, for the most part, still quite concentrated. When we prepared graphene liquid cells with 0.4 mM $CeCl_3$, the most dilute region we found had an oxygen to cerium ratio of 212 to 1, which corresponds to a concentration of approximately 260 mM. Beginning with a dilute initial solution appears to increase the chances of encapsulating a moderately dilute solution, yet there is still significant variability of the measured oxygen to cerium ratios across the initial concentrations and individual grids measured (see Figure A.3.5). Nevertheless, the purpose of this study is to understand the effects of the solution on gold nanocrystal etching in graphene liquid cells. In this context, reproducible etching trajectories of gold nanocrystals seem to occur in regions where the encapsulated solution is highly concentrated.

In addition to the EELS measurements of the oxygen to cerium ratios, we also used parallel beam Energy Dispersive Spectroscopy (EDS) to quantify the concentration of the encapsulated solution. With EDS, we could again illuminate the sample with the same irradiation source as is used for metal nanocrystal etching studies, but quantify the concentration

with another method. EDS data was collected on a graphene liquid cell prepared with a 40 mM $CeCl_3$ solution. A representative EDS spectrum and a box plot of the measured oxygen to cerium ratios are shown in Figure A.3.6. The average oxygen to cerium ratio measured with EDS is 4.73 ±1.33. This ratio is comparable to the ratio measured using EELS, and is significantly lower than what would be expected for a dilute solution.

We used an electron microscope for the majority of the data collection in this study due to its high spatial resolution and sensitivity to the chosen system. If we sacrifice the spatial resolution and acquire over a larger area, we can use another technique to corroborate the EELS and EDS results. We turned to Raman spectroscopy as an alternative method to measure the concentration of the graphene liquid cell solution. Previous work has shown that the shape of the OH stretching band in Raman changes as the hydration level of a $CeCl_3$ solution is modulated.[156] Water has two major OH stretching bands at 3200 cm^{-1} and 3405 cm^{-1} with a lower intensity shoulder at 3650 cm^{-1}. Dilute solutions of $CeCl_3$ have similar features, but when the concentration of $CeCl_3$ is increased above 3 M, the intensity of the band at 3200 cm^{-1} decreases significantly, while the band at 3650 cm^{-1} decreases entirely.[156] We performed Raman measurements on pure water and the 40 mM $CeCl_3$ solution used in this study and we get the same results as described above (Figure A.3.7, blue and black, respectively). We next measured the Raman signal of the same 40 mM $CeCl_3$ solution dropcast onto a glass slide and left to dry, to form a hydrated salt. We see that the major band at 3200 cm^{-1} and minor band at 3650 cm^{-1} have disappeared entirely, the other major band has shifted slightly to lower wavenumber and has sharpened significantly, and a shoulder around 3360 cm^{-1} appears (Figure A.3.7, grey). Direct assignment of this shoulder band is outside the scope of this work, but can be used as a fingerprint of the dried $CeCl_3$ salt.

We next performed Raman measurements on graphene liquid cells prepared with the 40 mM $CeCl_3$ solution using the lowest laser power possible as to not burst the liquid cell pocket. Accordingly, the signals from the graphene liquid cells are relatively weak, but bands around 3360 and 3405 cm^{-1} can be identified, while the bands at 3200 and 3600 cm^{-1} are absent (Figure A.3.7, green and pink), similar to the spectrum of the dried $CeCl_3$ salt. Of note, the relative intensity of the 3360 and 3405 cm^{-1} bands are variable across the individual measurements, indicating that environment of individual pockets may be variable, consistent with the EELS data.

From the EELS, EDS, and Raman data, it is apparent that the amount of water left in the encapsulating solution is significantly less than in the prepared, 40 mM $CeCl_3$ solution. The oxygen to cerium ratios measured in Figure 3.2 and A.3.6, and the Raman data in Figure A.3.7 indicate that the encapsulated solution may be better described as a hydrated salt matrix. With this in mind, we attempted to etch gold nanocrystals in a hydrated salt matrix by dropcasting the same 40 mM $CeCl_3$ solution onto a single grid, then let it dry under ambient conditions. For this experiment, there is no top grid present and the solution is not encapsulated. Upon imaging in the TEM, gold nanocrystals still etched, although it was considerably slower and less controlled than in a typical graphene liquid cell (see Figure A.3.8). Without a top grid present, volatile species (*e.g.* H_2, O_2 *etc.*) may leave the liquid,

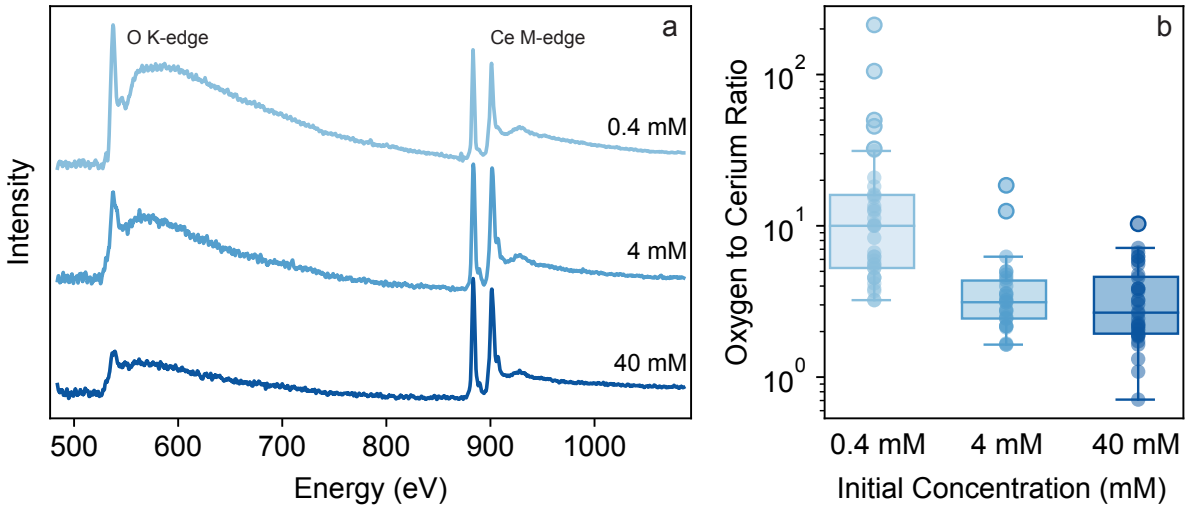

Figure 3.2: a) EELS core-loss and of graphene liquid cells prepared with a 0.4, 4, and 40 mM $CeCl_3$ solution. Note that the spectra are normalized to the Ce M-edge intensity to illustrate the varying amounts of oxygen present. b) Box plots of the ratio of the oxygen to cerium signals across the three different concentrations of encapsulating solutions used to prepare graphene liquid cells. The shaded region is the interquartile range of the data, the line in the box is the average, the end points of the whiskers are the range of the data, and outlined scatter point are outliers.

and thus cannot be recycled in chemical loops which have been postulated to be responsible for the consistent etching.

The high concentration of salt in the encapsulated solution in graphene liquid cells may have important implications for the kinetics of the chemical transformations in the solution. To probe this, we used time resolved EELS to study the oxidation of Ce^{3+} in a solution of 40 mM $CeCl_3$ and gold nanocrystals. Select spectra of a representative EELS time series collected at 375 $e^{-}Å^{-2}s^{-1}$ is shown in Figure 3.3a. Qualitatively, the initial spectrum is very similar to the Ce^{3+} standard spectrum, but the four features corresponding to the Ce^{4+} standard spectrum (dashed lines) as described above quickly develop. To ascertain how much Ce^{4+} is produced at each time step, a custom spectral deconvolution code was used to calculate the relative amount of Ce^{3+} and Ce^{4+} in each of these spectra (see SI for more details). In the first spectra at 0.1 s, there is approximately 9 % Ce^{4+} present in the graphene liquid cell (Figure 3.3c) and by 100.1 s there is 38 % Ce^{4+} present (Figure 3.3b). The percentage of Ce^{4+} was calculated for each of the ∼1200 spectra in the time series. By assuming that the average solution is $CeCl_3{\cdot}7H_2O$, a known hydrated cerium salt with an oxygen to cerium ratio within range of what was measured in Figure 3.2, these percentages can be converted to a concentration. A plot of the Ce^{4+} concentration over time is shown in Figure 3.3d. The initial increase in the Ce^{4+} concentration is very fast, followed by a slower increase until reaching a steady state concentration. The Ce^{4+} formation can be modeled with an empirical biexponential function with good fit (Figure 3.3d).

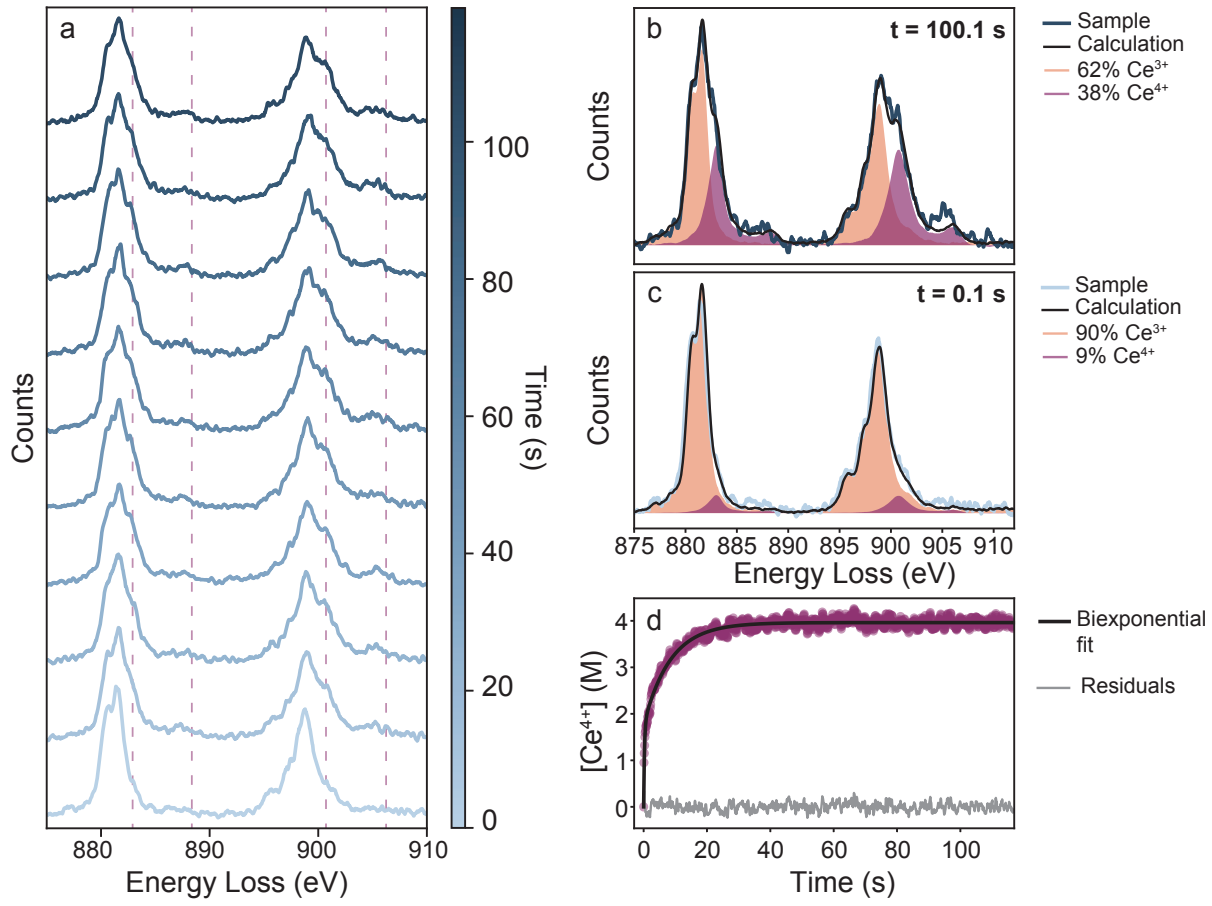

Figure 3.3: a) Time resolved EEL spectra of the Ce $M_{4,5}$ edge upon electron irradiation. Dashed lines indicate the features for Ce^{4+}. Deconvolution of the spectra taken at b) t=100.1s and c) t=0.1s indicating the relative contribution of Ce^{3+} and Ce^{4+} in each spectrum. d) Plot of the measured Ce^{4+} concentration for each spectra in the time series and the biexponential fit using the function $[Ce^{4+}] = A(1\text{-}e^{(-k_1 t)}) + B(1\text{-}e^{(-k_2 t)})$.

To gain further insight into the kinetics of formation of Ce^{4+} in the graphene liquid cell, approximately 60 different time series were captured at four different electron fluxes across several samples. The time-dependent Ce^{4+} concentration was calculated for each spectrum in the time series. Plots of the Ce^{4+} concentration over time at each of the four electron fluxes in shown in Figure 3.4a-d. The dark line is the average Ce^{4+} concentration at each electron flux, while the shaded region is the standard deviation of all the time series. While there is a large spread in Ce^{4+} concentration at a specific electron flux, the average steady state concentration of Ce^{4+} at each electron flux is similar (Figure 3.4e). To extract more information out of these curves, each individual time series was fit to the following empirical biexponential function

$$[Ce^{4+}] = A(1 - e^{(-k_1 t)}) + B(1 - e^{(-k_2 t)}) \tag{3.1}$$

where A and B are the total amount of Ce^{4+} formed through the fast and slow process, respectively, and k_1 and k_2 are the rate constants for the fast and slow process, respectively. Analysis of the fitting terms reveals that as the electron flux is increased, k_1 increases (Figure 4f). This indicates that at early times, the Ce^{4+} concentration increases faster at higher electron fluxes. See Figure A.3.9 for the other fitting terms.

To better understand how Ce^{4+} is formed in the graphene liquid cell, we used a radiolysis model derived from pulse radiolysis studies. This model included the generation of chemical species from electron-water interactions and homogeneous reactions between water-derived species and Ce or Cl species.[48,83] More information on this model is included in Figure A.3.10 and A.3.11. The initial concentration of Ce was set to 10.57 M, the molarity of cerium in $CeCl_3{\cdot}7H_2O$, which corresponds to the chemical species most closely matching the oxygen to cerium ratio observed with EELS. The model included dose partitioning between the solute and the solvent, which is required for models of highly concentrated solutions.[157] The results from this model insufficiently captured the observed Ce^{3+} oxidation kinetics, as indicated by the underestimation of the amount of Ce^{4+} generated (see Figure A.3.12). A sensitivity analysis of the reaction rate constants was performed to understand which reactions result in the discrepancy between experiment and theory (see Figure A.3.13 and Figure A.3.14). The sensitivity analysis indicated that the reaction rate constant between Ce^{3+} and hydroxyl radicals had to be over an order of magnitude faster to account for the experimental results (see Equation 3.2), while all other rate constants remained the same. It is expected that the increase in reactivity between hydroxyl radicals and Ce^{3+} is due to most of the water being associated with Ce^{3+} in the graphene liquid cell, and thus the hydroxyl radicals generated through radiolysis are in close proximity to the Ce^{3+} cation and react more readily. While this could be one potential explanation for this effect, more work is needed to understand the mechanism of Ce^{3+} oxidation.

$$Ce^{3+} + {}^{\bullet}OH \longrightarrow Ce^{4+} + OH^{-}; k = 2.27 \times 10^9 \tag{3.2}$$

The radiolysis model was also used to elucidate the variability in steady-state Ce^{4+} concentration observed between samples. Previous work indicates that the G-value of H_2

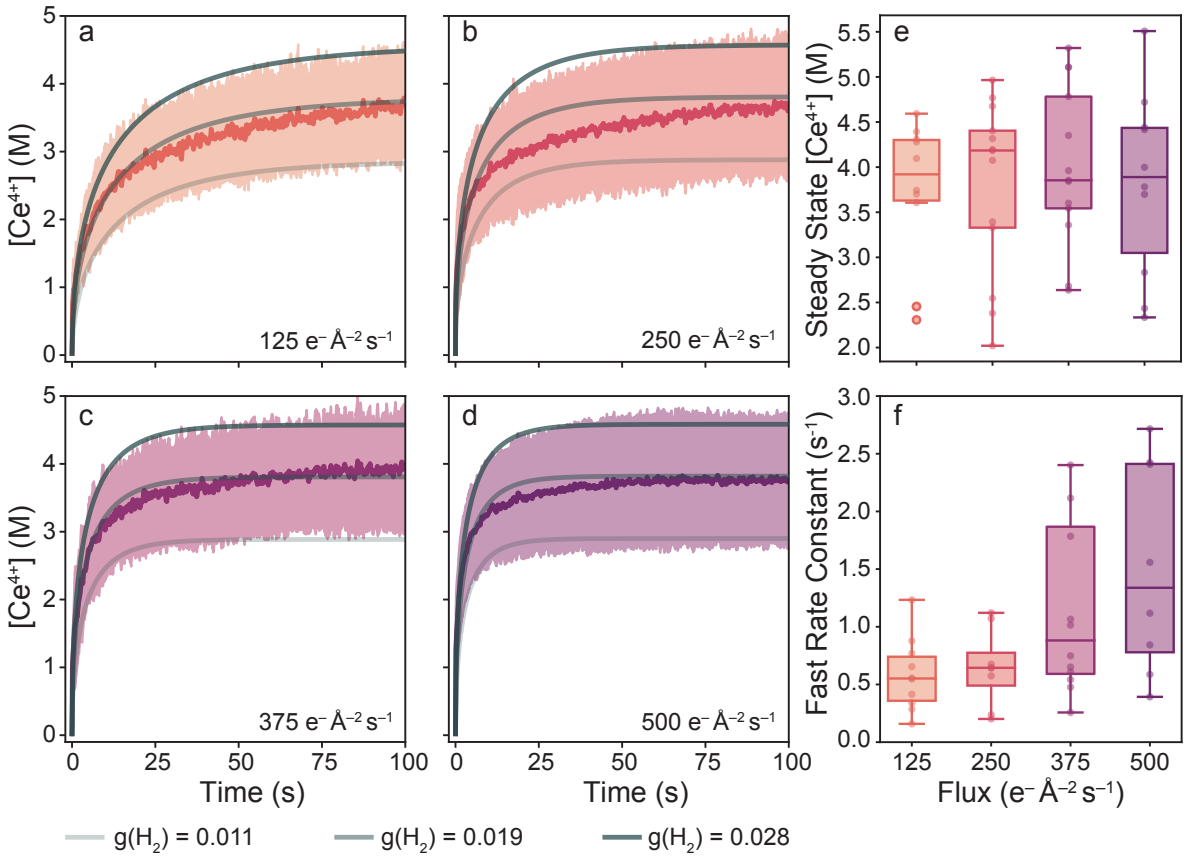

Figure 3.4: Average (dark line) and standard deviation (shaded region) of the measured Ce^{4+} concentration versus time at a) 125 b) 250 c) 375 and d) 500 $e^{-}Å^{-2}s^{-1}$. Overlaid lines are radiolytic model fits with a G-value for H_2 of 0.011 (light grey), 0.019 (grey), and 0.028 (dark grey). e) Box plots of the steady state concentration of Ce^{4+} at each of the electron fluxes. f) Box plots of the fast rate constant term at the four tested electron fluxes extracted from the biexponential fits for each time series.

changes as a solution becomes significantly concentrated.[158–160] Our simulations indicate that the steady-state concentration of Ce^{4+} is strongly dependent on the G-value of H_2. Simultaneous fitting of the radiolysis model including the changes described above to the experimental data resulted in an average H_2 G-value of 0.019 molecules/eV. G-values for H_2 in the range of 0.011 to 0.028 molecules/eV could explain the spread in steady-state Ce^{4+} concentration observed between samples (grey lines, Figure 3.4a-d). The updated model approximates the observed kinetics much more closely than the model for dilute solutions.

It is apparent that there are observable changes to the kinetics of Ce^{4+} formation in the graphene liquid cell under different electron fluxes. We correlated these effects with a model reaction that can be readily observed with LCTEM, the etching of gold nanocrystals by

Ce^{4+} cations. A graphene liquid cell was prepared with a solution containing pre-synthesized spherical gold nanocrystals and 40 mM $CeCl_3$. Dozens of gold nanocrystal etching trajectories were collected at the four different electron fluxes. Representative etching trajectories are shown in Figure 3.5a-d. The outline of the nanocrystal was calculated from each frame of the gold nanocrystal etching trajectory. Then, the radius of the nanocrystal at each frame of the video was determined and plotted versus time (Figure 3.5e). When plotting radius versus time, the plot is linear through the majority of the etching trajectory, as the radius is proportional to the surface etching rate (details of this analysis have been published previously).[83] The etch rate can then be calculated as the slope of the linear portion of the curve. The etch rate for each etching trajectory across the four electron fluxes was calculated and plotted in Figure 3.5f. This plot illustrates that the etch rate of gold nanocrystals increases with electron flux. Since there is substantial overlap between the time period prior to reaching steady-state Ce^{4+} concentration and time period of nanocrystal etching, it is expected that the generation rate of Ce^{4+} has an impact on the observed etching trajectories.

Moving forward, the insight obtained from this study will aid in the design and understanding of future graphene liquid cell experiments. This study highlights the importance of defining the solution in graphene liquid cells, as it can be significantly different from the prepared encapsulating solution. As shown in this work, solute species can be be highly concentrated in the graphene liquid cell, which can affect studies of chemical transformations in graphene liquid cells. Additionally, this result may impact studies of physical processes, such as dynamics and movement in graphene liquid cells. The dynamic viscosity of salt solutions increases as salinity increases,[161] which will affect the diffusion constant of nanocrystals through the Stokes-Einstein equation. Finally, care must be taken when using radiolysis models as they are designed for dilute solutions and may be inaccurate for the solutions in graphene liquid cells without further modifications specific to the graphene liquid cell environment.

Although we have shown that the nature of the encapsulated solution in graphene liquid cells have crucial differences compared to bulk solutions, these findings may be advantageous for future studies. Previous high-resolution imaging of nanocrystals in graphene liquid cells indicate that nanoscale tumbling of the particles is largely absent or significantly slowed down, which further supports that the nanocrystals are in a highly viscous medium. The suppressed tumbling in this highly viscous medium is likely key to 3D atomic resolution tomography in liquids[82,103] and enables the observation of facet dependent reactivity under different kinetic regimes.[79] While these findings may prompt reexamination of some previous work, we expect that the improved understanding of the liquid environment we have shown here will open up new directions of graphene liquid cell research.

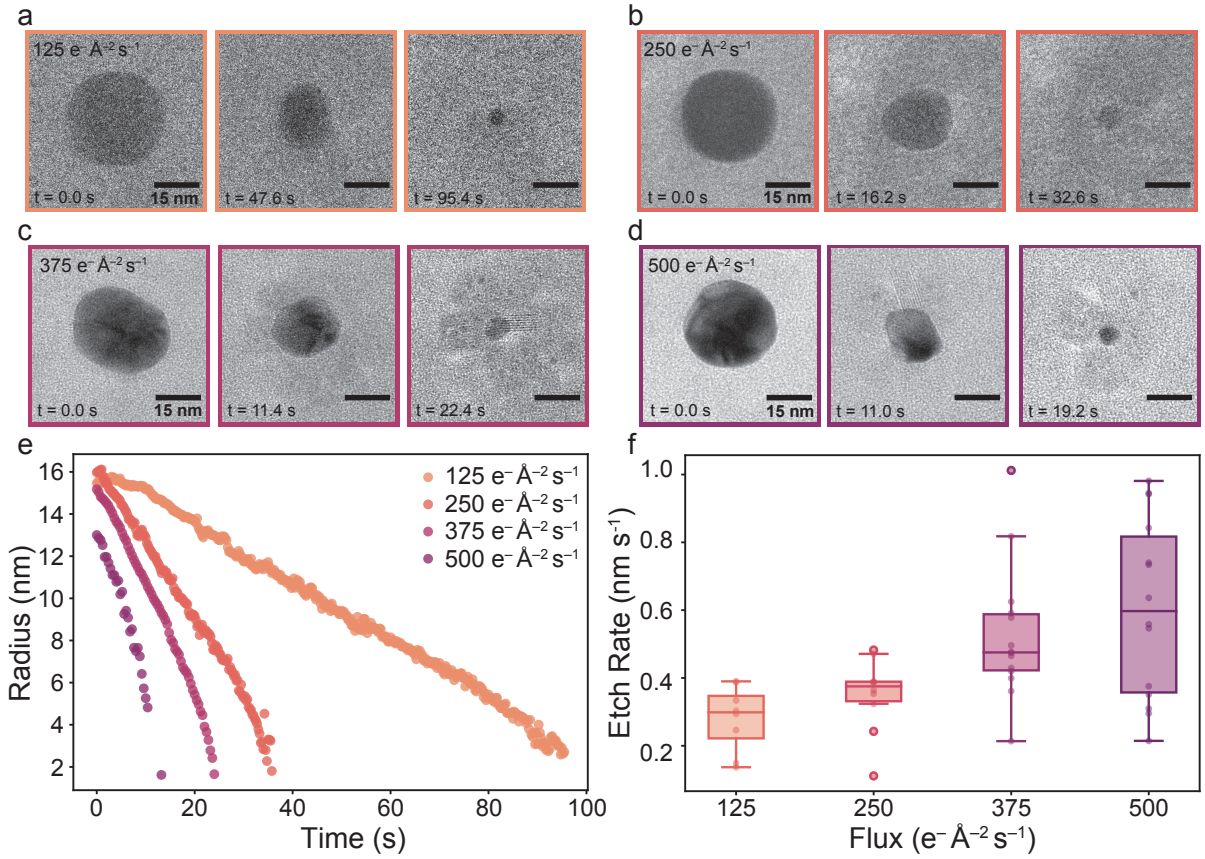

Figure 3.5: Etching trajectories of gold nanocrystals in a graphene liquid cell prepared with 40 mM $CeCl_3$ captured at a) 125, b) 250, c) 375, and d) 500 $e^-Å^{-2}s^{-1}$. e) Gold nanocrystal radius vs. time curves at each of the four electron fluxes. f) Box plots of the etch rates of gold nanocrystals at the four different electron fluxes.

3.3 Conclusion

Understanding the solution chemistry in graphene liquid cells is vital to interpret the results of liquid cell experiments. In this study, EELS was used to quantify specific solution parameters. By measuring the ratio between the O K-edge and Ce M-edge in graphene liquid cells prepared with 40, 4, and 0.4 mM $CeCl_3$, it was determined that the liquid cell solution is significantly more concentrated than the initial encapsulating solution. This likely occurs during the formation process as the seal is formed through evaporation of the solvent, indicating that this effect may extend to previous graphene liquid cell studies as well. Additionally, oxidation of the Ce^{3+} metal centers were tracked using time-resolved EELS. These experiments revealed that the rate of oxidation of the Ce^{3+} metal centers is dependent on the electron flux, while the steady state concentration of Ce^{4+} is independent of electron flux. Further analysis with kinetic radiolysis models revealed that the rate of oxidation and

spread in data can be rationalized by a highly concentrated solvent, with varying hydration levels in individual pockets. Finally, the flux-dependent rate of oxidation of the Ce^{3+} metal centers correlates well with the flux-dependent etching of gold nanocrystals. This study sheds new light on the nature of graphene liquid cell solutions and opens up new opportunities to study systems in dense electrolytes. The findings of this work will have implications for future graphene liquid cell experiments in a variety of fields, including chemistry, materials science, physics, and biology.

3.4 Materials and Methods

Nanocrystal Synthesis

Gold nanocrystals were synthesized following a modified procedure published previously.[96]

Preparation of Au Seeds

Briefly, 5 mL of 100 mM cetyltrimethylammonium ammonia chloride (CTAC) and 0.25 mL of 10 mM hydrochloroauric acid ($HAuCl_4$) were added to a clean, 20 mL vial. The vial was put into a water bath set to 30 °C and was stirred rapidly. Gold seeds were formed by adding 0.45 mL of 20 mM $NaBH_4$. The dispersion was allowed to stir for 1 minute, then left undisturbed at 30 °C for 1.5 hr to decompose any excess $NaBH_4$.

Preparation of Nanocrystals

Two identical solutions of 4.5 mL of 100 mM CTAC, 0.25 mL of 10 mM $HAuCl_4$, and 90 μL of 40 mM ascorbic acid were each added to clean 20 mL vials, in order. To the first vial, 1 mL of the seed solution was added during rapid stirring until the solution turned pale pink (approximately 5 s). Then, 12.5 μL of this solution was added into the other vial, briefly mixed, and left to sit on the bench for 15 mins to allow the growth to complete. The solution was then washed and resuspended in water three times by centrifugation at 8000 rpm for 10 minutes. After the final washing, the nanocrystals were concentrated to an OD of 1, then stored in a vial in the dark.

Graphene Liquid Cell Preparation

Graphene liquid cells were prepared as described previously[76] with modifications as follows. Prepared graphene-coated grids were used to encapsulate a solution of either 40 mM, 4, or 0.4 mM $CeCl_3$ in 40 mM HCl and the presynthesized gold nanocrystals. Approximately 0.5 μL of the encapsulating solution was placed on the graphene side of a graphene coated grid held in self-closing tweezers. A half-grid, prepared by cutting a grid with a razor, was

then immediately placed graphene side down on top of the droplet and left to dry for 10 minutes.

Electron Energy Loss Spectroscopy

All EELS experiments were performed in parallel-beam mode on the TEAM I double-corrected S/TEM microscope at the National Center for Electron Microscopy, Molecular Foundry, Lawrence Berkeley National Laboratory (LBNL). The microscope was operated at 300 kV with a high brightness 'X-FEG' electron source. A Gatan Continuum Imaging Filter with a 2.5 mm entrance aperture was used in conjunction with a K3 IS direct electron detector operated in electron-counting mode to collect the spectra. A source monochromator was used to obtain an energy resolution of approximately 0.25 eV. All data was collected in Dual EELS mode to capture the low loss and high loss regions simultaneously with the ZLP-lock function engaged to align spectra before summing to remove jitter in the elastic energy. The collection angle for all experiments was 25 mrad, set by a 100 μm objective aperture. The electron fluxes were calibrated on the camera. A custom script was used to control the microscope conditions (magnification, C2 lens %, etc.) when each spectra was acquired. The size of the irradiated area was then measured on the camera and determined to have a diameter of approximately 100 nm. All EELS analysis was performed in Python using custom scripts. All background subtraction was performed in Hyperspy using a power law model.

Time resolved EELS

The steps for collecting the time resolved EELS data are as follows. First, a suitable liquid pocket containing a gold nanocrystal was identified using low magnification and low electron flux (<1 $e^{-}Å^{-2}s^{-1}$) imaging conditions. Using a custom script, the microscope beam was blanked, then switched to a high magnification setting at the desired electron flux (125-500 $e^{-}Å^{-2}s^{-1}$) where only a region approximately 100 nm in diameter was irradiated. If the nanocrystals etched, indicating that the region was wet, then the beam was blanked, and the sample was moved to a location at least a few hundred nanometers away, outside the initial irradiated region. The EELS time series data collection feature in Digital Micrograph was initiated, then the beam was unblanked to ensure that the first electrons hitting the sample were collected in the time series. The time series were collected at 10 spectra per second for 2 minutes. A custom script was used to deconvolve the Ce^{3+} and Ce^{4+} contributions in each spectrum of the time series. More information on this script is provided in the SI.

Custom Spectral Deconvolution Code

A custom script was prepared to analyze the EELS data in this study. A copy of this script and a test data set are provided as well, and is described briefly here. First, spectra for the solid-state standards for Ce^{3+} and Ce^{4+}, CeF_3 and CeO_2, were collected (see Figure

3.1). These spectra were background subtracted with a power-law model, then an arctan function was fit to the remaining background to remove the step in the M_4-edge. These spectra were normalized to the integrated area of the remaining $M_{4,5}$ edge.

For the time-resolved EELS spectra, both the high-loss and low-loss data were collected simultaneously. Each high-loss spectrum was zeroed and deconvolved with the respective low-loss spectrum to set the correct energy scale and remove any effects of plural scattering. To increase the signal-to-noise for more reliable background subtraction, five spectra were averaged together, background subtracted using a power-law model, and an arctan function was removed from the M_4-edge. This was completed for the entire time series using a five spectra moving average. With the standard spectra, a linear least squares analysis was used to determine the relative amount of Ce^{3+} and Ce^{4+} in each five-spectrum average of the time series.

In Situ TEM Imaging

All BF-TEM videos were collected on a FEI Tecnai T-20 S-Twin TEM operating at 200 kV with a LaB_6 filament. *In situ* videos were collected with a Gatan Rio 16 IS camera using the Digital Micrograph *in situ* data collection function. Videos were binned by two for a 2048 $\times$ 2048 pixel area. The nominal magnification for all videos was 145 kx for a pixel resolution of 0.92 Å/pixel. The frame rate for all videos was either 4 or 10 fps, yielding a temporal resolution of 0.25 and 0.1 s, respectively. To convert counts to electrons, a conversion value of 124 counts/electron (provided by the manufacturer) was used. The electron flux was calibrated using a custom script[77] and checked several times throughout a session to maintain accuracy. When searching for nanocrystals, the electron flux was kept low (<15 $e^{-}Å^{-2}s^{-1}$) to prevent electron-beam induced reactions prior to video collection. Of note, although there is recent work suggesting the beam induced heating could be significant in the liquid cell, measuring and calibrating heating for individual experiment is still challenging so we have not included any heating effects into our analysis.

Radiolysis Chemical Network Model

A literature kinetic model was adjusted based on the EELS data collected herein on the kinetics of Ce^{3+} oxidation during graphene LCTEM imaging. The model is based on the MATLAB code written by Schneider et al., which implements a kinetic model by Elliot and McCracken.[44,48] The model includes previously reported reactions between species derived from water, chloride, and cerium.[48,83,157] Table A.5 summarizes the reactions used to model the effect of Cl and Ce additives. All water-based reactions (reactions 1-73) are as reported in Schneider et al.[48]. For all simulation conditions the solution is treated as homogeneous, allowing the simulation to be solved via a set of coupled ordinary differential equations as shown on Equation 3.3.

$$\frac{\partial C_i}{\partial t} = \sum_{j,k \neq i} k_{jk} C_j C_k - \sum_j k_{ij} C_i C_j + R_i \tag{3.3}$$

Where k_{jk} and k_{ij} are reaction rate constants, C_i, C_j, and C_k are reactant concentrations, and R_i is the electron beam induced generation of chemical species. The electron beam induced generation was determined according to Equation 3.4.

$$R_i = f_i \rho \psi G_i \tag{3.4}$$

Where f_i is the molar fraction of water in the graphene liquid cell solution, ρ is the liquid density, ψ is the electron dose rate, and G_i is the G-value for chemical species. A liquid density of 3.94 mg/mL was used, corresponding to the density of $CeCl_3 \bullet 7H_2O$. A total stopping power of 1.839 MeV cm2/g per electron at 300 keV was used to convert the electron beam dose to absorbed dose in Gy/s.[162] Table A.6 summarizes the G-values used for the chemical species in this model. The G-values for $HO_2^\bullet$ and H_2O were determined according to mass conservation principles, as shown on Equations 3.5 and 3.6.

$$G_{HO_2\bullet} = \frac{1}{3}[G_{H^+} - G_{OH^-} - 2G_{H_2O_2} + G_{H\bullet} - G_{HO\bullet} + 2G_{H_2}] \tag{3.5}$$

$$G_{H_2O} = -[G_{HO\bullet} + 2G_{H_2O_2} + 2G_{HO_2\bullet} + G_{OH^-}] \tag{3.6}$$

Energy Dispersive X-ray Spectroscopy (EDS)

All EDS experiments were performed in parallel-beam mode on the FEI ThemIS 60-300 STEM/TEM microscope at the National Center for Electron Microscopy, Molecular Foundry, Lawrence Berkeley National Laboratory (LBNL). An FEI low background double tilt holder was used for all experiments. The microscope was operated at 300 kV with a probe current of 1.2 nA (approximate electron flux of 2500 $e^- Å^{-2} s^{-1}$) using a Bruker windowless EDS detector with a solid angle of 0.7 steradians. Data was collected and quantified with the Thermo Scientific Velox software using the K series for O and the M and L series for Ce. Care was taken to ensure that the same beam conditions (magnification, C2 lens %, etc.) were used when taking EDS spectra of the graphene liquid cells. After the EDS spectra were collected, the size of the beam was measured on the camera and was determined to have a diameter of approximately 190 nm.

Energy Filtered TEM

All EFTEM experiments were performed on the TEAM I double-corrected S/TEM microscope at the National Center for Electron Microscopy, Molecular Foundry, Lawrence Berkeley National Laboratory (LBNL). The microscope was operated at 300 kV with a high brightness 'X-FEG' electron source. A Gatan Continuum Imaging Filter with a 2.5 mm entrance

aperture was used in conjunction with a K3 IS direct electron detector operated in electron-counting mode to collect the images. The thickness mapping mode was selected to collect the images.

Raman Spectroscopy

All Raman measurements were performed using a HORIBA LabRAM HR Evolution Confocal Raman Microscope. All measurements were performed using a 532 nm laser source, an ultra-low frequency filter enabling measurement of Raman shifts as low as 10 cm^{-1}, a 600 grooves/mm grating (resolution 2-3 cm^{-1}) and detected using a Horiba Synapse OE-CCD. For solution measurements, the laser light was focused onto the solution held in a quartz cuvette using a 50x long working distance objective. For samples in graphene liquid cells, laser light was focused onto the liquid samples using a 100x air objective. All measurements were performed with the minimum power needed to acquire a measurable signal. For the GLC samples, all measurements were performed with identical laser power. The spectrometer was calibrated using the Horiba LabSpec software using a Si (111) reference sample for all measurements. An attempt was made to measure the temperature of the samples during measurement using the Stokes/anti-Stokes ratio of the graphene G-band. However, even with increasing the laser power by a factor of 5, no anti-Stokes peak was observed.

Chapter 4

Conclusions and Outlook

4.1 Conclusions

As is evident in Chapters 2 and 3, several solution species inaccessible to TEM imaging can have a great effect on the present solution chemistry. Carefully designed imaging studies, such as the halide study in Chapter 2 can help infer what chemistry is present, but ultimately, correlative studies such as pulse radiolysis and EELS provide deeper insight into the species present and mechanisms at play. The pulse radiolysis studies of iron additives in Chapter 2 allowed deeper investigation of a previously suggested mechanism. The pulse radiolysis studies indicated that the preloaded $FeCl_3$ is oxidized to its active form, and this oxidized iron species participates in the gold oxidation. This information would have been extremely challenging to deduce without the spectroscopic insight from pulse radiolysis. Although pulse radiolysis exposes the solution to very similar conditions experienced in the TEM, which makes it a useful technique to understand the solution chemistry, ultimately there are still differences in the solution chemistry between these two techniques, largely due to the difference in duration of the electron beam exposure. EELS has the advantage that it exposes the solution to the exact same conditions as in liquid cell TEM imaging and can be performed *in situ*. As seen in Chapter 3, EELS is a powerful tool to study the solution chemistry, providing direct evidence of *in situ* oxidation. In this work, a $CeCl_3$ additive was used as it is also known to induce etching of metal nanocrystals *in situ*, but is a better spectroscopic probe for EELS. This study provided direct, experimental evidence of the $CeCl_3$ (a Ce^{3+} species) being oxidized to a Ce^{4+} species *in situ*. This *in situ* oxidation is analogous to the $FeCl_3$ oxidation determined using pulse radiolysis in Chapter 2. The ability to measure these solvated species directly in the liquid cell also led to the discovery that the concentration of the solution in graphene liquid cells is orders of magnitude higher than the encapsulating solution. This is likely due to the evaporative drying process used to form the hermetic seals in the graphene liquid cells. Ultimately, directly probing the solution species *in situ* has given us much greater understanding of the solution chemistry, and has allowed us to begin to modify the commonly used kinetic radiolysis models. Comparing

the outputs of the kinetic radiolysis models to the oxidation profiles captured using EELS show obvious discrepancy. However, these measurements allow us to begin to create a more accurate kinetic model based on liquid cell TEM results, to better understand the solution chemistry in liquid cell TEM moving forward.

4.2 Outlook for Graphene Liquid Cell TEM

The work presented herein has some important implications for the use of graphene liquid cells moving forward. Significantly, the *in situ* EELS work presented in Chapter 3 directly shows that the individual regions in graphene liquid cells are not chemically identical. This could be one explanation of the large error bars seen in many chemical transformations studied with graphene liquid cell, including the halide study in Chapter 2. Further, this indicates that repeat experiments may not be probing exactly the same chemistry. In order to develop this technique further into a robust characterization tool, there must be better control over the concentration of the species inside the individual liquid pockets. Moving forward, in order to precisely control the chemical environment in graphene liquid cells to truly perform repeat experiments, it is imperative that the graphene liquid cells are prepared with better control. The sandwich-type liquid cells used in Chapters 2 and 3 are formed stochastically through the evaporative drying process, thus control over the formation of the individual pockets is poor. Moving towards the next-generation liquid cells described in Chapter 1 should provide much better control over the chemical environment. Addtionally, methods which could ensure that the encapsulated solution is dilute, such as flowing in additional liquid[37] could help ensure the concentration is controlled.

Ultimately, with these adaptations, it is still imperative to characterize the solution and develop better models to understand and explain the observed chemistry. Chapter 3 showed that it is possible to directly track and measure solution chemistry inside the liquid cell. While this method is certainly not feasible for every chemical transformation of interest, building up an understanding of the chemistry inside the liquid cell, rather than relying solely on bulk measurements will be important in the long term. Kinetic models that are used today will continue to be highly valuable, but continual adjustments to the model based on liquid cell TEM measurements will allow these models to evolve with the liquid cell TEM technique.

Bibliography

(*1*) Bardell, D. (2004). The Invention of the Microscope. *Bios 75*, 78–84.

(*2*) Davisson, C. J., and Germer, L. H. (1928). Reflection and Refraction of Electrons by a Crystal of Nickel. *Proceedings of the National Academy of Sciences 14*, 619–627.

(*3*) Ruska, E., *The Early Development of Electron Lenses and Electron Microscopy*, First; Translated by T. Mulvey, Ed.; S. Hirzel: 1980, p 820.

(*4*) Kawasaki, T., Yoshida, T., Matsuda, T., Osakabe, N., Tonomura, A., Matsui, I., and Kitazawa, K. (2000). Fine crystal lattice fringes observed using a transmission electron microscope with 1 MeV coherent electron waves. *Applied Physics Letters 76*, 1342–1344.

(*5*) Batson, P. E. (2002). Sub-angstrom resolution using aberration corrected electron optics. *Nature 418*, 617–620.

(*6*) Haider, M., Uhlemann, S., Schwan, E., Rose, H., Kabius, B., and Urban, K. (1998). Electron microscopy image enhanced. *Nature 392*, 768–769.

(*7*) Erni, R., Rossell, M. D., Kisielowski, C., and Dahmen, U. (2009). Atomic-Resolution Imaging with a Sub-50-pm Electron Probe. *Physical Review Letters 102*, 096101.

(*8*) Sawada, H., Tanishiro, Y., Ohashi, N., Tomita, T., Hosokawa, F., Kaneyama, T., Kondo, Y., and Takayanagi, K. (2009). STEM imaging of 47-pm-separated atomic columns by a spherical aberration-corrected electron microscope with a 300-kV cold field emission gun. *Journal of Electron Microscopy 58*, 357–361.

(*9*) Kisielowski, C. et al. (2008). Detection of single atoms and buried defects in three dimensions by aberration-corrected electron microscope with 0.5-Å information limit. *Microscopy and Microanalysis 14*, 469–477.

(*10*) Kisielowski, C., Hetherington, C. J., Wang, Y. C., Kilaas, R., O'Keefe, M. A., and Thust, A. (2001). Imaging columns of the light elements carbon, nitrogen and oxygen with sub Ångstrom resolution. *Ultramicroscopy 89*, 243–263.

(*11*) O'Keefe, M. A., Hetherington, C. J., Wang, Y. C., Nelson, E. C., Turner, J. H., Kisielowski, C., Malm, J. O., Mueller, R., Ringnalda, J., Pan, M., and Thust, A. (2001). Sub-Ångstrom high-resolution transmission electron microscopy at 300keV. *Ultramicroscopy 89*, 215–241.

(*12*) Nellist, P. D., Chisholm, M. F., Dellby, N., Krivanek, O. L., Murfitt, M. F., Szilagyi, Z. S., Lupini, A. R., Borisevich, A., Sides, W. H., and Pennycook, S. J. (2004). Direct sub-angstrom imaging of a crystal lattice. *Science 305*, 1741.

(*13*) Crewe, A. V., Wall, J., and Langmore, J. (1970). Visibility of Single Atoms. *Science 168*, 1338–1340.

(*14*) Meyer, J. C., Girit, C. O., Crommie, M. F., and Zettl, A. (2008). Imaging and dynamics of light atoms and molecules on graphene. *Nature 454*, 319–322.

(*15*) Abrams, I. M., and McBain, J. W. (1944). A closed cell for electron microscopy. *Journal of Applied Physics 15*, 607–609.

(*16*) Ercius, P., Hachtel, J. A., and Klie, R. F. (2020). Chemical and bonding analysis of liquids using liquid cell electron microscopy. *MRS Bulletin 45*, 761–768.

(*17*) Williamson, M. J., Tromp, R. M., Vereecken, P. M., Hull, R., and Ross, F. M. (2003). Dynamic microscopy of nanoscale cluster growth at the solid-liquid interface. *Nature Materials 2*, 532–536.

(*18*) Yuk, J. M., Park, J., Ercius, P., Kim, K., Hellebusch, D. J., Crommie, M. F., Lee, J. Y., Zettl, A., and Alivisatos, A. P. (2012). High-Resolution EM of Colloidal Nanocrystal Growth Using Graphene Liquid Cells. *Science 336*, 61–64.

(*19*) Touve, M. A., Carlini, A. S., and Gianneschi, N. C. (2019). Self-assembling peptides imaged by correlated liquid cell transmission electron microscopy and MALDI-imaging mass spectrometry. *Nature Communications 10*, 1–12.

(*20*) Liao, H.-G., Zherebetskyy, D., Xin, H., Czarnik, C., Ercius, P., Elmlund, H., Pan, M., Wang, L.-W., and Zheng, H. (2014). Facet development during platinum nanocube growth. *Science 345*, 916–919.

(*21*) Zhang, J., Lin, L., Sun, L., Huang, Y., Koh, A. L., Dang, W., Yin, J., Wang, M., Tan, C., Li, T., Tan, Z., Liu, Z., and Peng, H. (2017). Clean Transfer of Large Graphene Single Crystals for High-Intactness Suspended Membranes and Liquid Cells. *Advanced Materials 29*, 1700639.

(*22*) Wang, C., Qiao, Q., Shokuhfar, T., and Klie, R. F. (2014). High-resolution electron microscopy and spectroscopy of ferritin in biocompatible graphene liquid cells and graphene sandwiches. *Advanced Materials 26*, 3410–3414.

(*23*) Kelly, D. J., Zhou, M., Clark, N., Hamer, M. J., Lewis, E. A., Rakowski, A. M., Haigh, S. J., and Gorbachev, R. V. (2018). Nanometer Resolution Elemental Mapping in Graphene-Based TEM Liquid Cells. *Nano Letters 18*, 1168–1174.

(*24*) Clark, N., Kelly, D. J., Zhou, M., Zou, Y. C., Myung, C. W., Hopkinson, D. G., Schran, C., Michaelides, A., Gorbachev, R., and Haigh, S. J. (2022). Tracking single adatoms in liquid in a transmission electron microscope. *Nature 609*, 942–947.

(*25*) Park, J., Koo, K., Noh, N., Chang, J. H., Cheong, J. Y., Dae, K. S., Park, J. S., Ji, S., Kim, I. D., and Yuk, J. M. (2021). Graphene Liquid Cell Electron Microscopy: Progress, Applications, and Perspectives. *ACS Nano 15*, 288–308.

(*26*) Wang, Y., Peng, X., Abelson, A., Xiao, P., Qian, C., Yu, L., Ophus, C., Ercius, P., Wang, L.-W., Law, M., and Zheng, H. (2019). Dynamic deformability of individual PbSe nanocrystals during superlattice phase transitions. *Science Advances 5*, eaaw5623.

(*27*) Yuk, J. M., Kim, K., Alemán, B., Regan, W., Ryu, J. H., Park, J., Ercius, P., Lee, H. M., Alivisatos, A. P., Crommie, M. F., Lee, J. Y., and Zettl, A. (2011). Graphene veils and sandwiches. *Nano Letters 11*, 3290–3294.

(*28*) Ghodsi, S. M., Anand, S., Shahbazian-Yassar, R., Shokuhfar, T., and Megaridis, C. M. (2019). In Situ Study of Molecular Structure of Water and Ice Entrapped in Graphene Nanovessels. *ACS Nano 13*, 4677–4685.

(*29*) Jeong, M., Yuk, J. M., and Lee, J. Y. (2015). Observation of Surface Atoms during Platinum Nanocrystal Growth by Monomer Attachment. *Chemistry of Materials 27*, 3200–3202.

(*30*) Keskin, S., Kunnas, P., and de Jonge, N. (2019). Liquid-Phase Electron Microscopy with Controllable Liquid Thickness. *Nano Letters 19*, 4608–4613.

(*31*) de Jonge, N., Peckys, D. B., Kremers, G. J., and Piston, D. W. (2009). Electron microscopy of whole cells in liquid with nanometer resolution. *Proceedings of the National Academy of Sciences 106*, 2159–2164.

(*32*) Sutter, E. A., and Sutter, P. W. (2017). In situ liquid cell electron microscopy of Ag–Au galvanic replacement reactions. *Nanoscale 9*, 1271–1278.

(*33*) Sutter, E., Jungjohann, K., Bliznakov, S., Courty, A., Maisonhaute, E., Tenney, S., and Sutter, P. (2014). In situ liquid-cell electron microscopy of silver–palladium galvanic replacement reactions on silver nanoparticles. *Nature Communications 5*, 4946.

(*34*) Sasaki, Y., Kitaura, R., Yuk, J. M., Zettl, A., and Shinohara, H. (2016). Efficient preparation of graphene liquid cell utilizing direct transfer with large-area well-stitched graphene. *Chemical Physics Letters 650*, 107–112.

(*35*) Chen, Q., Smith, J. M., Park, J., Kim, K., Ho, D., Rasool, H. I., Zettl, A., and Alivisatos, A. P. (2013). 3D Motion of DNA-Au Nanoconjugates in Graphene Liquid Cell Electron Microscopy. *Nano Letters 13*, 4556–4561.

(*36*) Ghodsi, S. M., Sharifi-Asl, S., Rehak, P., Král, P., Megaridis, C. M., Shahbazian-Yassar, R., and Shokuhfar, T. (2020). Assessment of Pressure and Density of Confined Water in Graphene Liquid Cells. *Advanced Materials Interfaces 7*, 1–10.

(*37*) Dunn, G., Adiga, V. P., Pham, T., Bryant, C., Horton-Bailey, D. J., Belling, J. N., Lafrance, B., Jackson, J. A., Barzegar, H. R., Yuk, J. M., Aloni, S., Crommie, M. F., and Zettl, A. (2020). Graphene-Sealed Flow Cells for in Situ Transmission Electron Microscopy of Liquid Samples. *ACS Nano 14*, 9637–9643.

(*38*) Woehl, T., and Abellan, P. (2017). Defining the radiation chemistry during liquid cell electron microscopy to enable visualization of nanomaterial growth and degradation dynamics. *Journal of Microscopy 265*, 135–147.

(*39*) Schwarz, H. A. (1969). Applications of the spur diffusion model to the radiation chemistry of aqueous solutions. *The Journal of Physical Chemistry 73*, 1928–1937.

(*40*) Allen, A., *The radiation chemistry of water and aqueous solutions.* Van Nostrand: Princeton N.J., 1961, p 204.

(*41*) Draganić, I. G., and Draganić, Z. D. In *The Radiation Chemistry of Water*; Academic Press, INC.: New York and London, 1971, pp 23–46.

(*42*) Hill, M., and Smith, F. (1994). Calculation of initial and primary yields in the radiolysis of water. *Radiation Physics and Chemistry 43*, 265–280.

(*43*) Buxton, G. V., Greenstock, C. L., Helman, W. P., and Ross, A. B. (1988). Critical Review of rate constants for reactions of hydrated electrons, hydrogen atoms and hydroxyl radicals (OH/O in Aqueous Solution. *Journal of Physical and Chemical Reference Data 17*, 513–886.

(*44*) Elliot, A. J., and McCracken, D. R. (1990). Computer modelling of the radiolysis in an aqueous lithium salt blanket: Suppression of radiolysis by addition of hydrogen. *Fusion Engineering and Design 13*, 21–27.

(*45*) Pastina, B., and LaVerne, J. A. (2001). Effect of Molecular Hydrogen on Hydrogen Peroxide in Water Radiolysis. *The Journal of Physical Chemistry A 105*, 9316–9322.

(*46*) Henglein, A., Spinks, J. W. T., and Woods, R. J. (1991). An Introduction to Radiation Chemistry. *Berichte der Bunsengesellschaft für physikalische Chemie 95*, 451–451.

(*47*) Le Caër, S. (2011). Water Radiolysis: Influence of Oxide Surfaces on H2 Production under Ionizing Radiation. *Water 3*, 235–253.

(*48*) Schneider, N. M., Norton, M. M., Mendel, B. J., Grogan, J. M., Ross, F. M., and Bau, H. H. (2014). Electron–Water Interactions and Implications for Liquid Cell Electron Microscopy. *The Journal of Physical Chemistry C 118*, 22373–22382.

(*49*) Armstrong, D. A., Huie, R. E., Koppenol, W. H., Lymar, S. V., Merényi, G., Neta, P., Ruscic, B., Stanbury, D. M., Steenken, S., and Wardman, P. (2015). Standard electrode potentials involving radicals in aqueous solution: inorganic radicals (IUPAC Technical Report). *Pure and Applied Chemistry 87*, 1139–1150.

(*50*) Atkins, P., and Shriver, D., *Inorganic Chemistry*, Fifth; W. H. Freeman: 2009, p 153.

(*51*) Aylward, G. H., and Findlay, T. J. V., *SI Chemical Data*, Sixth Edit; Wiley: 2008.

(*52*) Bard, A. J., *Standard Potentials in Aqueous Solution*, First Edit; CRC Press: 1985.

(*53*) Atkins, P. W., *Physical Chemistry*, Sixth Edit; W. H. Freeman & Co.: 1998.

(*54*) Bard, A. J., and Falkner, L. R., *Electrochemical Methods: Fundamentals and Applications*, 2nd Ed.; Wiley: 2001, p 864.

(*55*) Center for Disease Control Acute Radiation Syndrome: A Fact Sheet for Physicians, 2018.

(*56*) Medvedev, Z. A., *The Legacy of Chernobyl*, 1st American; W. W. Norton & Co. Inc.: 1990, pp 42–50.

(*57*) Belloni, J., Mostafavi, M., Remita, H., Marignier, J.-L., Delcourt, and Marie-Odile (1998). Radiation-induced synthesis of mono- and multi-metallic clusters and nanocolloids. *New Journal of Chemistry 22*, 1239–1255.

(*58*) Alam, M. S., Maisonhaute, E., Rose, D., Demarque, A., Larbre, J.-P., Marignier, J.-L., and Mostafavi, M. (2013). Concomitant transient electrochemical and spectroscopic detection with electron pulse radiolysis. *Electrochemistry Communications 35*, 149–151.

(*59*) LaVerne, J. A., and Pimblott, S. M. (1991). Scavenger and time dependences of radicals and molecular products in the electron radiolysis of water: examination of experiments and models. *The Journal of Physical Chemistry 95*, 3196–3206.

(*60*) Cho, H., Jones, M. R., Nguyen, S. C., Hauwiller, M. R., Zettl, A., and Alivisatos, A. P. (2017). The Use of Graphene and Its Derivatives for Liquid-Phase Transmission Electron Microscopy of Radiation-Sensitive Specimens. *Nano Letters 17*, 414–420.

(*61*) Woehl, T. J., Jungjohann, K. L., Evans, J. E., Arslan, I., Ristenpart, W. D., and Browning, N. D. (2013). Experimental procedures to mitigate electron beam induced artifacts during in situ fluid imaging of nanomaterials. *Ultramicroscopy 127*, 53–63.

(*62*) Noh, K. W., Liu, Y., Sun, L., and Dillon, S. J. (2012). Challenges associated with in-situ TEM in environmental systems: The case of silver in aqueous solutions. *Ultramicroscopy 116*, 34–38.

(*63*) Abellan, P., Parent, L. R., Al Hasan, N., Park, C., Arslan, I., Karim, A. M., Evans, J. E., and Browning, N. D. (2016). Gaining Control over Radiolytic Synthesis of Uniform Sub-3-nanometer Palladium Nanoparticles: Use of Aromatic Liquids in the Electron Microscope. *Langmuir 32*, 1468–1477.

(*64*) Yu, C., Zhang, B., Yan, F., Zhao, J., Li, J., Li, L., and Li, J. (2016). Engineering nano-porous graphene oxide by hydroxyl radicals. *Carbon 105*, 291–296.

(*65*) Radich, E. J., and Kamat, P. V. (2013). Making Graphene Holey . Gold-Nanoparticle-Mediated Hydroxyl Radical Attack on Reduced Graphene Oxide. *ACS Nano 7*, 5546–5557.

(*66*) Qiu, Y., Wang, Z., Owens, A. C. E., Kulaots, I., Chen, Y., Kane, A. B., and Hurt, R. H. (2014). Antioxidant chemistry of graphene-based materials and its role in oxidation protection technology. *Nanoscale 6*, 11744–11755.

(*67*) Jungjohann, K. L., Bliznakov, S., Sutter, P. W., Stach, E. A., and Sutter, E. A. (2013). In Situ Liquid Cell Electron Microscopy of the Solution Growth of Au–Pd Core–Shell Nanostructures. *Nano Letters 13*, 2964–2970.

(*68*) Chen, F.-C., Chen, J.-y., Lin, Y.-h., Kuo, M.-y., Hsu, Y.-j., and Wu, W.-w. (2019). In situ TEM observation of Au–Cu_2O core–shell growth in liquids. *Nanoscale 11*, 10486–10492.

(*69*) Canepa, S. A., Sneed, B. T., Sun, H., Unocic, R. R., and Mølhave, K. (2018). Influence of Cetyltrimethylammonium Bromide on Gold Nanocrystal Formation Studied by In Situ Liquid Cell Scanning Transmission Electron Microscopy. *The Journal of Physical Chemistry C 122*, 2350–2357.

(*70*) Radisic, A., Vereecken, P. M., Hannon, J. B., Searson, P. C., and Ross, F. M. (2006). Quantifying Electrochemical Nucleation and Growth of Nanoscale Clusters Using Real-Time Kinetic Data. *Nano Letters 6*, 238–242.

(*71*) Jin, B., Sushko, M. L., Liu, Z., Cao, X., Jin, C., and Tang, R. (2019). Understanding Anisotropic Growth of Au Penta-Twinned Nanorods by Liquid Cell Transmission Electron Microscopy. *The Journal of Physical Chemistry Letters 10*, 1443–1449.

(*72*) Wang, M., Park, C., and Woehl, T. J. (2018). Quantifying the Nucleation and Growth Kinetics of Electron Beam Nanochemistry with Liquid Cell Scanning Transmission Electron Microscopy. *Chemistry of Materials 30*, 7727–7736.

(*73*) Aliyah, K., Lyu, J., Goldmann, C., Bizien, T., Hamon, C., Alloyeau, D., and Constantin, D. (2020). Real-Time In Situ Observations Reveal a Double Role for Ascorbic Acid in the Anisotropic Growth of Silver on Gold. *The Journal of Physical Chemistry Letters 11*, 2830–2837.

(*74*) Zheng, H., Smith, R. K., Jun, Y. W., Kisielowski, C., Dahmen, U., and Alivisatos, A. P. (2009). Observation of single colloidal platinum nanocrystal growth trajectories. *Science 324*, 1309–1312.

(*75*) Woehl, T. J., Evans, J. E., Arslan, I., Ristenpart, W. D., and Browning, N. D. (2012). Direct in Situ Determination of the Mechanisms Controlling Nanoparticle Nucleation and Growth. *ACS Nano 6*, 8599–8610.

(*76*) Hauwiller, M. R., Frechette, L. B., Jones, M. R., Ondry, J. C., Rotskoff, G. M., Geissler, P., and Alivisatos, A. P. (2018). Unraveling Kinetically-Driven Mechanisms of Gold Nanocrystal Shape Transformations Using Graphene Liquid Cell Electron Microscopy. *Nano Letters 18*, 5731–5737.

(*77*) Hauwiller, M. R., Ondry, J. C., Chan, C. M., Khandekar, P., Yu, J., and Alivisatos, A. P. (2019). Gold Nanocrystal Etching as a Means of Probing the Dynamic Chemical Environment in Graphene Liquid Cell Electron Microscopy. *Journal of the American Chemical Society 141*, 4428–4437.

(*78*) Hauwiller, M. R., Ye, X., Jones, M. R., Chan, C. M., Calvin, J. J., Crook, M. F., Zheng, H., and Alivisatos, A. P. (2020). Tracking the Effects of Ligands on Oxidative Etching of Gold Nanorods in Graphene Liquid Cell Electron Microscopy. *ACS Nano 14*, 10239–10250.

(*79*) Ye, X., Jones, M. R., Frechette, L. B., Chen, Q., Powers, A. S., Ercius, P., Dunn, G., Rotskoff, G. M., Nguyen, S. C., Adiga, V. P., Zettl, A., Rabani, E., Geissler, P., and Alivisatos, A. P. (2016). Single-particle mapping of nonequilibrium nanocrystal transformations. *Science 354*, 874–877.

(*80*) Jiang, Y., Zhu, G., Dong, G., Lin, F., Zhang, H., Yuan, J., Zhang, Z., and Jin, C. (2017). Probing the oxidative etching induced dissolution of palladium nanocrystals in solution by liquid cell transmission electron microscopy. *Micron 97*, 22–28.

(*81*) Chen, L., Leonardi, A., Chen, J., Cao, M., Li, N., Su, D., Zhang, Q., Engel, M., and Ye, X. (2020). Imaging the kinetics of anisotropic dissolution of bimetallic core–shell nanocubes using graphene liquid cells. *Nature Communications 11*, 1–10.

(*82*) Park, J., Zettl, A., and Alivisatos, A. P. (2015). 3D structure of individual nanocrystals in solution by electron microscopy. *Science 349*, 287–290.

(*83*) Moreno-Hernandez, I. A., Crook, M. F., Ondry, J. C., and Alivisatos, A. P. (2021). Redox Mediated Control of Electrochemical Potential in Liquid Cell Electron Microscopy. *Journal of the American Chemical Society 143*, 12082–12089.

(*84*) Crook, M. F., Laube, C., Moreno-Hernandez, I. A., Kahnt, A., Zahn, S., Ondry, J. C., Liu, A., and Alivisatos, A. P. (2021). Elucidating the Role of Halides and Iron during Radiolysis-Driven Oxidative Etching of Gold Nanocrystals Using Liquid Cell Transmission Electron Microscopy and Pulse Radiolysis. *Journal of the American Chemical Society 143*, 11703–11713.

(*85*) Ambrožič, B., Prašnikar, A., Hodnik, N., Kostevšek, N., Likozar, B., Rožman, K. Ž., and Šturm, S. (2019). Controlling the radical-induced redox chemistry inside a liquid-cell TEM. *Chemical Science 10*, 8735–8743.

(*86*) Korpanty, J., Parent, L. R., and Gianneschi, N. C. (2021). Enhancing and Mitigating Radiolytic Damage to Soft Matter in Aqueous Phase Liquid-Cell Transmission Electron Microscopy in the Presence of Gold Nanoparticle Sensitizers or Isopropanol Scavengers. *Nano Letters 21*, 1141–1149.

(*87*) Moreno-Hernandez, I. A., Crook, M. F., Jamali, V., and Alivisatos, A. P. (2022). Recent advances in the study of colloidal nanocrystals enabled by in situ liquid-phase transmission electron microscopy. *MRS Bulletin 47*, 305–313.

(*88*) Dorfman, L. M. (1963). Pulse Radiolysis : Fast Reaction Studies in Radiation Chemistry. *Science 141*, 493–498.

(*89*) Egerton, R. F., *Electron Energy Loss Spectroscopy in the Electron Microscope*, 3rd ed.; Springer: New York, 2011.

(*90*) Leapman, R. In *Transmission Electron Energy Loss Spectrometry in Materials Science and The EELS Atlas*; Wiley-VCH Verlag GmbH & Co. KGaA: Weinheim, FRG, 2005, pp 49–96.

(*91*) Yang, J., Alam, S. B., Yu, L., Chan, E., and Zheng, H. (2019). Dynamic behavior of nanoscale liquids in graphene liquid cells revealed by in situ transmission electron microscopy. *Micron 116*, 22–29.

(*92*) Lim, K., Bae, Y., Jeon, S., Kim, K., Kim, B. H., Kim, J., Kang, S., Heo, T., Park, J., and Lee, W. C. (2020). A Large-Scale Array of Ordered Graphene-Sandwiched Chambers for Quantitative Liquid-Phase Transmission Electron Microscopy. *Advanced Materials 32*, 2002889.

(*93*) Jungjohann, K. L., Evans, J. E., Aguiar, J. A., Arslan, I., and Browning, N. D. (2012). Atomic-scale imaging and spectroscopy for in situ liquid scanning transmission electron microscopy. *Microscopy and Microanalysis 18*, 621–627.

(*94*) Tran, M., DePenning, R., Turner, M., and Padalkar, S. (2016). Effect of citrate ratio and temperature on gold nanoparticle size and morphology. *Materials Research Express 3*, 105027.

(*95*) Nikoobakht, B., and El-Sayed, M. A. (2003). Preparation and Growth Mechanism of Gold Nanorods (NRs) Using Seed-Mediated Growth Method. *Chemistry of Materials 15*, 1957–1962.

(*96*) Wu, H.-L., Kuo, C.-H., and Huang, M. H. (2010). Seed-Mediated Synthesis of Gold Nanocrystals with Systematic Shape Evolution from Cubic to Trisoctahedral and Rhombic Dodecahedral Structures. *Langmuir 26*, 12307–12313.

(*97*) Leff, D. V., Ohara, P. C., Heath, J. R., and Gelbart, W. M. (1995). Thermodynamic control of gold nanocrystal size: Experiment and theory. *Journal of Physical Chemistry 99*, 7036–7041.

(*98*) Smith, D. K., Miller, N. R., and Korgel, B. A. (2009). Iodide in CTAB Prevents Gold Nanorod Formation. *Langmuir 25*, 9518–9524.

(*99*) Rayavarapu, R. G., Ungureanu, C., Krystek, P., Van Leeuwen, T. G., Manohar, S., and Materials, M. (2010). Iodide Impurities in Hexadecyltrimethylammonium Bromide (CTAB) Products: Lot-Lot Variations and Influence on Gold Nanorod Synthesis. *Langmuir 26*, 5050–5055.

(*100*) Langille, M. R., Personick, M. L., Zhang, J., and Mirkin, C. A. (2012). Defining Rules for the Shape Evolution of Gold Nanoparticles. *Journal of the American Chemical Society 134*, 14542–14554.

(*101*) O'Brien, M. N., Jones, M. R., Brown, K. A., and Mirkin, C. A. (2014). Universal Noble Metal Nanoparticle Seeds Realized Through Iterative Reductive Growth and Oxidative Dissolution Reactions. *Journal of the American Chemical Society 136*, 7603–7606.

(*102*) Niu, W., Zheng, S., Wang, D., Liu, X., Li, H., Han, S., Chen, J., Tang, Z., and Xu, G. (2009). Selective Synthesis of Single-Crystalline Rhombic Dodecahedral, Octahedral, and Cubic Gold Nanocrystals. *Journal of the American Chemical Society 131*, 697–703.

(*103*) Kim, B. H. et al. (2020). Critical differences in 3D atomic structure of individual ligand-protected nanocrystals in solution. *Science 368*, 60–67.

(*104*) Hermannsdörfer, J., de Jonge, N., and Verch, A. (2015). Electron beam induced chemistry of gold nanoparticles in saline solution. *Chemical Communications 51*, 16393–16396.

(*105*) Mopper, K., and Zhout, X. (1990). Hydroxyl Radical Photoproduction in the Sea and Its Potential Impact on Marine Processes. *Science 250*, 661–664.

(*106*) Zhou, X., and Mopper, K. (1990). Determination of photochemically produced hydroxyl radicals in seawater and freshwater. *Marine Chemistry 30*, 71–88.

(*107*) Hata, K., Inoue, H., Kojima, T., Iwase, A., Kasahara, S., Hanawa, S., Ueno, F., and Tsukada, T. (2016). Hydrogen Peroxide Production by Gamma Radiolysis of Sodium Chloride Solutions Containing a Small Amount of Bromide Ion. *Nuclear Technology 193*, 434–443.

(*108*) Zhang, S., Zhang, L., Liu, K., Liu, M., Yin, Y., and Gao, C. (2018). Digestive ripening in the formation of monodisperse silver nanospheres. *Materials Chemistry Frontiers 2*, 1328–1333.

(*109*) Rafi, A., and Sutton, H. C. (1965). Radiolysis of aerated solutions of potassium bromide. *Transactions of the Faraday Society 61*, 877.

(*110*) Ward, J. F., and Myers, L. S. (1965). The Effect of Chloride Ions on Some Radiation Chemical Reactions in Aqueous Solution. *Radiation Research 26*, 483.

(*111*) Atinault, E., De Waele, V., Schmidhammer, U., Fattahi, M., and Mostafavi, M. (2008). Scavenging of e_s^- and $OH^\bullet$ radicals in concentrated HCl and NaCl aqueous solutions. *Chemical Physics Letters 460*, 461–465.

(*112*) Jayson, G. G., Parsons, B. J., and Swallow, A. J. (1973). Some simple, highly reactive, inorganic chlorine derivatives in aqueous solution. Their formation using pulses of radiation and their role in the mechanism of the Fricke dosimeter. *Journal of the Chemical Society, Faraday Transactions 1: Physical Chemistry in Condensed Phases 69*, 1597.

(*113*) Parker, K. M., and Mitch, W. A. (2016). Halogen radicals contribute to photooxidation in coastal and estuarine waters. *Proceedings of the National Academy of Sciences 113*, 5868–5873.

(*114*) Chee, S. W., Pratt, S. H., Hattar, K., Duquette, D., Ross, F. M., and Hull, R. (2015). Studying localized corrosion using liquid cell transmission electron microscopy. *Chemical Communications 51*, 168–171.

(*115*) Hauwiller, M. R., Ondry, J. C., and Alivisatos, A. P. (2018). Using Graphene Liquid Cell Transmission Electron Microscopy to Study *in situ* Nanocrystal Etching. *Journal of Visualized Experiments*, 57665.

(*116*) Long, R., Zhou, S., Wiley, B. J., and Xiong, Y. (2014). Oxidative etching for controlled synthesis of metal nanocrystals: Atomic addition and subtraction. *Chemical Society Reviews 43*, 6288–6310.

(*117*) Xiong, Y., Cai, H., Wiley, B. J., Wang, J., Kim, M. J., and Xia, Y. (2007). Synthesis and mechanistic study of palladium nanobars and nanorods. *Journal of the American Chemical Society 129*, 3665–3675.

(*118*) Guo, X., Zhang, Q., Sun, Y., Zhao, Q., and Yang, J. (2012). Lateral etching of core-shell Au@metal nanorods to metal-tipped Au nanorods with improved catalytic activity. *ACS Nano 6*, 1165–1175.

(*119*) Xia, X., Choi, S.-I., Herron, J. A., Lu, N., Scaranto, J., Peng, H.-C., Wang, J., Mavrikakis, M., Kim, M. J., and Xia, Y. (2013). Facile Synthesis of Palladium Right Bipyramids and Their Use as Seeds for Overgrowth and as Catalysts for Formic Acid Oxidation. *Journal of the American Chemical Society 135*, 15706–15709.

(*120*) Meena, S. K., Celiksoy, S., Schäfer, P., Henkel, A., Sönnichsen, C., and Sulpizi, M. (2016). The role of halide ions in the anisotropic growth of gold nanoparticles: a microscopic, atomistic perspective. *Physical Chemistry Chemical Physics 18*, 13246–13254.

(*121*) Anbar, M., and Thomas, J. K. (1964). Pulse Radiolysis Studies of Aqueous Sodium Chloride Solutions 1. *The Journal of Physical Chemistry 68*, 3829–3835.

(*122*) Wardman, P. (1989). Reduction Potentials of One-Electron Couples Involving Free Radicals in Aqueous Solution. *Journal of Physical and Chemical Reference Data 18*, 1637–1755.

(*123*) Hayon, E., Treinin, A., and Wilf, J. (1972). Electronic spectra, photochemistry, and autoxidation mechanism of the sulfite-bisulfite-pyrosulfite systems. SO_2^-, SO_3^-, SO_4^-, and SO_5^- radicals. *Journal of the American Chemical Society 94*, 47–57.

(*124*) Buxton, G. V. In *The Study of Fast Processes and Transient Species by Electron Pulse Radiolysis*, 1982, pp 241–266.

(*125*) Persson, I. (2018). Ferric Chloride Complexes in Aqueous Solution: An EXAFS Study. *Journal of Solution Chemistry 47*, 797–805.

(*126*) Sastre, S., Casasnovas, R., Muñoz, F., and Frau, J. (2016). Isodesmic reaction for accurate theoretical pK_a calculations of amino acids and peptides. *Physical Chemistry Chemical Physics 18*, 11202–11212.

(*127*) Marenich, A. V., Cramer, C. J., and Truhlar, D. G. (2009). Universal solvation model based on solute electron density and on a continuum model of the solvent defined by the bulk dielectric constant and atomic surface tensions. *Journal of Physical Chemistry B 113*, 6378–6396.

(*128*) Ho, J. (2015). Are thermodynamic cycles necessary for continuum solvent calculation of pK_as and reduction potentials? *Physical Chemistry Chemical Physics 17*, 2859–2868.

(*129*) Fielden, E. M. In *The Study of Fast Processes and Transient Species by Electron Pulse Radiolysis*; 8; Springer Netherlands: Dordrecht, 1982; Vol. 44, pp 49–62.

(*130*) Neese, F. (2012). The ORCA program system. *Wiley Interdisciplinary Reviews: Computational Molecular Science 2*, 73–78.

(*131*) Reiher, M., Salomon, O., and Hess, B. A. (2001). Reparameterization of hybrid functionals based on energy differences of states of different multiplicity. *Theoretical Chemistry Accounts 107*, 48–55.

(*132*) Kepp, K. P. (2016). Theoretical Study of Spin Crossover in 30 Iron Complexes. *Inorganic Chemistry 55*, 2717–2727.

(*133*) Weigend, F. (2006). Hartree–Fock Exchange Fitting Basis Sets for H to Rn. *Journal of computational chemistry 29*, 167–175.

(*134*) Weigend, F., and Ahlrichs, R. (2005). Balanced basis sets of split valence, triple zeta valence and quadruple zeta valence quality for H to Rn: Design and assessment of accuracy. *Physical Chemistry Chemical Physics 7*, 3297–3305.

(*135*) Grimme, S., Antony, J., Ehrlich, S., and Krieg, H. (2010). A consistent and accurate ab initio parametrization of density functional dispersion correction (DFT-D) for the 94 elements H-Pu. *The Journal of Chemical Physics 132*, 154104-1–154104-19.

(*136*) Grimme, S., Ehrlich, S., and Goerick, L. (2011). Effect of the Damping Function in Dispersion Corrected Density Functional Theory. *Journal of computational chemistry 32*, 1456–1465.

(*137*) Barone, V., Cossi, M., and Tomasi, J. (1998). Geometry optimization of molecular structures in solution by the polarizable continuum model. *Journal of Computational Chemistry 19*, 404–417.

(*138*) Herrmann, C., Reiher, M., and Hess, B. A. (2005). Comparative analysis of local spin definitions. *The Journal of Chemical Physics 122*, 034102–1–034102–10.

(*139*) Nielsen, M. H., Aloni, S., and De Yoreo, J. J. (2014). In situ TEM imaging of $CaCO_3$ nucleation reveals coexistence of direct and indirect pathways. *Science 345*, 1158–1162.

(*140*) Ou, Z., Wang, Z., Luo, B., Luijten, E., and Chen, Q. (2020). Kinetic pathways of crystallization at the nanoscale. *Nature Materials 19*, 450–455.

(*141*) Park, J., Zheng, H., Lee, W. C., Geissler, P. L., Rabani, E., and Alivisatos, A. P. (2012). Direct observation of nanoparticle superlattice formation by using liquid cell transmission electron microscopy. *ACS Nano 6*, 2078–2085.

(*142*) Cepeda-Perez, E., Doblas, D., Kraus, T., and de Jonge, N. (2020). Electron microscopy of nanoparticle superlattice formation at a solid-liquid interface in nonpolar liquids. *Science Advances 6*, 1–6.

(*143*) Yesibolati, M. N., Mortensen, K. I., Sun, H., Brostrøm, A., Tidemand-Lichtenberg, S., and Mølhave, K. (2020). Unhindered Brownian Motion of Individual Nanoparticles in Liquid-Phase Scanning Transmission Electron Microscopy. *Nano Letters 20*, 7108–7115.

(*144*) Vratsanos, M. A., and Gianneschi, N. C. (2022). Direct Observation of Emulsion Morphology, Dynamics, and Demulsification. *ACS Nano 16*, 7783–7793.

(*145*) Gnanasekaran, K., Korpanty, J., Berger, O., Hampu, N., Halperin-Sternfeld, M., Cohen-Gerassi, D., Adler-Abramovich, L., and Gianneschi, N. C. (2021). Dipeptide Nanostructure Assembly and Dynamics via in Situ Liquid-Phase Electron Microscopy. *ACS Nano 15*, 16542–16551.

(*146*) Gnanasekaran, K., Chang, H., Smeets, P. J. M., Korpanty, J., Geiger, F. M., and Gianneschi, N. C. (2020). In Situ Ni^{2+} Stain for Liposome Imaging by Liquid-Cell Transmission Electron Microscopy. *Nano Letters 20*, 4292–4297.

(*147*) Keskin, S., Pawell, C., and de Jonge, N. (2021). Verification of water presence in graphene liquid cells. *Micron*, 103109.

(*148*) Holtz, M. E., Yu, Y., Gao, J., Abruña, H. D., and Muller, D. A. (2013). In Situ Electron Energy-Loss Spectroscopy in Liquids. *Microscopy and Microanalysis 19*, 1027–1035.

(*149*) Unocic, R. R., Baggetto, L., Veith, G. M., Aguiar, J. A., Unocic, K. A., Sacci, R. L., Dudney, N. J., and More, K. L. (2015). Probing battery chemistry with liquid cell electron energy loss spectroscopy. *Chemical Communications 51*, 16377–16380.

(*150*) Jokisaari, J. R., Hachtel, J. A., Hu, X., Mukherjee, A., Wang, C., Konecna, A., Lovejoy, T. C., Dellby, N., Aizpurua, J., Krivanek, O. L., Idrobo, J.-C., and Klie, R. F. (2018). Vibrational Spectroscopy of Water with High Spatial Resolution. *Advanced Materials 30*, 1802702.

(*151*) Khestanova, E., Guinea, F., Fumagalli, L., Geim, A. K., and Grigorieva, I. V. (2016). Universal shape and pressure inside bubbles appearing in van der Waals heterostructures. *Nature Communications 7*, 1–10.

(*152*) Vasu, K. S., Prestat, E., Abraham, J., DIx, J., Kashtiban, R. J., Beheshtian, J., Sloan, J., Carbone, P., Neek-Amal, M., Haigh, S. J., Geim, A. K., and Nair, R. R. (2016). Van der Waals pressure and its effect on trapped interlayer molecules. *Nature Communications 7*, 1–6.

(*153*) Lim, C. H. Y. X., Nesladek, M., and Loh, K. P. (2014). Observing high-pressure chemistry in graphene bubbles. *Angewandte Chemie - International Edition 53*, 215–219.

(*154*) Karnatak, R. C., Esteva, J. M., Dexpert, H., Gasgnier, M., Caro, P. E., and Albert, L. (1987). X-ray absorption studies of CeO_2, PrO_2, and TbO_2. I. Manifestation of localized and extended f states in the 3d absorption spectra. *Physical Review B 36*, 1745–1749.

(*155*) Löble, M. W. et al. (2015). Covalency in lanthanides. An X-ray absorption spectroscopy and density functional theory study of $LnCl_6^{x-}$ (x = 3, 2). *Journal of the American Chemical Society 137*, 2506–2523.

(*156*) Tsvirko, M., and Svetashev, A. (2011). Raman spectroscopic study of trivalent lanthanides in concentrated aqueous solutions. *Journal of Physics: Conference Series 289*, 012012.

(*157*) El Omar, A. K., Schmidhammer, U., Rousseau, B., Laverne, J., and Mostafavi, M. (2012). Competition reactions of $H_2O^{\bullet+}$ radical in concentrated Cl^- aqueous solutions: Picosecond pulse radiolysis study. *Journal of Physical Chemistry A 116*, 11509–11518.

(*158*) LaVerne, J. A., and Tandon, L. (2005). H_2 and Cl_2 production in the radiolysis of calcium and magnesium chlorides and hydroxides. *Journal of Physical Chemistry A 109*, 2861–2865.

(*159*) Schwarz, H. A. (1955). The Effect of Solutes on the Molecular Yields in the Radiolysis of Aqueous Solutions. *Journal of the American Chemical Society 77*, 4960–4964.

(*160*) Pastina, B., Laverne, J. A., and Pimblott, S. M. (1999). Dependence of Molecular Hydrogen Formation in Water on Scavengers of the Precursor to the Hydrated Electron. *Journal of Physical Chemistry A 103*, 5841–5846.

(*161*) Kestin, J., Khalifa, H. E., and Correia, R. J. (1981). Tables of the dynamic and kinematic viscosity of aqueous NaCl solutions in the temperature range 20–150 °C and the pressure range 0.1–35 MPa. *Journal of Physical and Chemical Reference Data 10*, 71–88.

(*162*) NIST ESTAR Program.

(*163*) Bjergbakke, E., Navaratnam, S., Parsons, B. J., and Swallow, A. J. (1981). Reaction between hydroperoxo radicals and chlorine in aqueous solution. *Journal of the American Chemical Society 103*, 5926–5928.

(*164*) Zehavi, D., and Rabani, J. (1972). Oxidation of aqueous bromide ions by hydroxyl radicals. A Pulse radiolytic investigation. *The Journal of Physical Chemistry 76*, 312–319.

(*165*) Merenyi, G., and Lind, J. (1994). Reaction Mechanism of Hydrogen Abstraction by the Bromine Atom in Water. *Journal of the American Chemical Society 116*, 7872–7876.

(*166*) Kläning, U. K., and Wolff, T. (1985). Laser Flash Photolysis of HClO, ClO^-, HBrO, and BrO^- in Aqueous Solution. Reactions of Cl^- and Br^- Atoms. *Berichte der Bunsengesellschaft für physikalische Chemie 89*, 243–245.

(*167*) Ershov, B. G., Kelm, M., Janata, E., Gordeev, A. V., and Bohnert, E. (2002). Radiation-chemical effects in the near-field of a final disposal site: role of bromine on the radiolytic processes in NaCl-solutions. *Radiochimica Acta 90*, 617–622.

(*168*) Matthew, B. M., and Anastasio, C. (2006). A chemical probe technique for the determination of reactive halogen species in aqueous solution: Part 1 – bromide solutions. *Atmospheric Chemistry and Physics 6*, 2423–2437.

(*169*) Sutton, H. C., and Downes, M. T. (1972). Reactions of the HO_2 radical in aqueous solution with bromine and related compounds. *Journal of the Chemical Society, Faraday Transactions 1: Physical Chemistry in Condensed Phases 68*, 1498–1507.

(*170*) Sutton, H., Adams, G., Boag, J., and Michael, B. In *International Symposium on Pulse Radiolysis*; Academic Press: Manchester, England, 1965, pp 61–81.

(*171*) Buxton, G. V., and Mulazzani, Q. G. (2007). On the hydrolysis of iodine in alkaline solution: A radiation chemical study. *Radiation Physics and Chemistry 76*, 932–940.

(*172*) Ishigure, K., Shiraishi, H., and Okuda, H. (1988). Radiation chemistry of aqueous iodine systems under nuclear reactor accident conditions. *International Journal of Radiation Applications and Instrumentation. Part C. Radiation Physics and Chemistry 32*, 593–597.

(*173*) Schwarz, H. A., and Bielski, B. H. J. (1986). Reactions of hydroperoxo and superoxide with iodine and bromine and the iodide (I_2^-) and iodine atom reduction potentials. *The Journal of Physical Chemistry 90*, 1445–1448.

(*174*) Malato, S., Fernández-Ibáñez, P., Maldonado, M., Blanco, J., and Gernjak, W. (2009). Decontamination and disinfection of water by solar photocatalysis: Recent overview and trends. *Catalysis Today 147*, 1–59.

(*175*) Jonah, C. D., Miller, J. R., and Matheson, M. S. (1977). The reaction of the precursor of the hydrated electron with electron scavengers. *The Journal of Physical Chemistry 81*, 1618–1622.

(*176*) Dainton, F. S., Holt, B. J., Philipson, N. A., and Pilling, M. J. (1976). Reactions of hydrogen atoms in 6 mol dm^{-3} sulphuric acid. Part 2.—The transition from activation to diffusion control. *Journal of the Chemical Society, Faraday Transactions 1: Physical Chemistry in Condensed Phases 72*, 257–267.

(*177*) Sehested, K., Bjergbakke, E., Rasmussen, O. L., and Fricke, H. (1969). Reactions of H_2O_3 in the Pulse-Irradiated Fe(II)-O_2 System. *Journal of Chemical Physics 51*, 3159–3166.

(*178*) Stuglik, Z., and PawełZagórski, Z. (1981). Pulse radiolysis of neutral iron(II) solutions: oxidation of ferrous ions by OH radicals. *Radiation Physics and Chemistry 17*, 229–233.

(*179*) Gogolev, A. V., Shilov, V. P., Fedoseev, A. M., and Pikaev, A. K. (1991). The study of reactivity of actinide ions towards hydrated electrons and hydrogen atoms in acid aqueous solutions by a pulse radiolysis method. *International Journal of Radiation Applications and Instrumentation. Part 37*, 531–535.

(*180*) Ribeiro, A. R., Mukherjee, A., Hu, X., Shafien, S., Ghodsi, R., He, K., Gemini-Piperni, S., Wang, C., Klie, R. F., Shokuhfar, T., Shahbazian-Yassar, R., Borojevic, R., Rocha, L. A., and Granjeiro, J. M. (2017). Bio-camouflage of anatase nanoparticles explored by: In situ high-resolution electron microscopy. *Nanoscale 9*, 10684–10693.

(*181*) Zhu, C., Liang, S., Song, E., Zhou, Y., Wang, W., Shan, F., Shi, Y., Hao, C., Yin, K., Zhang, T., Liu, J., Zheng, H., and Sun, L. (2018). In-situ liquid cell transmission electron microscopy investigation on oriented attachment of gold nanoparticles. *Nature Communications 9*, 1–7.

(*182*) Keskin, S., and de Jonge, N. (2018). Reduced Radiation Damage in Transmission Electron Microscopy of Proteins in Graphene Liquid Cells. *Nano Letters 18*, 7435–7440.

(*183*) Kang, S. et al. (2021). Real-space imaging of nanoparticle transport and interaction dynamics by graphene liquid cell TEM. *Science Advances 7*, 1–11.

(*184*) Wang, L., Chen, J., Cox, S. J., Liu, L., Sosso, G. C., Li, N., Gao, P., Michaelides, A., Wang, E., and Bai, X. (2021). Microscopic Kinetics Pathway of Salt Crystallization in Graphene Nanocapillaries. *Physical Review Letters 126*, 136001.

(*185*) Dachraoui, W., Keller, D., Henninen, T. R., Ashton, O. J., and Erni, R. (2021). Atomic Mechanisms of Nanocrystallization via Cluster-Clouds in Solution Studied by Liquid-Phase Scanning Transmission Electron Microscopy. *Nano Letters 21*, 2861–2869.

(*186*) Yuk, J. M., Seo, H. K., Choi, J. W., and Lee, J. Y. (2014). Anisotropic lithiation onset in silicon nanoparticle anode revealed by in situ graphene liquid cell electron microscopy. *ACS Nano 8*, 7478–7485.

(*187*) Chang, J. H., Cheong, J. Y., Yuk, J. M., Kim, C., Kim, S. J., Seo, H. K., Kim, I. D., and Lee, J. Y. (2017). Direct realization of complete conversion and agglomeration dynamics of SnO_2 nanoparticles in liquid electrolyte. *ACS Omega 2*, 6329–6336.

(*188*) Kim, S. J., Dae, K. S., Park, J. Y., Lee, J. Y., and Yuk, J. M. (2017). Hollow Ag_2S nanosphere formation via electron beam-assisted oxidative etching of Ag nanoparticles. *Chemical Communications 53*, 11122–11125.

(*189*) Cheong, J. Y., Chang, J. H., Kim, S. J., Kim, C., Seo, H. K., Shin, J. W., Yuk, J. M., Lee, J. Y., and Kim, I. D. (2017). In Situ High-Resolution Transmission Electron Microscopy (TEM) Observation of Sn Nanoparticles on SnO_2 Nanotubes under Lithiation. *Microscopy and Microanalysis 23*, 1107–1115.

(*190*) Yang, J., Koo, J., Kim, S., Jeon, S., Choi, B. K., Kwon, S., Kim, J., Kim, B. H., Lee, W. C., Lee, W. B., Lee, H., Hyeon, T., Ercius, P., and Park, J. (2019). Amorphous-Phase-Mediated Crystallization of Ni Nanocrystals Revealed by High-Resolution Liquid-Phase Electron Microscopy. *Journal of the American Chemical Society 141*, 763–768.

(*191*) Hirokawa, S., Teshima, H., Solís-Fernández, P., Ago, H., Li, Q.-Y., and Takahashi, K. (2021). Pinning in a Contact and Noncontact Manner: Direct Observation of a Three-Phase Contact Line Using Graphene Liquid Cells. *Langmuir 37*, 12271–12277.

(*192*) Zhou, W., Yin, K., Wang, C., Zhang, Y., Xu, T., Borisevich, A., Sun, L., Idrobo, J. C., Chisholm, M. F., Pantelides, S. T., Klie, R. F., and Lupini, A. R. (2015). The observation of square ice in graphene questioned. *Nature 528*, E1–E2.

(*193*) Algara-Siller, G., Lehtinen, O., Wang, F. C., Nair, R. R., Kaiser, U., Wu, H. A., Geim, A. K., and Grigorieva, I. V. (2015). Square ice in graphene nanocapillaries. *Nature 519*, 443–445.

Appendix A

Supplementary Information

A.1 Chapter 2 Supplementary Figures

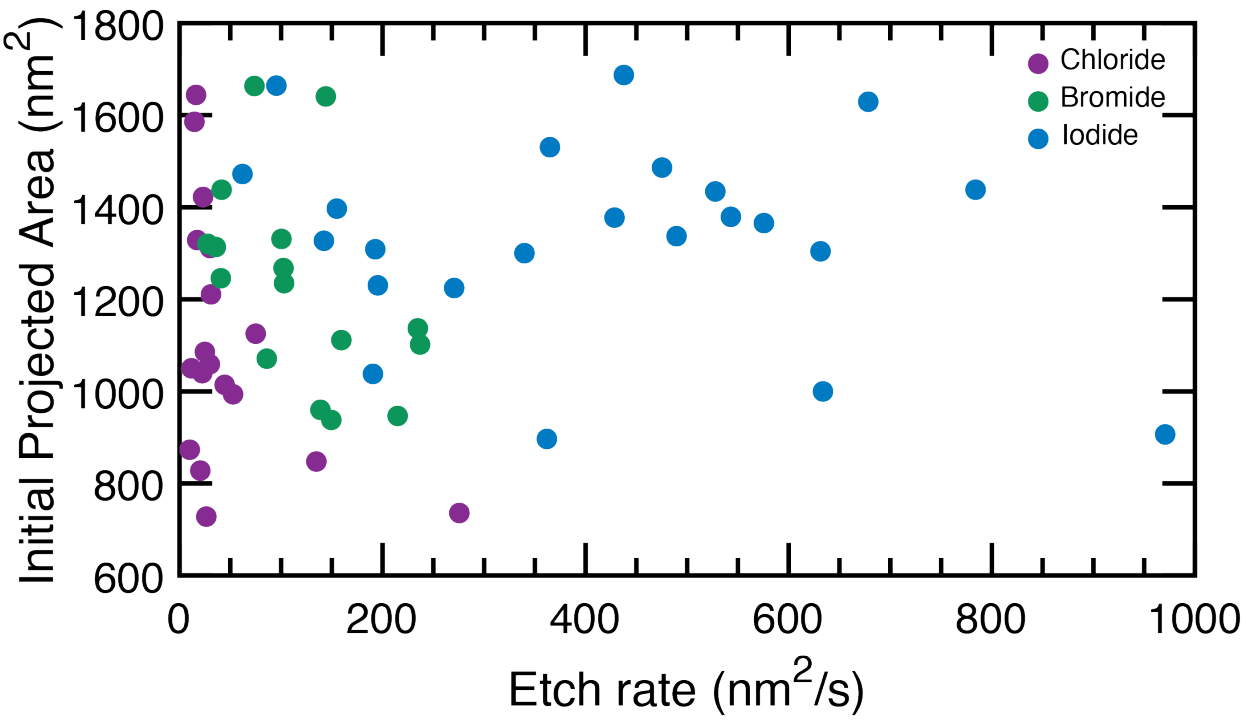

Figure A.1.1: Comparison of initial projected area and etch rate for nanocrystals in solution with 190mM Cl^- and 40mM Fe^{3+} (purple), 190mM Cl^-, 0.38mM Br^- and 40mM Fe^{3+} (green), and 190mM Cl^-, 0.38mM I^- and 40mM Fe^{3+} (blue). There is not a strong dependence between initial size and etch rate in these experiments. The average initial size and standard deviation for the chloride, bromide, and iodide environments are 1104 nm^2 $\pm$ 269 nm^2, 1232 nm^2 $\pm$ 221 nm^2, and 1336 nm^2 $\pm$ 216 nm^2, respectively.

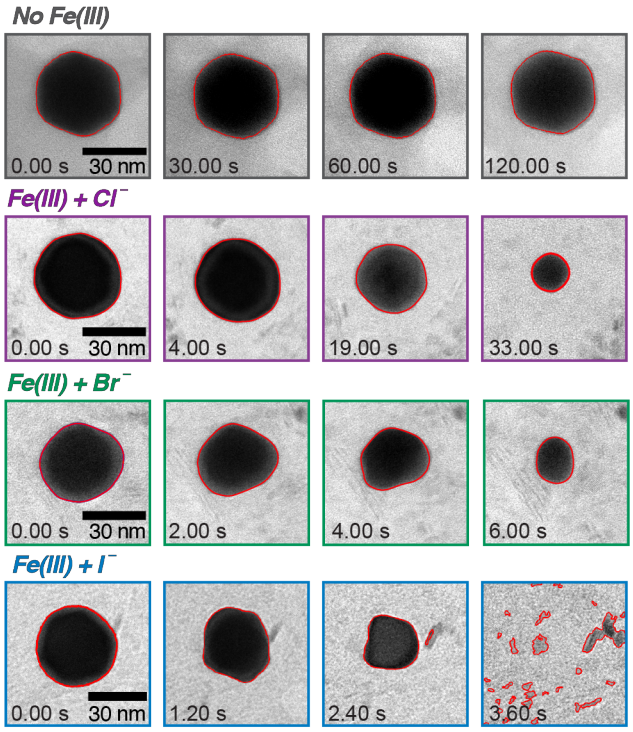

Figure A.1.2: Segmentation used to calculate circularity of each nanocrystal. The perimeters are relatively smooth, decreasing error due to noise of the outline. However, as the nanocrystals near the very end of their etching trajectories, the contrast becomes very low, and the segmentation becomes less reliable. As the error in segmentation increases near the very end of the etching trajectories, the circularity increases, which is likely the cause of in the increase in circularity at the end of all the nanocrystal etching trajectories, and a circularity greater than 1 at the end of the etching trajectory for the nanocrystals in the chloride environment.

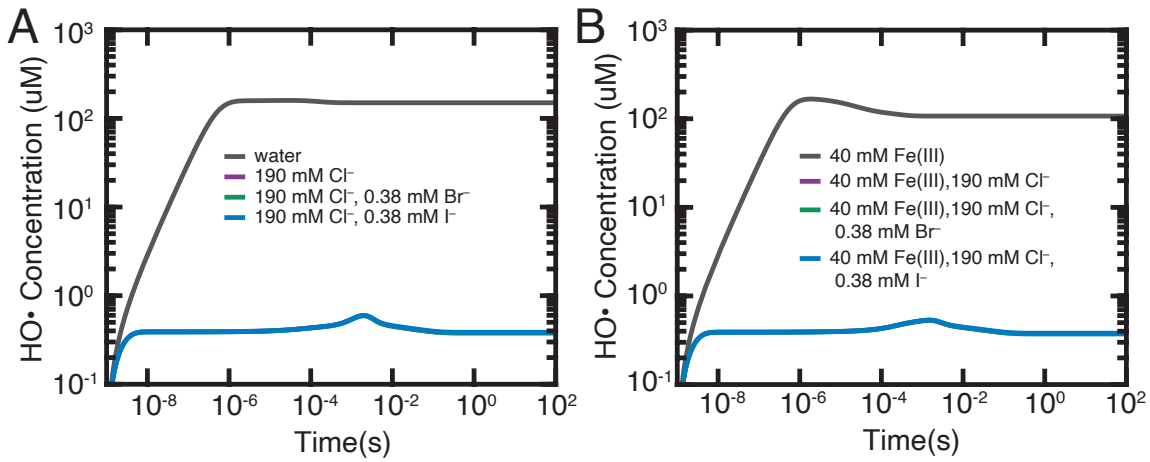

Figure A.1.3: Simulated steady state concentration of •OH radicals under various halide conditions. a) •OH radical concentration in neat water (grey), and with 190 mM Cl^- (purple), 190 mM Cl^- and 0.38 mM Br^- (green), and 190 mM Cl^- and 0.38 mM I^- (blue). b) •OH radical concentration under the four experimental concentrations tested. 40 mM Fe^{3+} (grey), 40 mM Fe^{3+} and 190 mM Cl^- (purple), 40 mM Fe^{3+}, 190 mM Cl^- and 0.38 mM Br^- (green), and 40 mM Fe^{3+}, 190 mM Cl^- and 0.38 mM I^- (blue). Chloride, bromide, and iodide solutions are overlapped in both a) and b).

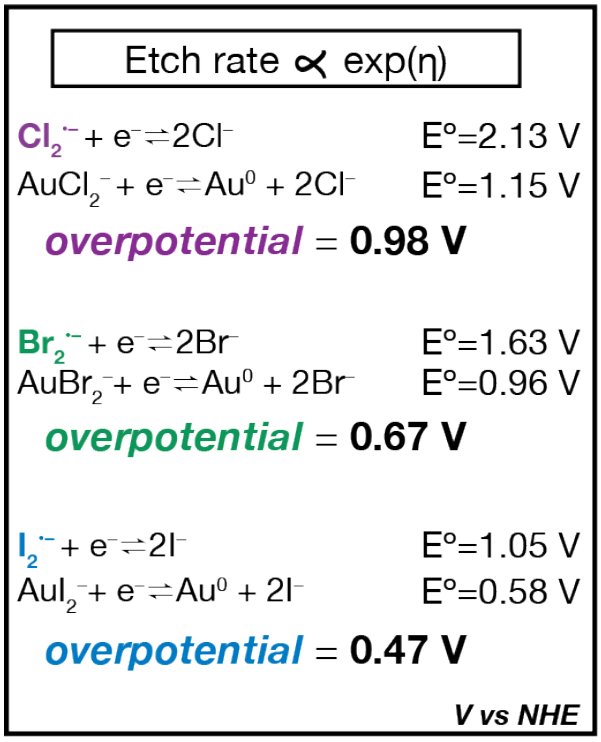

Figure A.1.4: Overpotential (η) when halides act as oxidant and complexation agent. The overpotential for etching decreases moving down group 17. If this were the predominating mechanism, a decrease in etch rate would be observed as the overpotential is proportional to the exponential of etch rate in a high driving force regime.

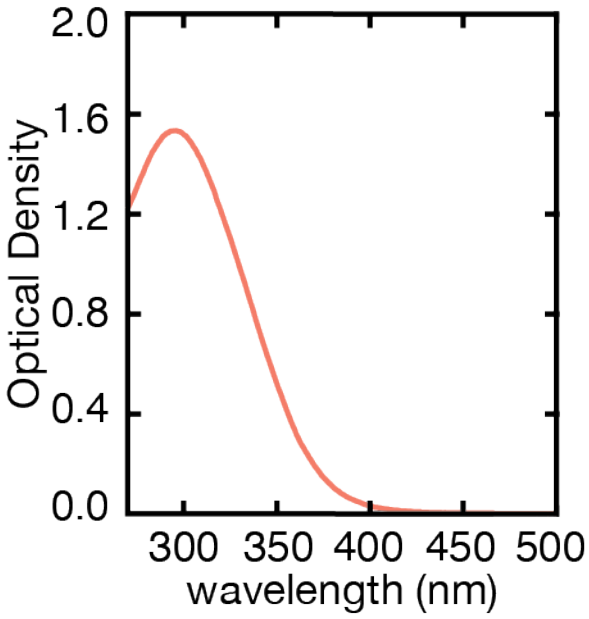

Figure A.1.5: Optical density of the 1 mM $FeCl_3$ in 0.2M HCl solution used in the pulse radiolysis studies. Note the strong absorbance in the 290-360 nm wavelength range, where the ground state bleaching in the pulse radiolysis studies is observed.

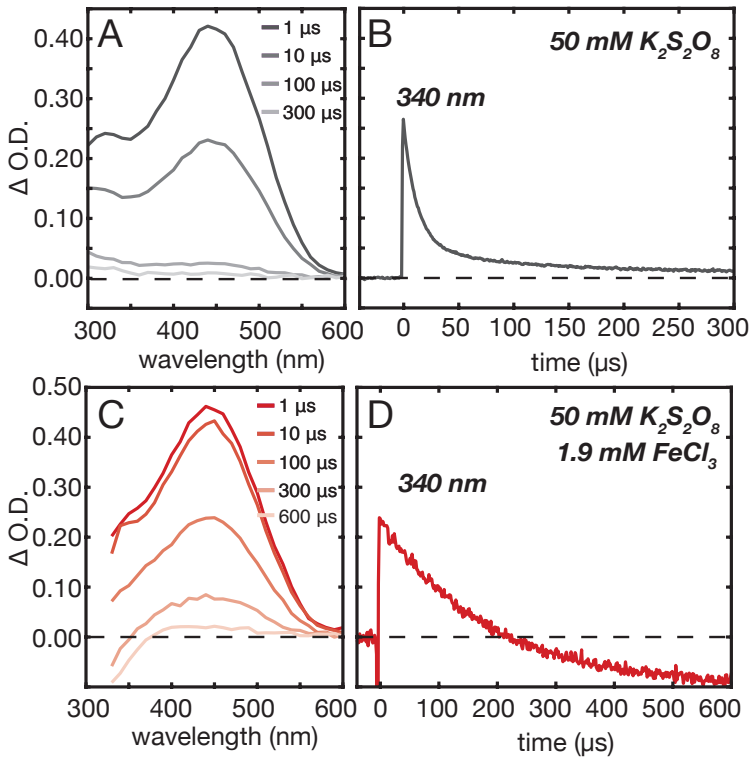

Figure A.1.6: a) Pulse radiolysis measurement (85 Gy/pulse, 15ns FWHM) of an N_2 saturated aqueous solution containing 50 mM potassium persulfate and 5 Vol% t-BuOH b) Corresponding time absorption profile at 340 nm. c) Pulse radiolysis measurement (85 Gy/pulse, 15 ns FWHM) of an N_2 saturated aqueous solution containing 50 mM potassium persulfate, 1.9 mM $Fe(NO_3)_3$ and 5 Vol% t-BuOH. d) Corresponding time absorption profile at 340 nm

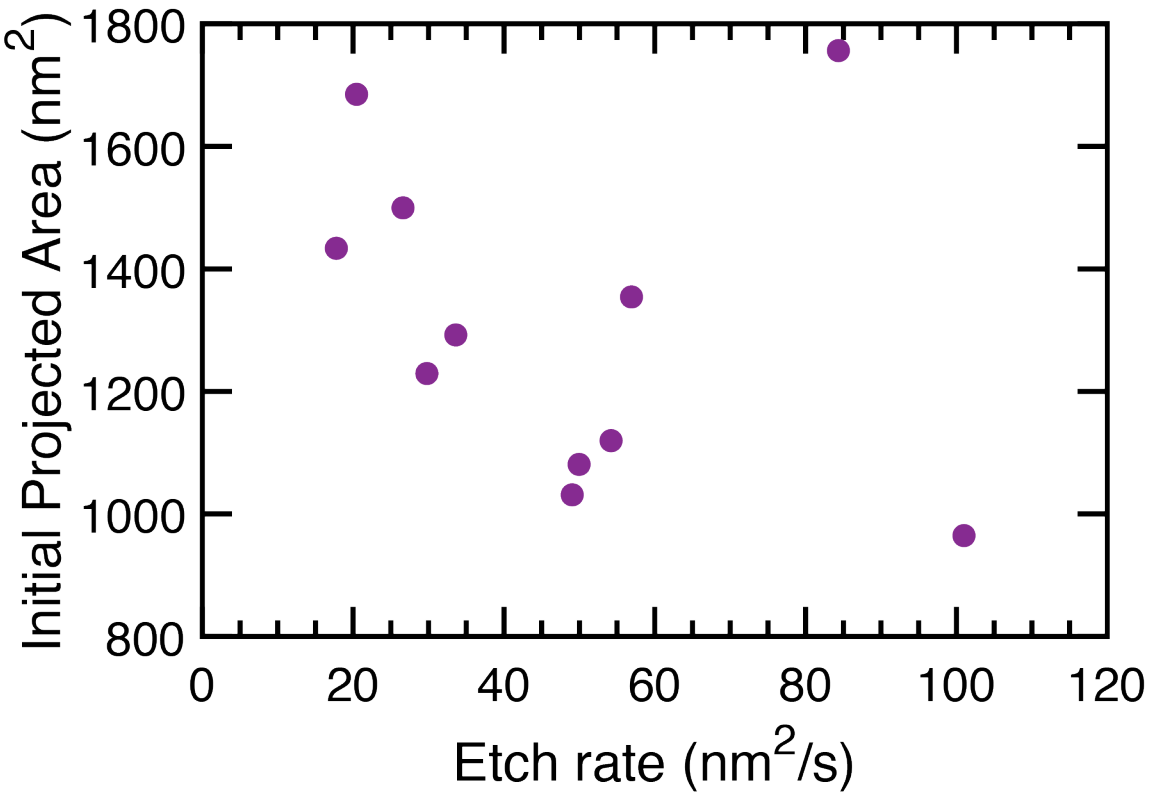

Figure A.1.7: Comparison of initial projected area and initial etch rate at 800 $e^{-}Å^{-2}s^{-1}$ for nanocrystals in solution with 190mM Cl^{-} and 40mM Fe^{3+} for the dose decrease experiments in Figure 2.5.There is not a strong correlation between initial size and etch rate. The average initial projected area for these nanocrystals is 1313 nm^2 ± 262 nm^2

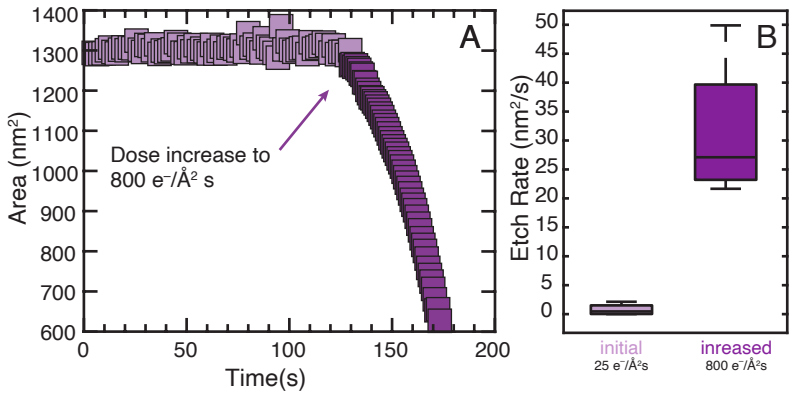

Figure A.1.8: Increase of etch rate during controls shown in Figure2.5b. During the control, the was held at 25 $e^{-}Å^{-2}s^{-1}$ for 1-2 minutes. To confirm that the nanocrystals used for the control experiments were in liquid, and lack of etching was not due to a dry pocket, the electron flux was increased to 800 $e^{-}Å^{-2}s^{-1}$ after 1-2 minutes. The onset of etching after the dose increase confirms that the nanocrystals were in solution. a) Etching trajectory of a gold nanocrystal initially irradiated at 25 $e^{-}Å^{-2}s^{-1}$. The electron flux was increased to 800 $e^{-}Å^{-2}s^{-1}$ after 130 s and the gold nanocrystal began to etch. b) Box and whisker plot summarizing the control etching trajectories under these conditions. The average etch rate of the AuNCs after increasing the electron flux significantly increases the etch rate.

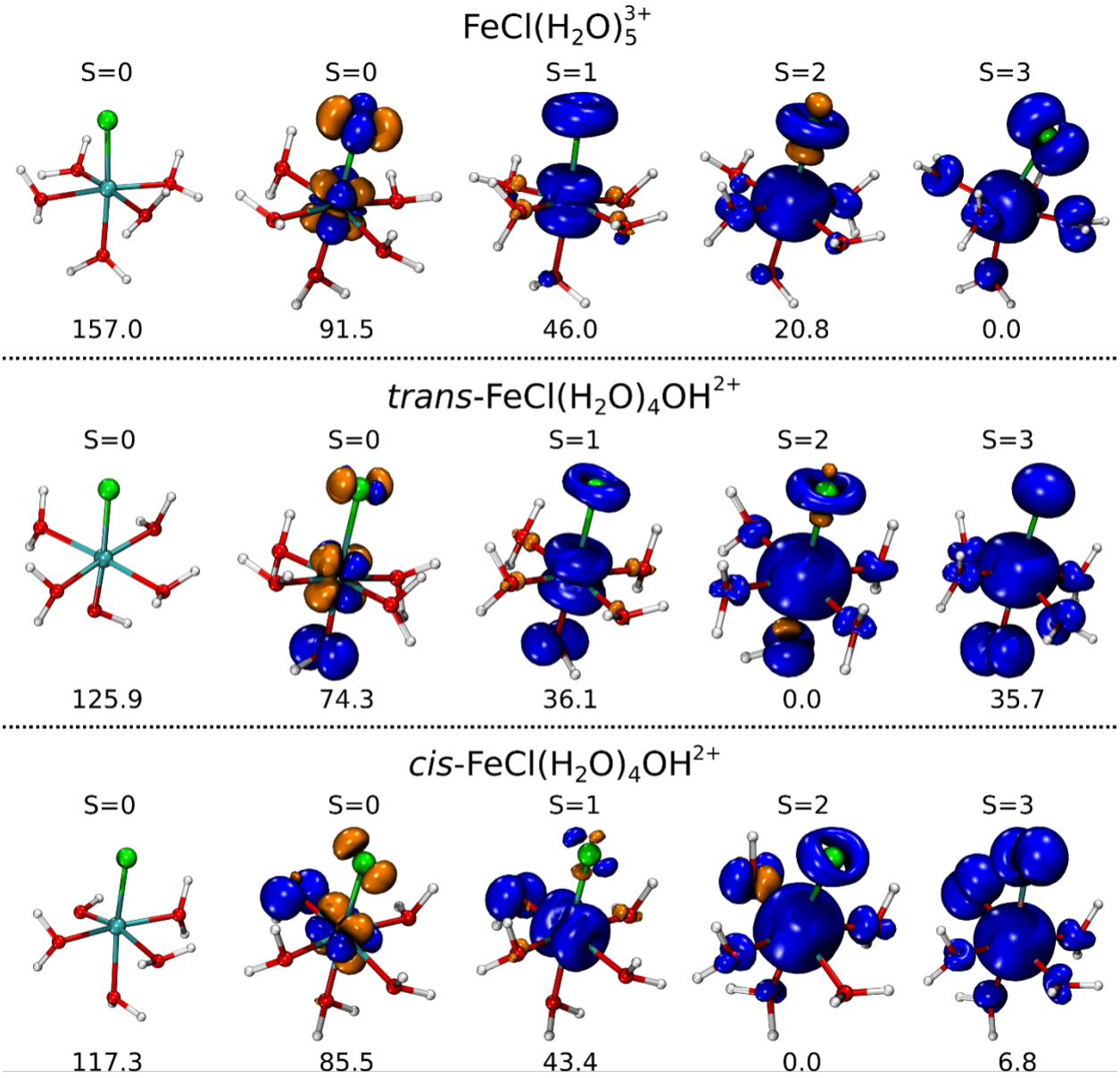

Figure A.1.9: Spin density of each Fe-complex with one Cl-atom and up to one OH group as ligand. The blue isosurface highlights regions of increased α spin density while orange are regions of increased β spin density. On top of each complex is shown the total spin S of the system while the Gibbs free energy is given below each complex. All energies are given in kJ/mol and the most stable electronic structure of each isomer was set to 0 kJ/mol.

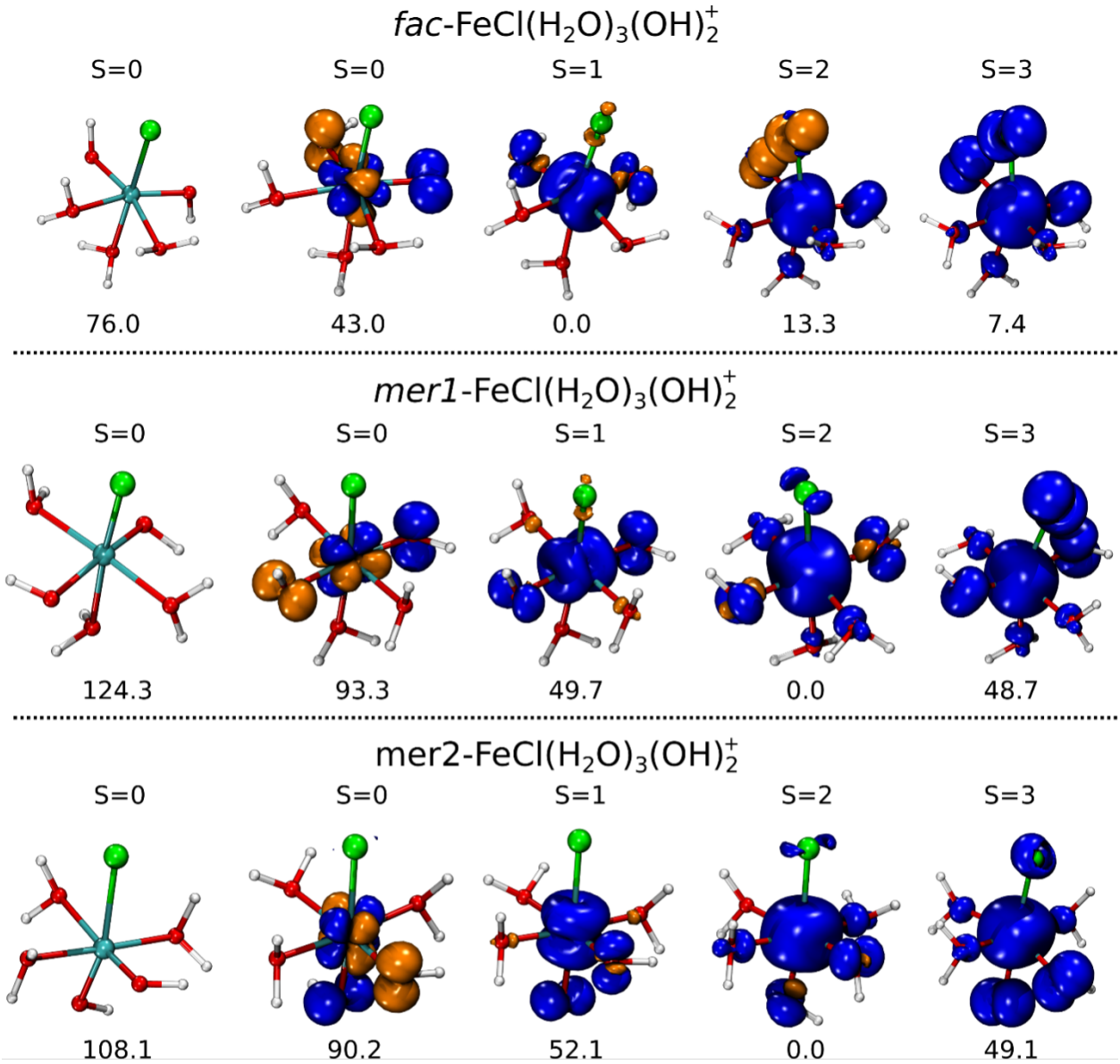

Figure A.1.10: Spin density of each Fe-complex with one Cl-atom and two OH groups as ligands. The blue isosurface highlights regions of increased α spin density while orange are regions of increased β spin density. On top of each complex is shown the total spin S of the system while the Gibbs free energy is given below each complex. All energies are given in kJ/mol and the most stable electronic structure of each isomer was set to 0 kJ/mol.

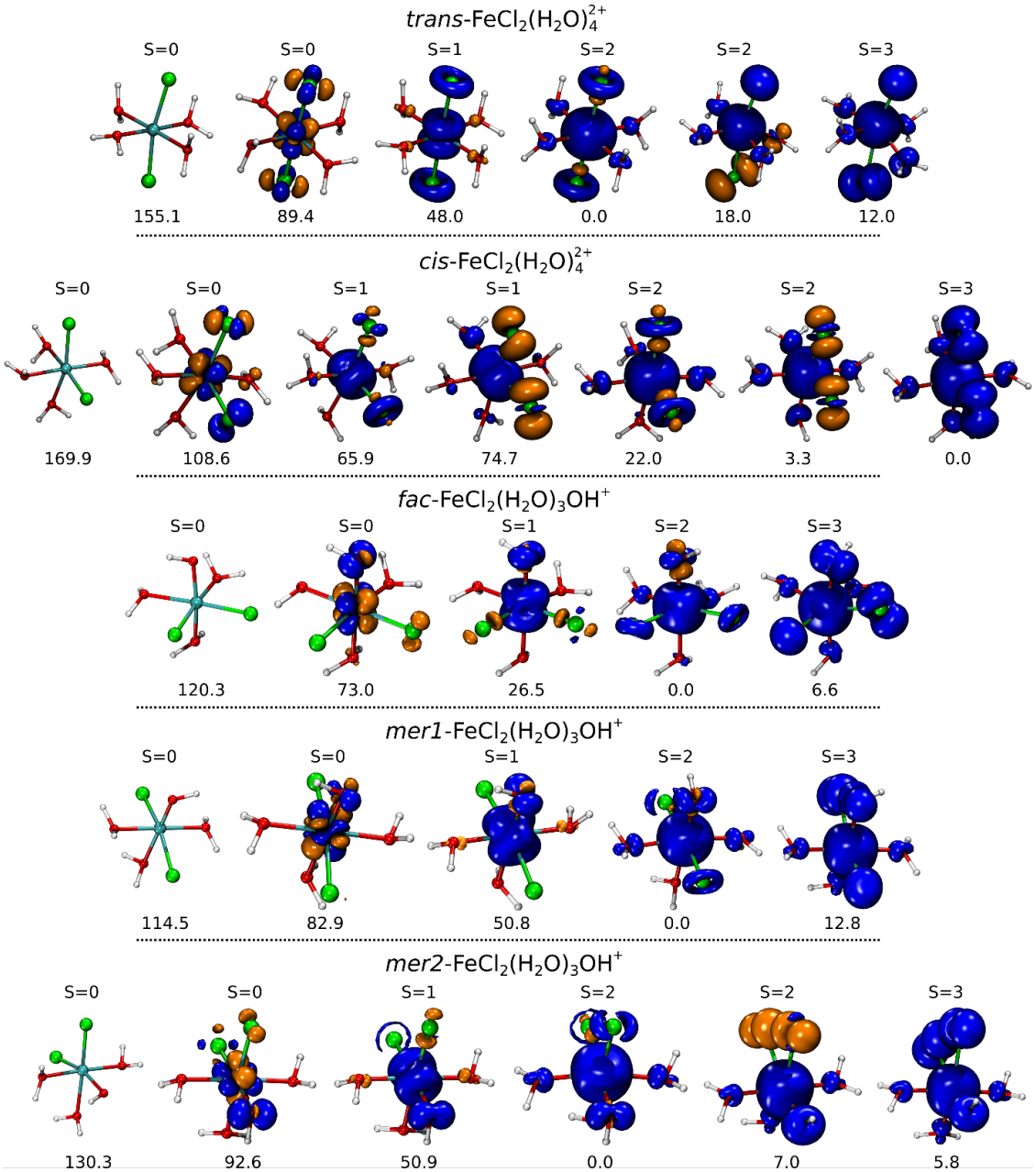

Figure A.1.11: Spin density of each Fe-complex with two Cl-atoms and up to one OH group as ligand. Blue areas indicate regions of increased α spin density while orange highlights regions of increased β spin density. On top of each complex is shown the total spin S of the system while the Gibbs free energy is given below each complex. All energies are given in kJ/mol and the most stable electronic structure was set to 0 kJ/mol for each isomer.

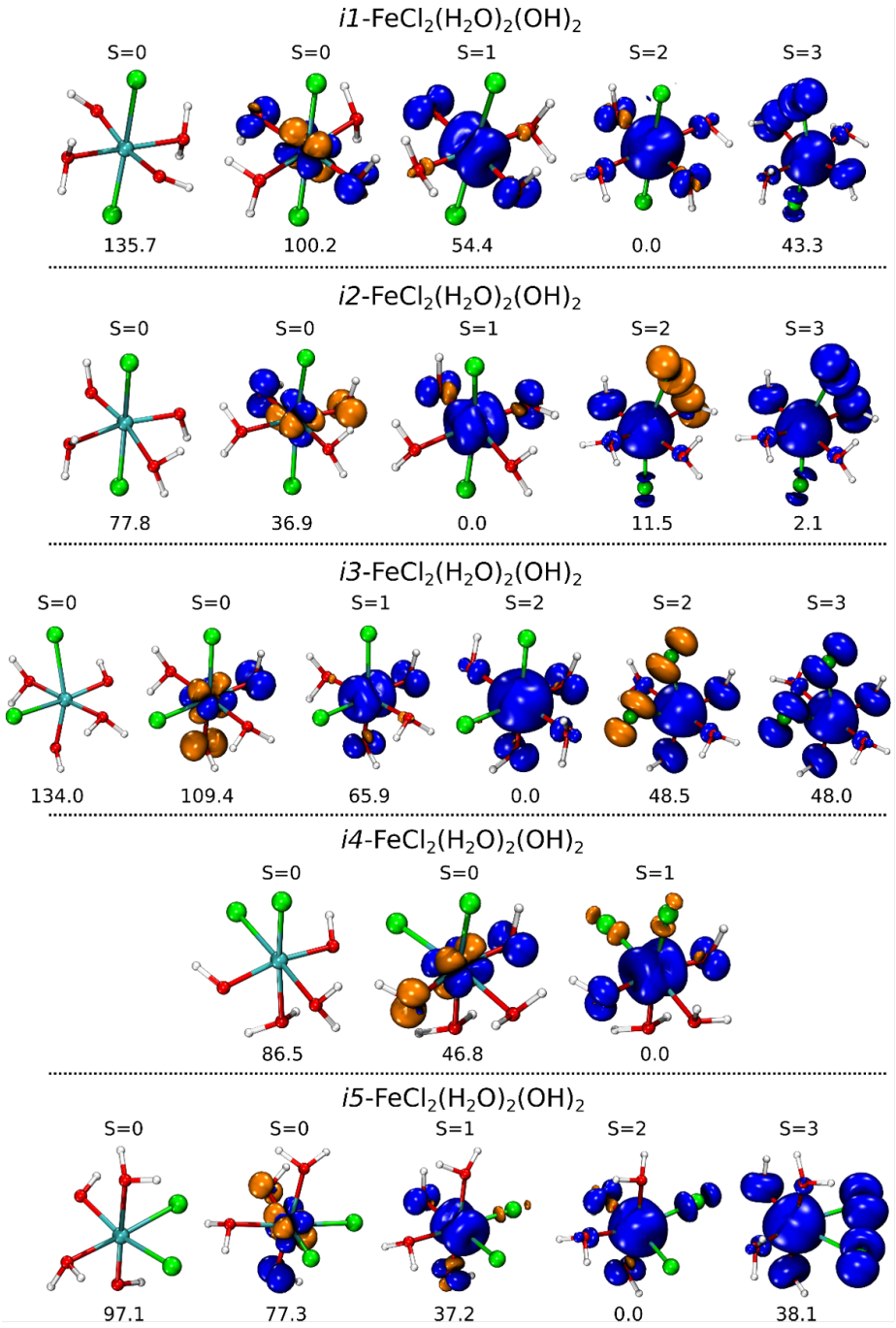

Figure A.1.12: Spin density of each Fe-complex with two Cl-atoms and two OH-groups as ligand. Blue areas indicate regions of increased α spin density while orange highlights regions of increased β spin density. On top of each complex is shown the total spin S of the system while the Gibbs free energy is given below each complex. All energies are given in kJ/mol and the most stable electronic structure was set to 0 kJ/mol for each isomer.

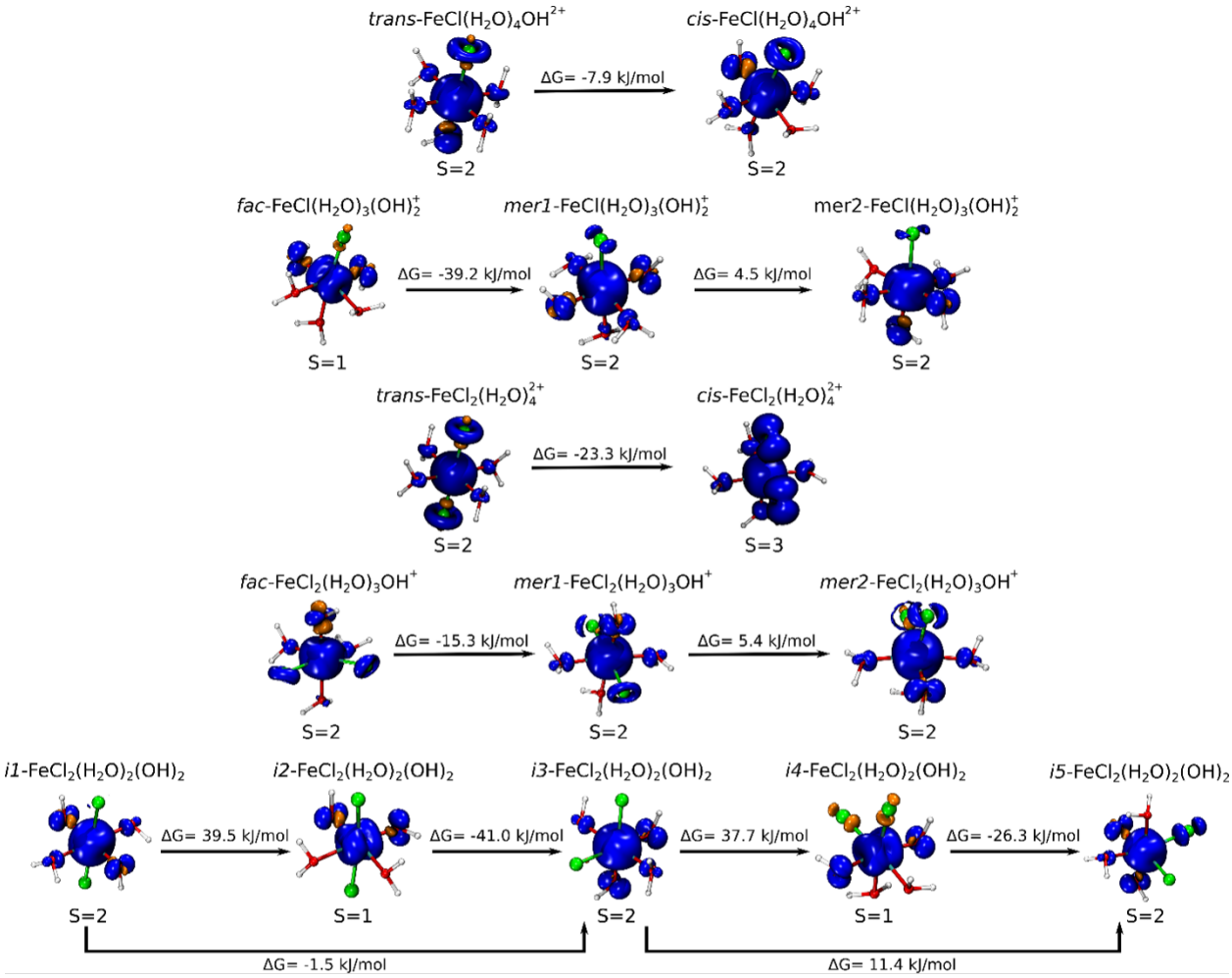

Figure A.1.13: Comparison of the stability of isomers of the Fe-complexes. Only the most stable electronic structure is compared. Isosurfaces highlight the spin density of each Fe-complex. Blue areas indicate regions of increased α spin density while orange highlights regions of increased β spin density. Bottom of each complex is shown the total spin S of the system.

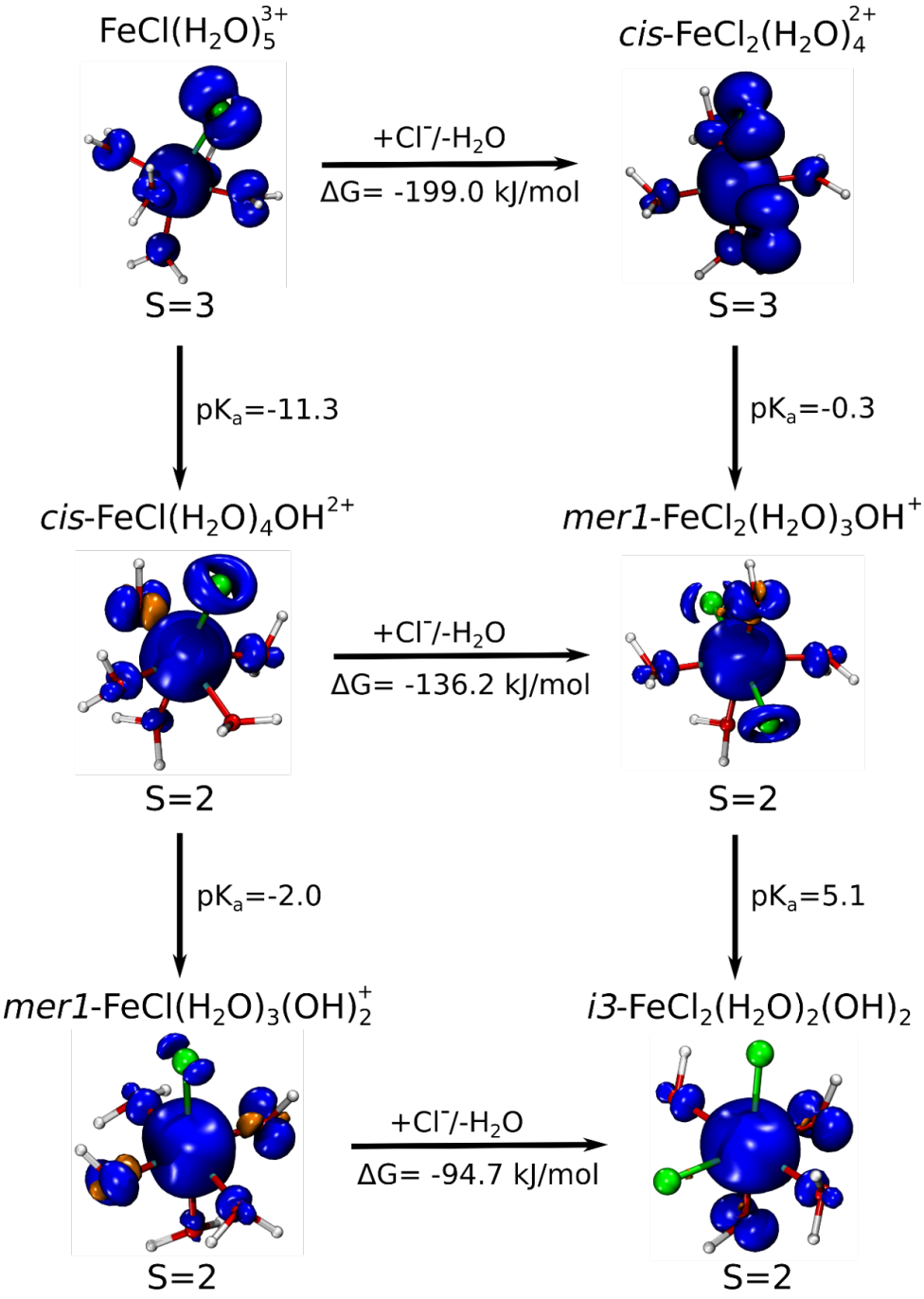

Figure A.1.14: Spin density of each Fe-complex for the most stable isomer and electronic structure. Blue areas indicate regions of increased α spin density while orange highlights regions of increased β spin density. Furthermore, pK_a values and free reaction enthalpy ΔG for exchange of a water ligand by a chloride anion.

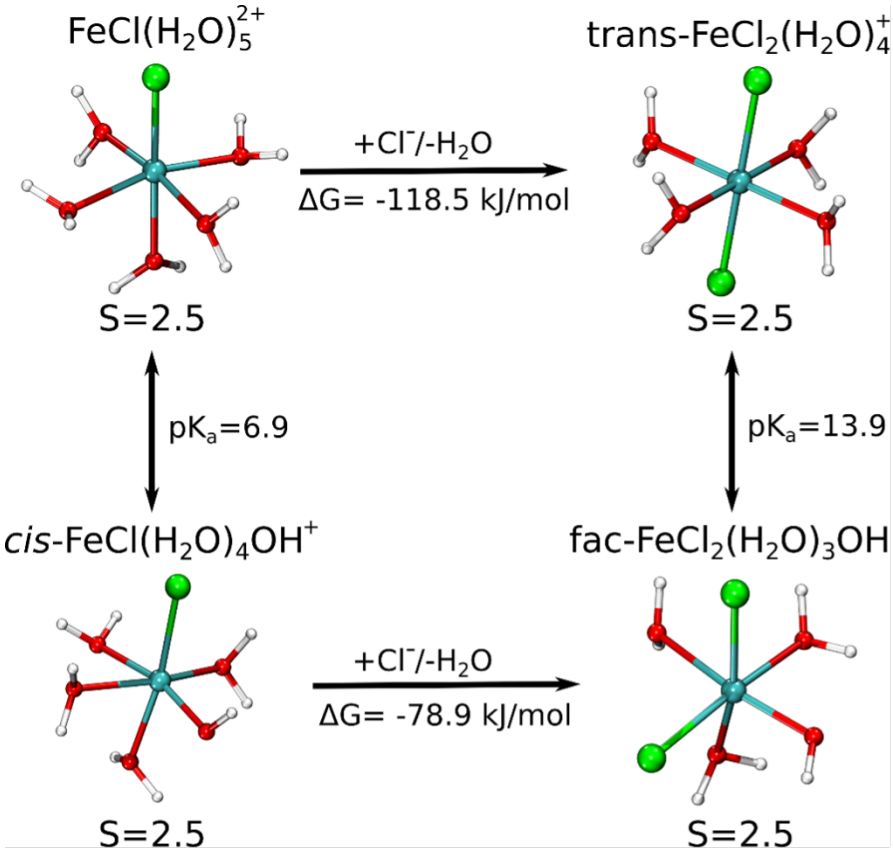

Figure A.1.15: Comparison of the stability of isomers of the Fe^{3+}-complex before the oxidation. Only the most stable electronic structure is compared. Furthermore, pK_a values and free reaction enthalpy ΔG for exchange of a water ligand by a chloride anion.

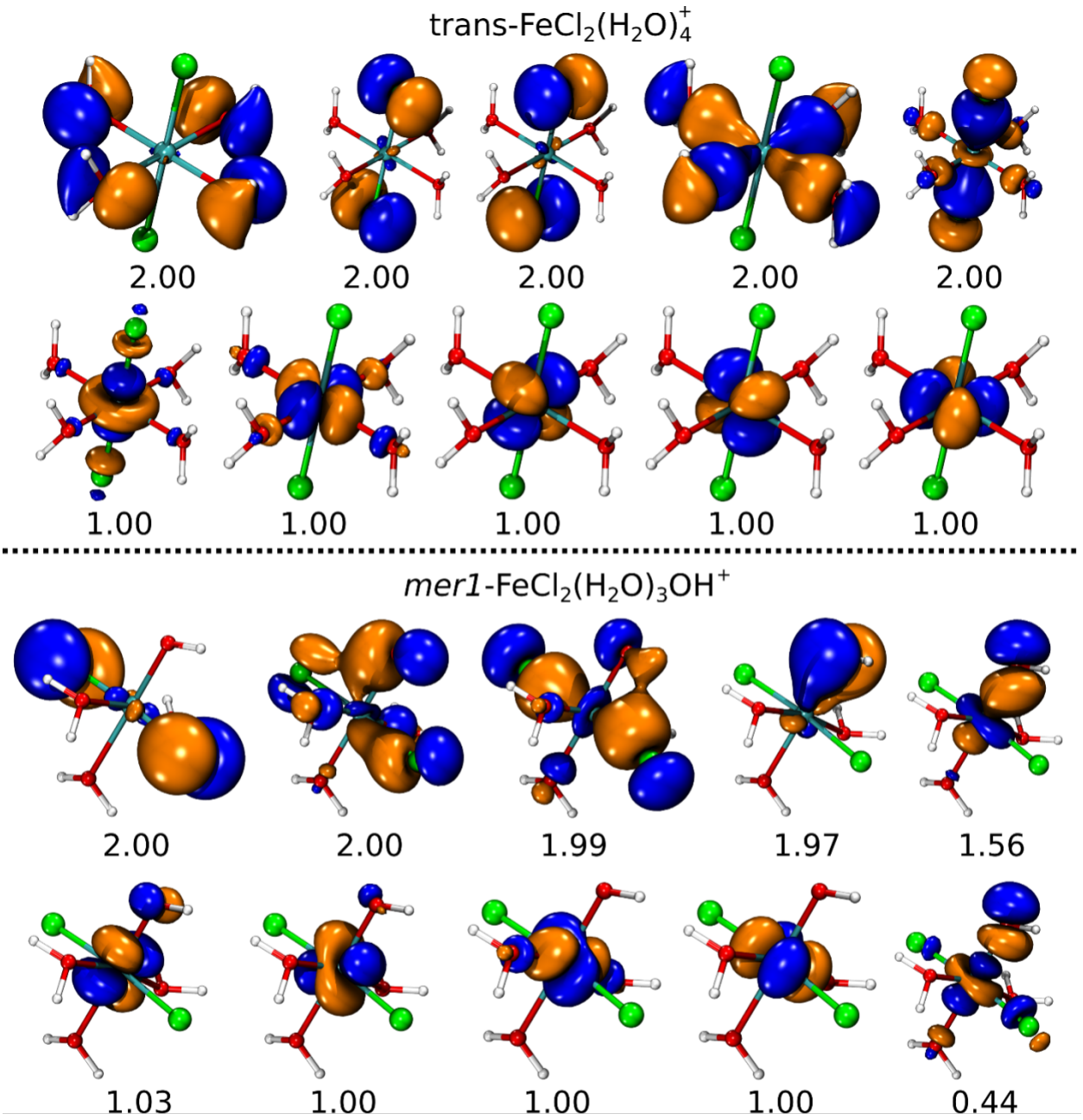

Figure A.1.16: Natural orbitals and occupation numbers of the CASSCF calculations of $[\text{trans-FeCl}_2(\text{H}_2\text{O})_4]^+$ (top, S=2.5, CASSCF(15,10)) and mer1-$[\text{FeCl}_2(\text{H}_2\text{O})_3\text{OH}^+]$ (bottom, S=2, CASSCF(14,10))

A.2 Chapter 2 Supplementary Tables

Table A.1: Summary of Cl Chemical Reactions Included in Radiolysis Chemical Network Model

No.	Reaction	Rate Constant ($M^{-1}s^{-1}$ or s^{-1})	Reference
74	$HO^{\bullet} + Cl^{-} \longrightarrow ClOH^{\bullet -}$	4.3×10^{9}	El Omar et al.[157]
75	$ClOH^{\bullet -} \longrightarrow OH^{\bullet} + Cl^{-}$	6.1×10^{9}	El Omar et al.[157]
76	$Cl^{\bullet} + Cl^{-} \longrightarrow Cl_2^{\bullet -}$	8.5×10^{9}	El Omar et al.[157]
77	$H^{+} + ClOH^{\bullet -} \longrightarrow Cl^{\bullet} + H_2O$	2.1×10^{10}	El Omar et al.[157]
78	$ClOH^{\bullet -} \longrightarrow Cl^{\bullet} + OH^{-}$	2.3×10^{1}	El Omar et al.[157]
79	$Cl^{\bullet} + OH^{-} \longrightarrow ClOH^{\bullet -}$	1.8×10^{10}	El Omar et al.[157]
80	$Cl_2^{\bullet -} \longrightarrow Cl^{\bullet} + Cl^{-}$	6.0×10^{4}	El Omar et al.[157]
81	$Cl_2^{\bullet -} + Cl_2^{\bullet -} \longrightarrow Cl_3^{-} + Cl^{-}$	2.0×10^{9}	El Omar et al.[157]
82	$Cl^{\bullet} + Cl_2^{\bullet -} \longrightarrow Cl_3^{-}$	6.3×10^{8}	El Omar et al.[157]
83	$Cl^{-} + Cl_2 \longrightarrow Cl_3^{-}$	1.0×10^{4}	El Omar et al.[157]
84	$Cl_3^{-} \longrightarrow Cl^{-} + Cl_2$	5.0×10^{4}	El Omar et al.[157]
85	$Cl^{\bullet} + Cl^{\bullet} \longrightarrow Cl_2$	8.8×10^{7}	El Omar et al.[157]
86	$e_{aq}^{-} + Cl^{\bullet} \longrightarrow Cl^{-}$	1.0×10^{10}	El Omar et al.[157]
87	$e_{aq}^{-} + Cl_2^{\bullet -} \longrightarrow 2Cl^{-}$	1.0×10^{10}	El Omar et al.[157]
88	$e_{aq}^{-} + Cl_3^{-} \longrightarrow Cl^{-} + Cl_2^{\bullet -}$	3.0×10^{10}	El Omar et al.[157]
89	$H^{\bullet} + Cl^{\bullet} \longrightarrow H^{+} + Cl^{-}$	1.0×10^{10}	El Omar et al.[157]
90	$H^{\bullet} + Cl_2^{\bullet -} \longrightarrow H^{+} + Cl^{-}$	8.0×10^{9}	El Omar et al.[157]
91	$H^{\bullet} + Cl_3^{-} \longrightarrow H^{+} + Cl^{-} + Cl_2^{\bullet -}$	1.0×10^{10}	El Omar et al.[157]
92	$HO_2^{\bullet} + Cl_2^{\bullet -} \longrightarrow 2Cl^{-} + O_2 + H^{+}$	1.0×10^{9}	El Omar et al.[157]
93	$HO_2^{\bullet} + Cl_2 \longrightarrow Cl_2^{\bullet -} + O_2 + H^{+}$	1.0×10^{9}	Bjergbakke et al.[163]
94	$H_2O_2 + Cl_2^{\bullet -} \longrightarrow HO_2^{\bullet} + 2Cl^{-} + H^{+}$	1.4×10^{5}	El Omar et al.[157]

95	$H_2O_2 + Cl^\bullet \longrightarrow HO_2^\bullet + Cl^- + H^+$	2×10^9	El Omar et al.[157]

Table A.2: Summary of Br Chemical Reactions Included in Radiolysis Chemical Network Model

No.	Reaction	Rate Constant ($M^{-1}s^{-1}$ or s^{-1})	Reference
96	$HO^\bullet + Br^- \longrightarrow BrOH^{\bullet-}$	1.1×10^{10}	Zehavi, and Rabani[164]
97	$BrOH^{\bullet-} \longrightarrow OH^\bullet + Br^-$	3.3×10^7	Zehavi, and Rabani[164]
98	$Br^\bullet + Br^- \longrightarrow Br_2^{\bullet-}$	1.2×10^{10}	Merenyi, and Lind[165]
99	$Br_2^{\bullet-} \longrightarrow Br^\bullet + Br^-$	1.9×10^4	Merenyi, and Lind[165]
100	$BrOH^{\bullet-} + H^+ \longrightarrow Br^\bullet + H_2O$	4.4×10^{10}	Zehavi, and Rabani[164]
101	$Br^\bullet + OH^- \longrightarrow BrOH^{\bullet-}$	1.3×10^{10}	Kläning, and Wolff[166]
102	$Br_2^{\bullet-} + H^\bullet \longrightarrow H^+ + 2Cl^-$	1.4×10^4	Hata et al.[107]
103	$Br_2^{\bullet-} + e_{aq}^- \longrightarrow 2Br^-$	1.1×10^10	Hata et al.[107]
104	$Br_3^- + H^\bullet \longrightarrow H^+Br_2^{\bullet-} + Br^-$	1.2×10^10	Hata et al.[107]
105	$Br_3^- + e_{aq}^- \longrightarrow Br_2^{\bullet-} + Br^-$	2.7×10^{10}	Hata et al.[107]
106	$Br_2^- + Br^- \longrightarrow Br_3^-$	9.6×10^8	Ershov et al.[167]
107	$Br_3^- \longrightarrow Br_2 + Br^-$	5.5×10^7	Ershov et al.[167]
108	$Br_2^{\bullet-} + H_2O_2 \longrightarrow 2Br^- + HO_2^\bullet + H^+$	5.0×10^2	Matthew, and Anastasio[168]
109	$BrOH^{\bullet-} \longrightarrow Br^\bullet + OH^-$	4.2×10^6	Zehavi, and Rabani[164]
110	$Br_2 + HO_2^\bullet \longrightarrow Br_2^{\bullet-} + H^+ + O_2$	1.1×10^8	Sutton, and Downes[169]

111	$Br_2^{\bullet-} + HO_2^{\bullet} \longrightarrow H^+ + 2Br^- + O_2$	4.6×10^9	Sutton et al.[170]

Table A.3: Summary of I Chemical Reactions Included in Radiolysis Chemical Network Model

No.	Reaction	Rate Constant ($M^{-1}s^{-1}$, $M^{-2}s^{-1}$, or s^{-1})	Reference
112	$HO^{\bullet} + I^- \longrightarrow IOH^{\bullet-}$	1.6×10^{10}	Buxton, and Mulazzani[171]
113	$I^- + I^{\bullet} \longrightarrow I_2^{\bullet-}$	9.1×10^9	Buxton, and Mulazzani[171]
114	$I_2^{\bullet-} + I^{\bullet} \longrightarrow I_3^{\bullet-}$	6.5×10^9	Buxton, and Mulazzani[171]
115	$I_3^- + e_{aq}^- \longrightarrow I_2^{\bullet-} + I^-$	3.5×10^{10}	Buxton, and Mulazzani[171]
116	$2I_2^{\bullet-} \longrightarrow I^- + I_3^-$	2.5×10^9	Buxton, and Mulazzani[171]
117	$I_2^{\bullet-} + H^{\bullet} \longrightarrow 2I^- + H^+$	1.8×10^7	Buxton, and Mulazzani[171]
118	$I_2 + H^{\bullet} \longrightarrow H^+ + I_2^{\bullet-}$	3.5×10^{10}	Buxton, and Mulazzani[171]
119	$I_3^- + H^{\bullet} \longrightarrow H^+ + I_2^{\bullet-} + I^-$	3.5×10^{10}	Buxton, and Mulazzani[171]
120	$I_2^{\bullet-} + HO_2^{\bullet} \longrightarrow I_2 + HO_2^-$	4.0×10^9	Ishigure et al.[172]
121	$2I^{\bullet} \longrightarrow I_2$	1.1×10^{10}	Buxton, and Mulazzani[171]
122	$I_3^- + O_2^{\bullet-} \longrightarrow O_2 + I_2^{\bullet-} + I^-$	2.5×10^8	Buxton, and Mulazzani[171]
123	$I_2 + HO_2^{\bullet} \longrightarrow I_2^{\bullet-} + H^+ + O_2$	1.8×10^7	Schwarz, and Bielski[173]

124	$I^{\bullet} + OH^{-} \longrightarrow IOH^{\bullet -}$	1.6×10^{8}	Buxton, and Mulazzani[171]
125	$IOH^{\bullet -} \longrightarrow I^{\bullet} + OH^{-}$	3.5×10^{7}	Buxton, and Mulazzani[171]
126	$I_2 + e_{aq}^{-} \longrightarrow I_2^{\bullet -}$	5.1×10^{10}	Buxton, and Mulazzani[171]
127	$I^{-} + O_2^{\bullet -} + H_2O \longrightarrow IOH^{\bullet -} + OH^{-}$	2.9×10^{9}	Buxton, and Mulazzani[171]

Table A.4: Summary of Fe Chemical Reactions Included in Radiolysis Chemical Network Model

No.	Reaction	Rate Constant ($M^{-1}s^{-1}$)	Reference
128	$Fe^{2+} + H_2O_2 \longrightarrow Fe^{3+} + HO^{\bullet} + OH^{-}$	60	Malato et al.[174]
129	$Fe^{3+} + e_{aq}^{-} \longrightarrow Fe^{2+}$	6×10^{10}	Jonah et al.[175]
130	$H^{\bullet} + Fe^{3+} \longrightarrow H^{+} + Fe^{2+}$	7.0×10^{5}	Dainton et al.[176]
131	$HO_2^{\bullet -} + Fe^{3+} \longrightarrow H^{+} + O_2 + Fe^{2+}$	2.1×10^{5}	Sehested et al.[177]
132	$Fe^{2+} + HO^{\bullet} \longrightarrow Fe^{3+} + OH^{-}$	3.1×10^{8}	Stuglik, and PawełZagórski[178]

A.3 Chapter 3 Supplementary Figures

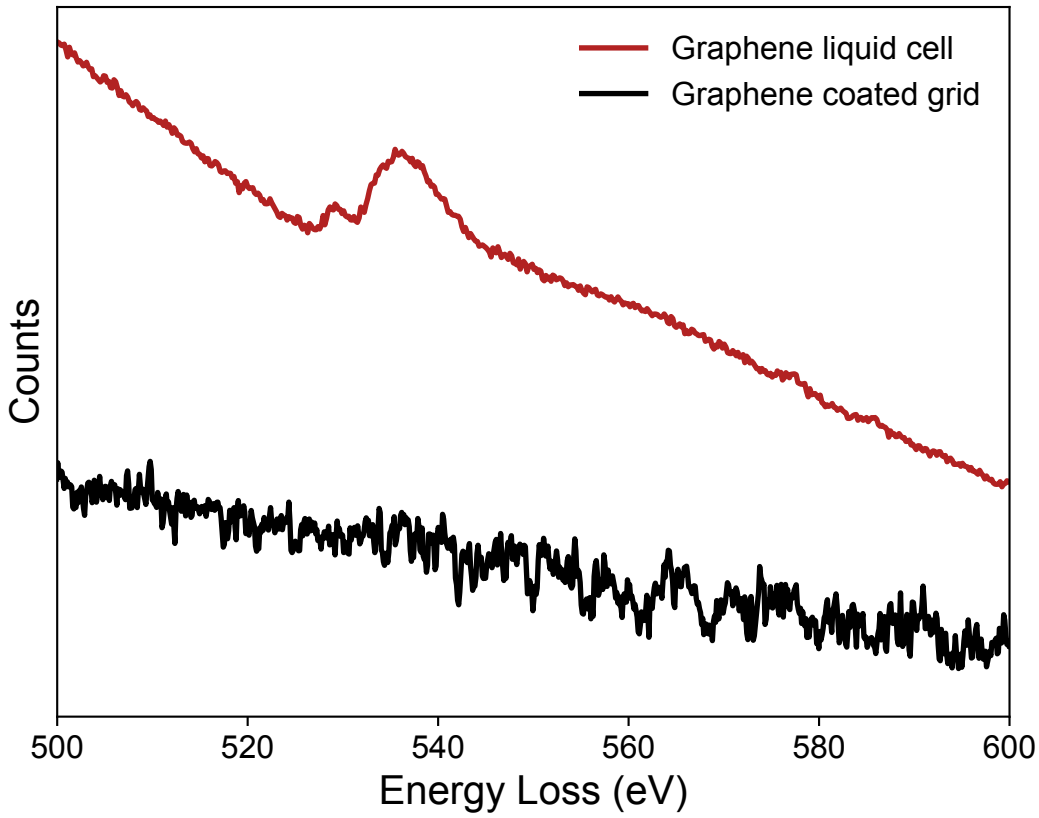

Figure A.3.1: Oxygen K-edge on a graphene coated grid (black) and of a graphene liquid cell (maroon) used in this study.

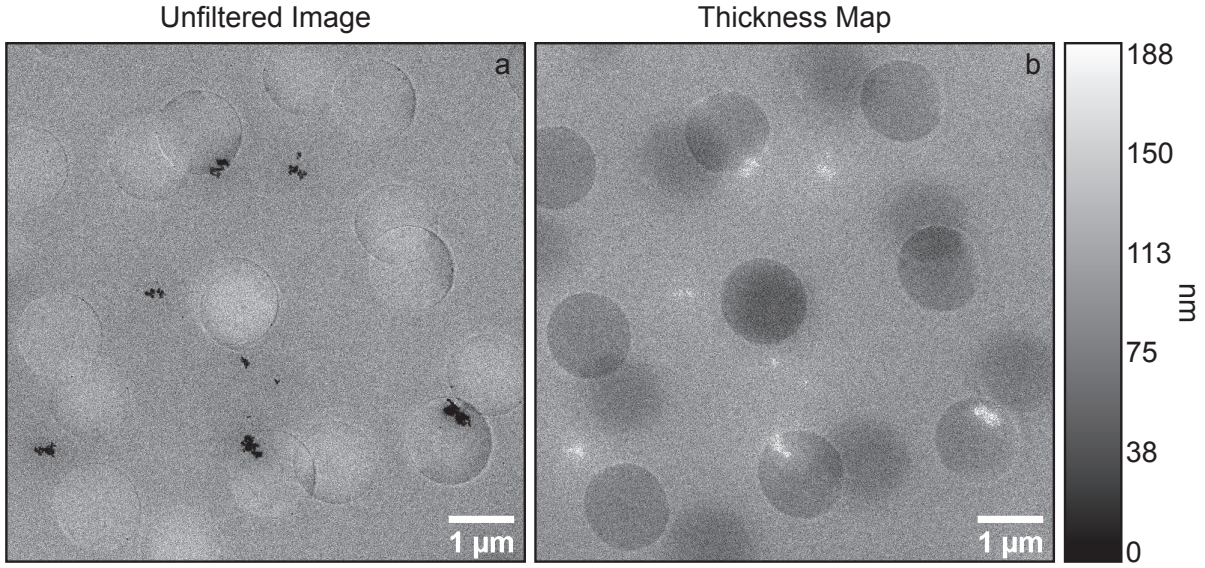

Figure A.3.2: a) Low magnification TEM image and b) thickness map of a graphene liquid cell prepared with 40 mM $CeCl_3$. The thickness of the graphene liquid cell is relatively uniform across the displayed region, and thinner in the graphene coated holes of the holey carbon grid. Thickness was calculated assuming the solution was $CeCl_3 \bullet 7H_2O$. It is important to note that EELS, EDS, and Raman data indicate that the concentration of the solution changes from region to region, which would affect the inelastic mean free path and the thickness measurements.

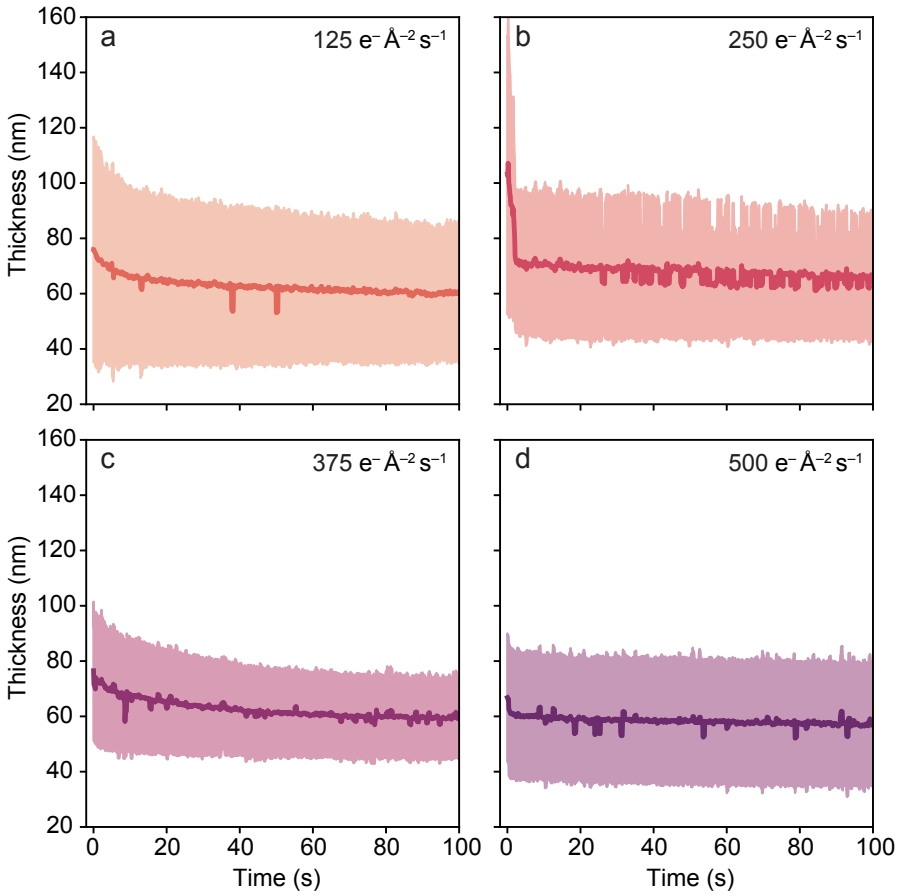

Figure A.3.3: Time dependent thickness measurements of the graphene liquid cells at a) 125 b) 250 c) 375 and d) 500 $e^{-}Å^{-2}s^{-1}$. The dark curve is the average and the shaded region is the standard deviation. Thickness was calculated assuming the solution was $CeCl_3 \bullet 7H_2O$. It is important to note that EELS, EDS, and Raman data indicate that the concentration of the solution changes from region to region, which would affect the inelastic mean free path and the thickness measurements.

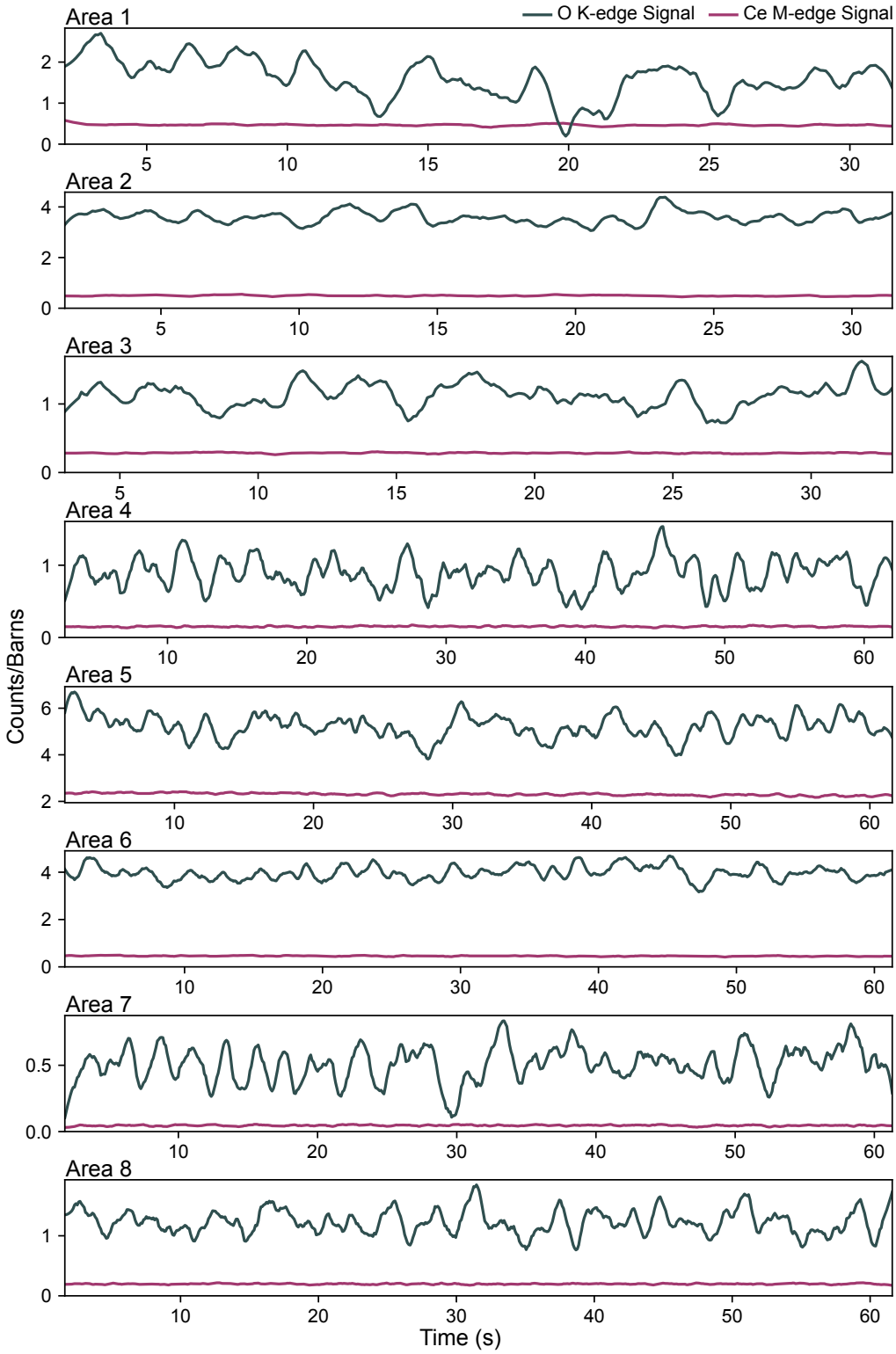
O K-edge Signal
Ce M-edge Signal
Area 1
Area 2
Area 3
Area 4
Area 5
Area 6
Area 7
Area 8
Counts/Barns
Time (s)

Figure A.3.4: Time resolved oxygen K-edge and cerium M-edge signals, taking into account their respective cross sections, on eight separate areas of a graphene liquid cell prepared with 40 mM $CeCl_3$. Although the oxygen signal varies throughout irradiation, which has been described previously,[93] there is not a net decrease in the signal in these regions, which would indicate loss of solvent.

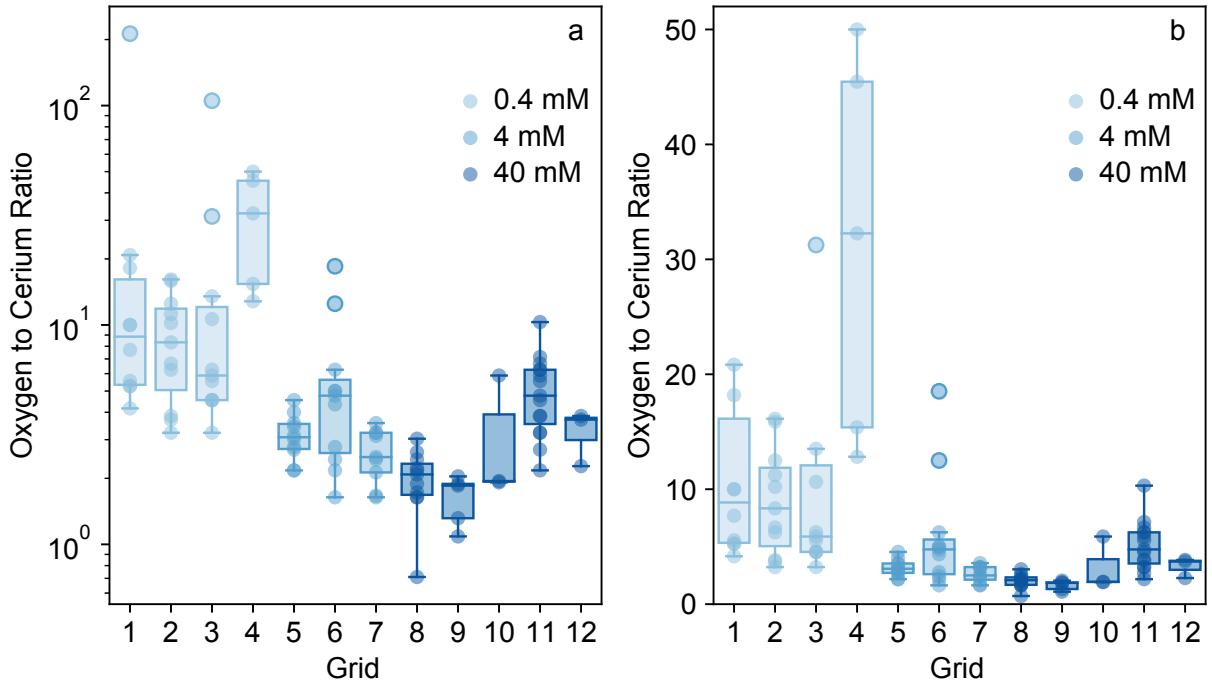

Figure A.3.5: Box plots of the oxygen to cerium ratio of individual graphene liquid cells prepared with with 0.4, 4, or 40 mM $CeCl_3$ plotted on a a) log and b) linear scale. Note that the top most outliers on grids 1 and 3 were removed from b) for clarity.

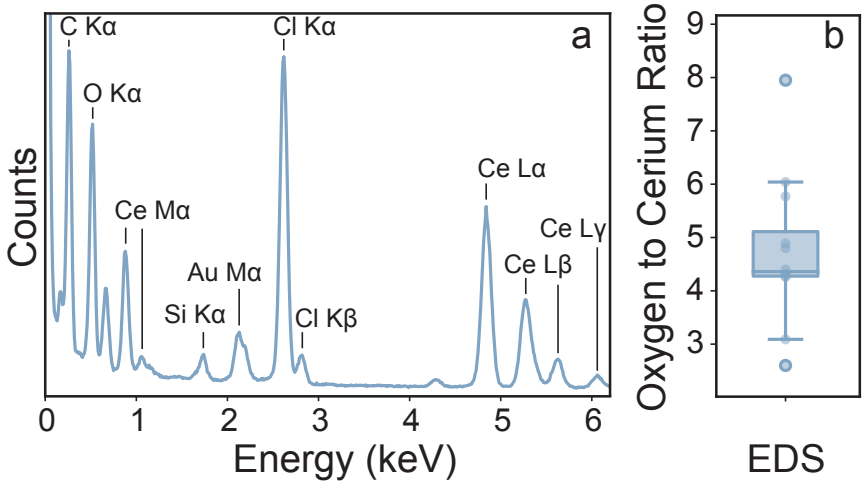

Figure A.3.6: a) Representative EDS spectra and b) box plot of the oxygen to cerium ratios calculated from the spectra. The ratio calculated from the EDS measurements is 4.73 ± 1.33

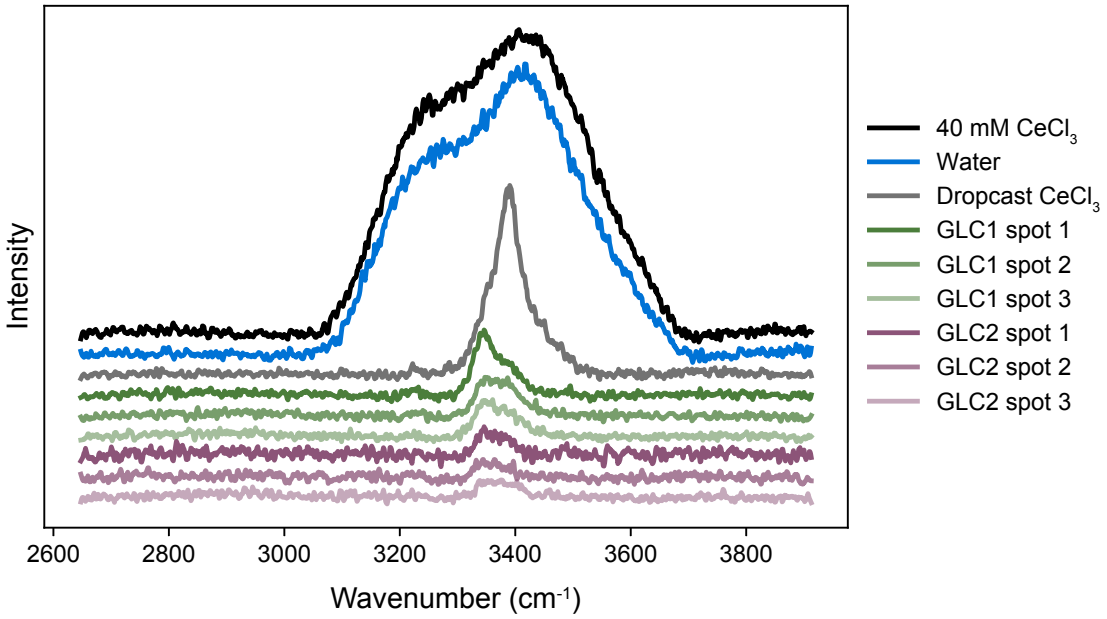

Figure A.3.7: Raman spectra two graphene liquid cells measured at three different regions, as well as standard spectra of water, 40 mM $CeCl_3$, and dropcast $CeCl_3$.

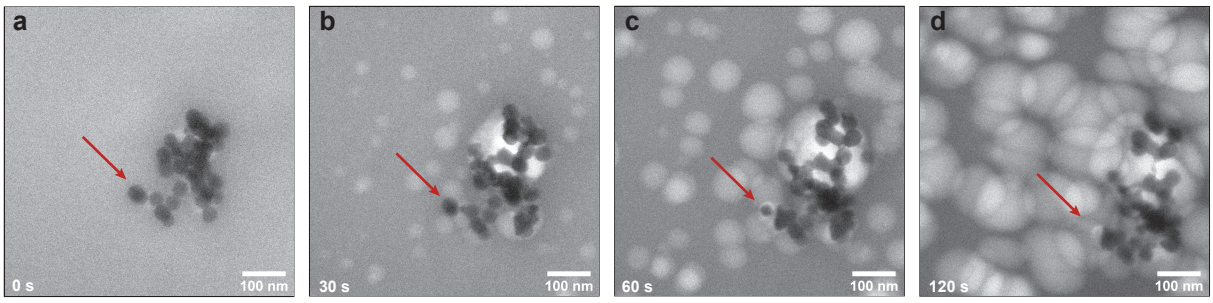

Figure A.3.8: a-d) Times series of AuNCs etching on a single grid. Note the nanocrystal etching highlighted by the red arrow

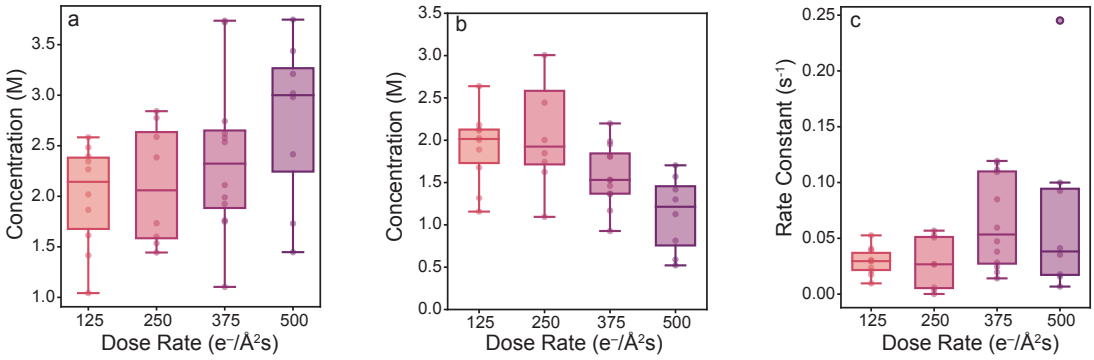

Figure A.3.9: Box plot of the a) A, b) B, and c) k_2 fitting terms for the biexponential function $[Ce^{4+}] = A(1\text{-}e^{(-k_1 t)}) + B(1\text{-}e^{(-k_2 t)})$. The box plot for the k_1 term is in Figure 4f

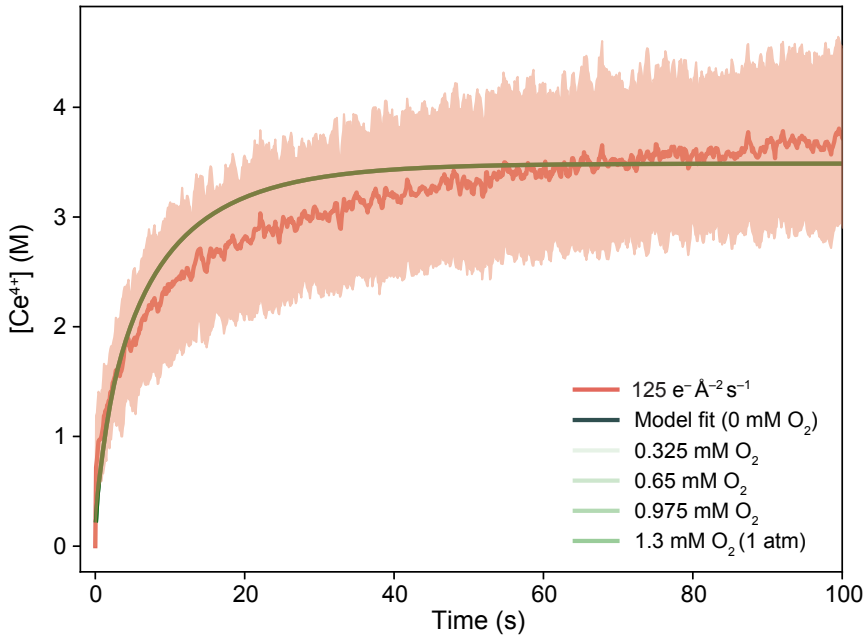

Figure A.3.10: Plot of the the model output of Ce^{4+} concentration over time with varying levels of initial dissolved O_2 at 125 $e^{-}Å^{-2}s^{-1}$. These outputs are overlaid on the original model output (0 mM initial dissolved O_2) and the experimental Ce^{4+} concentration over time. All of the models are overlaid on each other, indicating that the initial dissolved oxygen levels have very little effect on the Ce^{4+} concentrations.

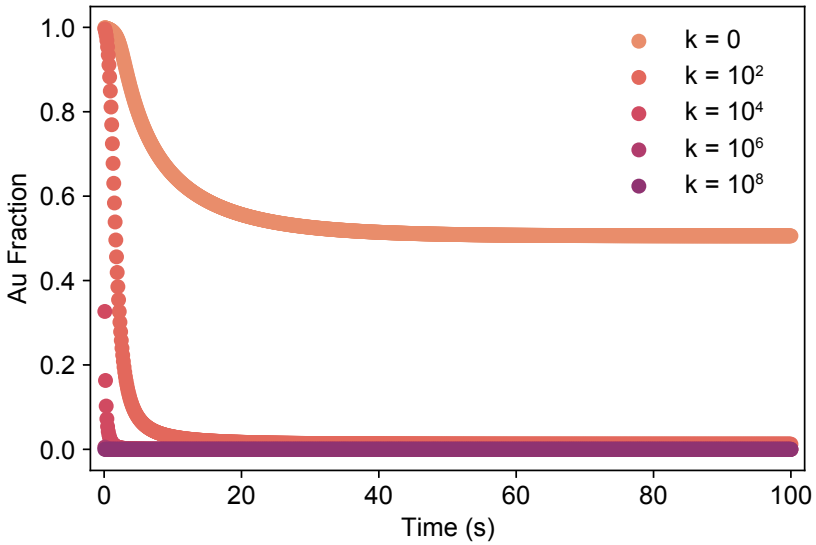

Figure A.3.11: Plot of the the model output of the fraction of Au(0) over time as the rate constant for the reaction $Au^0 + Ce^{4+} \longrightarrow Au^{1+} + Ce^{3+}$ is varied. From the data it is clear that without a reaction between Au^0 and Ce^{4+}, Au^0 does not fully oxidize, but once this reaction proceeds, the gold fully oxidizes. Note that this is a homogeneous model, meaning that the Au^0 in this model is soluble gold, so it is difficult to quantitatively correlate this to the etching trajectories.

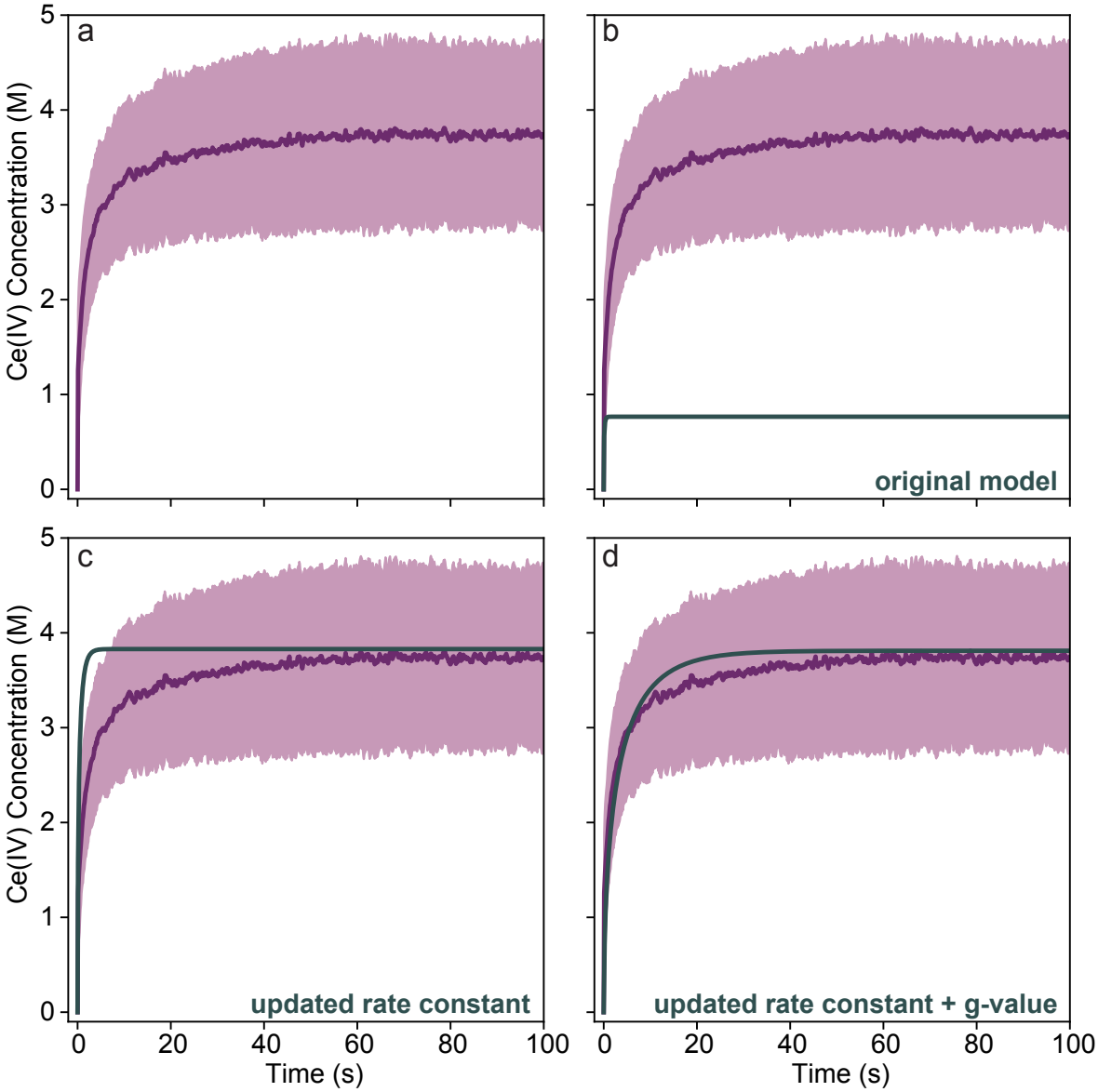

Figure A.3.12: Development of the kinetic radiolysis model output of Ce^{4+} formation. The outputs for the model only at 500 $e^{-}Å^{-2}s^{-1}$ is shown for clarity. a) Statistics of the kinetic EELS data collected at 500 $e^{-}Å^{-2}s^{-1}$ re-plotted here and in b), c), and d) for comparison purposes. b) Output of the original kinetic radiolysis model published in Moreno-Hernandez et al.[83] with an input concentration of 10.57 M Ce^{3+}. c) Kinetic radiolysis model output with updated rate constant for R96 as described below. d) Kinetic radiolysis model output with updated rate constant for R96 and updated g-value for H_2.

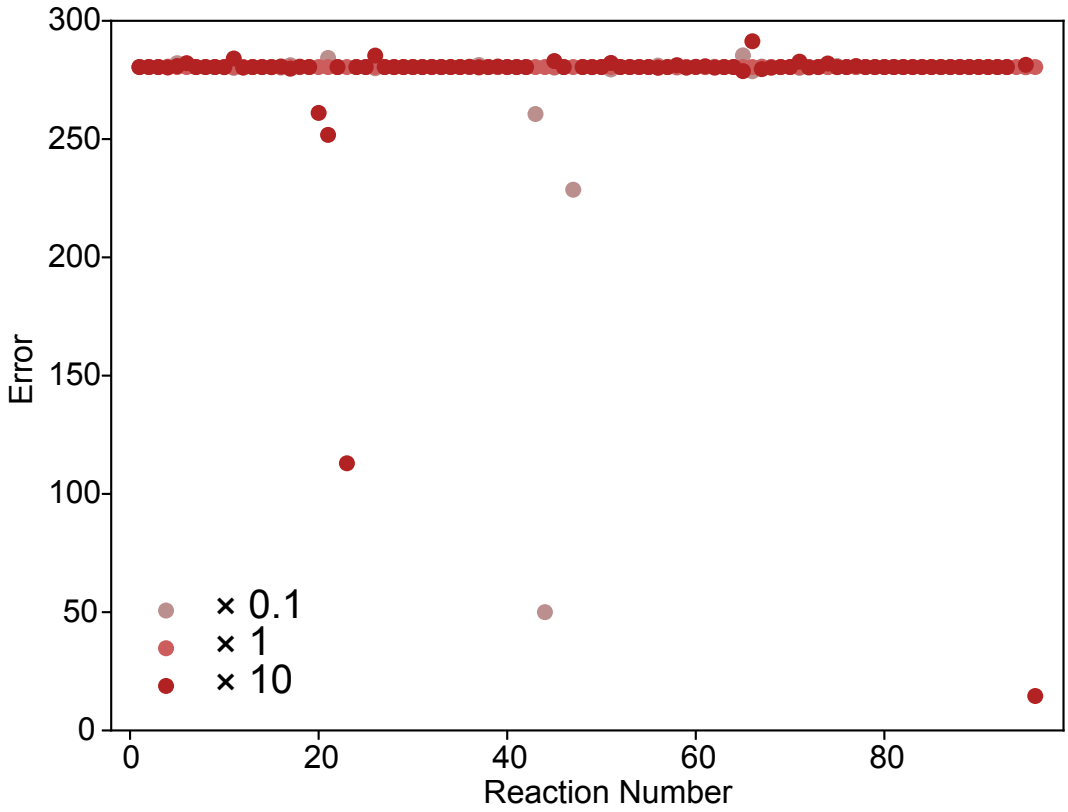

Figure A.3.13: Error obtained if reaction rates in original model are changed by a factor of 0.1, 1 (no change), or 10. While this analysis shows that reaction 44 could be changed ($HO^{\bullet}$ reacting with H_2), we did not choose to change this since there was no clear reason this rate would change since H_2 is a gas-phase product. An additional sensitivity analysis indicates that after updating R96 changes to R44 do not substantially improve the error (see A.3.14 below).

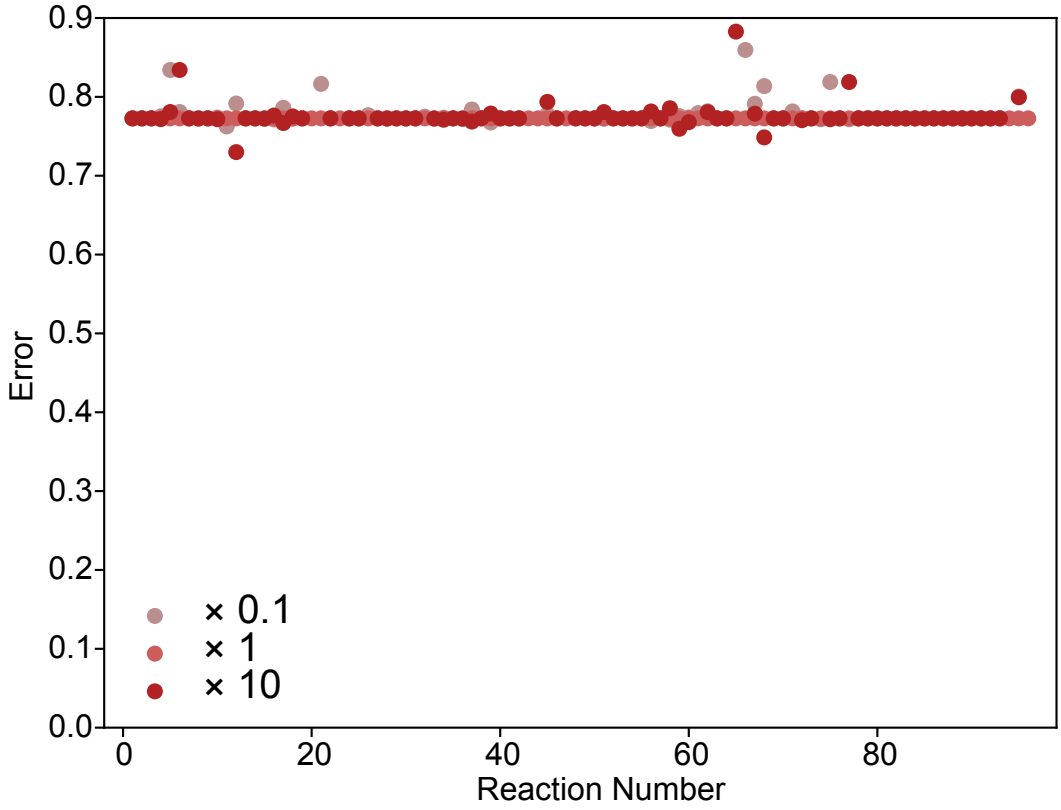

Figure A.3.14: Error obtained after setting R96 to 2.27×10^9 if reaction rates in original model are changed by a factor of 0.1, 1 (no change), or 10.

A.4 Chapter 3 Supplementary Tables

Table A.5: Summary of Cl and Ce Chemical Reactions Included in Radiolysis Chemical Network Model

No.	Reaction	Rate Constant ($M^{-1}s^{-1}$ or s^{-1})	Reference
74	$HO^{\bullet} + Cl^{-} \longrightarrow ClOH^{\bullet -}$	4.3×10^{9}	El Omar et al.[157]
75	$ClOH^{\bullet -} \longrightarrow OH^{\bullet} + Cl^{-}$	6.1×10^{9}	El Omar et al.[157]
76	$Cl^{\bullet} + Cl^{-} \longrightarrow Cl_2^{\bullet -}$	8.5×10^{9}	El Omar et al.[157]
77	$H^{+} + ClOH^{\bullet -} \longrightarrow Cl^{\bullet} + H_2O$	2.1×10^{10}	El Omar et al.[157]
78	$ClOH^{\bullet -} \longrightarrow Cl^{\bullet} + OH^{-}$	2.3×10^{1}	El Omar et al.[157]
79	$Cl^{\bullet} + OH^{-} \longrightarrow ClOH^{\bullet -}$	1.8×10^{10}	El Omar et al.[157]
80	$Cl_2^{\bullet -} \longrightarrow Cl^{\bullet} + Cl^{-}$	6.0×10^{4}	El Omar et al.[157]
81	$Cl_2^{\bullet -} + Cl_2^{\bullet -} \longrightarrow Cl_3^{-} + Cl^{-}$	2.0×10^{9}	El Omar et al.[157]
82	$Cl^{\bullet} + Cl_2^{\bullet -} \longrightarrow Cl_3^{-}$	6.3×10^{8}	El Omar et al.[157]
83	$Cl^{-} + Cl_2 \longrightarrow Cl_3^{-}$	1.0×10^{4}	El Omar et al.[157]
84	$Cl_3^{-} \longrightarrow Cl^{-} + Cl_2$	5.0×10^{4}	El Omar et al.[157]
85	$Cl^{\bullet} + Cl^{\bullet} \longrightarrow Cl_2$	8.8×10^{7}	El Omar et al.[157]
86	$e_{aq}^{-} + Cl^{\bullet} \longrightarrow Cl^{-}$	1.0×10^{10}	El Omar et al.[157]
87	$e_{aq}^{-} + Cl_2^{\bullet -} \longrightarrow 2Cl^{-}$	1.0×10^{10}	El Omar et al.[157]
88	$e_{aq}^{-} + Cl_3^{-} \longrightarrow Cl^{-} + Cl_2^{\bullet -}$	3.0×10^{10}	El Omar et al.[157]
89	$H^{\bullet} + Cl^{\bullet} \longrightarrow H^{+} + Cl^{-}$	1.0×10^{10}	El Omar et al.[157]
90	$H^{\bullet} + Cl_2^{\bullet -} \longrightarrow H^{+} + Cl^{-}$	8.0×10^{9}	El Omar et al.[157]
91	$H^{\bullet} + Cl_3^{-} \longrightarrow H^{+} + Cl^{-} + Cl_2^{\bullet -}$	1.0×10^{10}	El Omar et al.[157]
92	$HO_2^{\bullet} + Cl_2^{\bullet -} \longrightarrow 2Cl^{-} + O_2 + H^{+}$	1.0×10^{9}	El Omar et al.[157]
93	$HO_2^{\bullet} + Cl_2 \longrightarrow Cl_2^{\bullet -} + O_2 + H^{+}$	1.0×10^{9}	Bjergbakke et al.[163]
94	$Ce^{4+} + e_{aq}^{-} \longrightarrow Ce^{3+}$	6.6×10^{10}	Gogolev et al.[179]

95	$Ce^{4+} + H^{\bullet} \longrightarrow Ce^{3+} + H^{+}$	6.6×10^{7}	Gogolev et al.[179]
96	$Ce^{3+} + OH^{\bullet} \longrightarrow Ce^{4+} + OH^{-}$	2.27×10^{9}	This Work
97	$Au^{+} + H^{\bullet} \longrightarrow Au^{0} + H^{+}$	8.0×10^{9}	Ambrožič et al.[85]
98	$Au^{+} + e^{-}_{aq} \longrightarrow Au^{0}$	8.0×10^{9}	Ambrožič et al.[85]
99	$Au^{0} + OH^{\bullet} \longrightarrow Au^{+} + OH^{-}$	1.83×10^{9}	Ambrožič et al.[85]
100	$Au^{0} + Ce^{4+} \longrightarrow Au^{+} + Ce^{3+}$	4×10^{9}	See Text

Table A.6: Summary of G-Values Included in Radiolysis Chemical Network Model

Species	G-Value (molecules/ 100 eV)	Reference
e_{aq-}	0.382	This Work
$H^{\bullet}$	0.110	This Work
H_2	0.011 to 0.028	This Work
$HO^{\bullet}$	0.400	This Work
H_2O_2	0.052	This Work
H^{+}	0.486	This Work
HO^{-}	0.105	This Work
$HO_2^{\bullet}$	See Text	This Work
H_2O	See Text	This Work

Table A.7: Review of Encapsulated Salt Solutions in Graphene and Amorphous Carbon Liquid Cells

No.	Solute	Solvent	Ref.
1	0.5% Triton X-100, 0.25% glutaraldehyde	water	Park et al.[82]

2	0.15 M $FeCl_3$	water	Chen et al.[81]
3	'biological sample containing solution'	water	Wang et al.[22]
4	Fetal bovine serum	water	Ribeiro et al.[180]
5	34 mM NaCitrate & 0.24 mM $HAuCl_4$	water	Zhu et al.[181]
6	37-45 mM $FeCl_3$	water	Hauwiller et al.[76]
7	$FeCl_3$, Tris Buffer HCl, HCl	water	Ye et al.[79]
8	Tris Buffer HCl, general tubulin buffer	water	Keskin, and de Jonge[182]
9	38 mM $FeCl_3$, 8 mM HCl, 58 mM Tris Buffer HCl	water	Hauwiller et al.[78]
10	3wt% NaCl	water	Yang et al.[91]
11	TBE Buffer, 200 mM NaCl	water	Chen et al.[35]
12	0.15 M NaCl	water	Cho et al.[60]
13	40 mM $FeCl_3$, 190 mM HCl	water	Crook et al.[84]
14	10 mM $CeCl_3$/ 10 mM V_2O_4/ 10 mM $CrCl_3$	water	Moreno-Hernandez et al.[83]
15	29-42 mM $FeCl_3$, Tris Buffer HCl	water	Hauwiller et al.[77]
16	2 mM sodium phosphate buffer, 15 mM NaCl	water	Kang et al.[183]
17	5 mM 4-(2-hydroxyethyl)-1-piperazineethanesulfonic acid buffer	water	Kim et al.[103]
18	Saturated NaCl	water	Wang et al.[184]
19	5 mM $NaAuCl_4$	water	Dachraoui et al.[185]

Table A.8: Review of Encapsulated Organic Solutions in Graphene and Amorphous Carbon Liquid Cells

No.	Solute	Solvent	Ref.

1	1M $LiPF_6$ & Si NPs	1:1:1 EC : DMC : DEC	Yuk et al.[186]
2	10 mg/mL $Pt(AcAc)_2$	9:1 o-dichlorobenzene : oleylamine	Yuk et al.[18]
3	1.3 M $LiPF_6$	3:7 EC:DEC with 10 wt% fluoro-EC	Chang et al.[187]
4	$Mg(TFSI)_2$	diglyme	Kim et al.[188]
5	1.3 M $LiPF_6$	3:7 EC:DEC with 10 wt% fluoro-EC	Cheong et al.[189]
6	$Ni(acetate)_2$	20:1 o-dichlorobenzene : oleylamine	Yang et al.[190]
7	Pt NCs	20:1 o-dichlorobenzene : oleylamine	Park et al.[82]

Table A.9: Review of Encapsulated Pure Water in Graphene Liquid Cells

No.	Solvent	Note	Ref.
1	water	Cu NCs formed under e-beam exposure (Fig. 5), indicating leftover Cu salt from wet transfer process	Sasaki et al.[34]
2	water	Potential high-Z contaminants shown in Figure S2	Ghodsi et al.[28]
3	water	Cu/Ni NCs formed under e-beam exposure (Fig. 2, 3, 4), indicating leftover salt from wet transfer process	Hirokawa et al.[191]
4	water	Reply published[192] indicating likely NaCl contaminants	Algara-Siller et al.[193]
5	water	Potential high-Z contaminants shown in Figures S5, S6, S10	Ghodsi et al.[36]
6	water	Potential high-Z contaminants shown in Figure S3	Wang et al.[184]

Appendix B

Supplementary Multimedia

B.1 Chapter 2

Videos are hosted on the ACS website at `10.1021/jacs.1c05099`

Movie B.1.1: Movie of a gold nanocrystal in solution with 190 mM Cl^- and no iron. Note the distinct lack of etching. Available at `10.1021/jacs.1c05099,ja1c05099_si_002.avi`

Movie B.1.2: Movie of a gold nanocrystal in solution with 190 mM Cl^-, 0.38 mM Br^-, and no iron. Note the distinct lack of etching. Available at `10.1021/jacs.1c05099,ja1c05099_si_003.avi`

Movie B.1.3: Movie of a gold nanocrystal in solution with 190 mM Cl^-, 0.38 mM I^-, and no iron. Note the distinct lack of etching. Available at `10.1021/jacs.1c05099,ja1c05099_si_004.avi`

Movie B.1.4: Movie of a gold nanocrystal in solution with 190 mM Cl^- and 40 mM Fe^{3+}. Available at `10.1021/jacs.1c05099,ja1c05099_si_005.avi`

Movie B.1.5: Movie of a gold nanocrystal in solution with 190 mM Cl^-, 0.38 mM Br^-, and 40 mM Fe^{3+}. Available at `10.1021/jacs.1c05099,ja1c05099_si_006.avi`

Movie B.1.6: Movie of a gold nanocrystal in solution with 190 mM Cl^-, 0.38 mM I^-, and 40 mM Fe^{3+}. Available at `10.1021/jacs.1c05099,ja1c05099_si_007.avi`

Movie B.1.7: Movie of a gold nanocrystal etching in a solution with 190 mM Cl^- and 40 mM Fe^{3+}. The electron flux is initially increased to 800 $e^-Å^{-2}s^{-1}$ to induce etching. In the middle of the etching trajectory, the electron flux was decreased to 25 $e^-Å^{-2}s^{-1}$. Available at `10.1021/jacs.1c05099,ja1c05099_si_008.avi`

B.2 Chapter 3

Videos are hosted on the ACS website at `10.1021/jacs.2c07778`

Movie B.2.1: Movie of a gold nanocrystal etching in a solution with 40 mM $CeCl_3$ at an electron flux of 500 $e^-Å^{-2}s^{-1}$ Available at `10.1021/jacs.2c07778,ja2c07778_si_003.avi`

Movie B.2.2: Movie of a gold nanocrystal etching in a solution with 40 mM $CeCl_3$ at an electron flux of 375 $e^-Å^{-2}s^{-1}$ Available at `10.1021/jacs.2c07778,ja2c07778_si_004.avi`

Movie B.2.3: Movie of a gold nanocrystal etching in a solution with 40 mM $CeCl_3$ at an electron flux of 250 $e^-Å^{-2}s^{-1}$ Available at `10.1021/jacs.2c07778,ja2c07778_si_005.avi`

Movie B.2.4: Movie of a gold nanocrystal etching in a solution with 40 mM $CeCl_3$ at an electron flux of 125 $e^-Å^{-2}s^{-1}$ Available at `10.1021/jacs.2c07778,ja2c07778_si_006.avi`